BIOFUNCTIONAL HYDROGELS FOR SKELETAL MUSCLE CONSTRUCTS

A Dissertation
Presented to
The Academic Faculty

by

Apoorva S. Salimath

In Partial Fulfillment
of the Requirements for the Degree
Doctor of Philosophy in Bioengineering in the
Woodruff School of Mechanical Engineering

Georgia Institute of Technology
December 2015

BIOFUNCTIONAL HYDROGELS FOR SKELETAL MUSCLE CONSTRUCTS

Approved by:

Dr. Andrés J. García, Advisor
School of Mechanical Engineering
Georgia Institute of Technology

Dr. Thomas H. Barker
Department of Biomedical Engineering
Georgia Institute of Technology

Dr. Edward A. Botchwey
Department of Biomedical Engineering
Georgia Institute of Technology

Dr. Thomas J. Burkholder
School of Applied Physiology
Georgia Institute of Technology

Dr. Johnna S. Temenoff
Department of Biomedical Engineering
Georgia Institute of Technology

Date Approved: November 05, 2015

To my Parents, Dr. Uma Kalasuramath and Dr. Mukayya Swamy Kalasuramath

Thank you for your love and support

ACKNOWLEDGEMENTS

I am indebted to my adviser, Dr. Andrés García, for his careful supervision, consistent encouragement, and honest feedback. Andrés believed there was more to my project than I seemed to understand. He was always there when I needed him, but equally willing to let me figure things out on my own. Though invariably, the latter took much longer! I am thankful for his patience and guidance in bringing this document to a depth and breadth necessary to fulfill the requirements of a Georgia Tech dissertation.

I am grateful for my committee members: Dr. Thomas Burkholder, for his thorough and detailed advice on the study of skeletal muscle; Dr. Johnna Temenoff, for her succinct and clear opinions throughout the course of the project; Dr. Thomas Barker, for his encouragement and valued opinions beyond matrix biology; and Dr. Edward Botchwey for his thought-provoking views on science and methodologies. I have been given much actionable and useful feedback during our combined discussions at proposals, updates, and the defense. I am privileged to have had the opportunity to interact with each of you.

I am thankful for the environment of the Garcia Lab, where lab mates willingly exchange information, reagents and dog-sitting duties. Dr. Edward Phelps, who first introduced me to the weird and wonderful world of hydrogels, I will forever remember the way he taught me to not only perform protocols correctly, but also understand the reasoning behind each action. Dr. Ted Lee, who showed me speed and quality did not have to be mutually exclusive, and taught a detail-oriented rookie to be more efficient

and make time for a life outside of lab. I must thank Dr. Nduka Enemchukwu, for his diligent analysis of unpredictable hydrogel outcomes as his work and opinions have made their sure way into my protocols. Dr. Asha Shekaran was ever-open for scientific discussions and her upbeat attitude towards research motivated me. When she wasn't sharing useful advice on navigating Georgia Tech's unfathomable paperwork system, Dr. Stacie Gutowski baked, and I am grateful for the steady stream of delicious treats. Dr. Chi-Chi Esimai and I had several interesting conversations in the TC room, and her company made the lab a less lonely place at odd hours.

Kellie Burns-Templeman is missed as our resident Lab superhero, but I am glad we have Charu Kumar to take her place and answer all our questions about why our reagents haven't arrived yet.

As for the current lab group, it was a good day when I decided my seat in the lair would be next to Amy Clark (then Cheng). Our many scientific and non-scientific discourses have shaped not only my work at Georgia Tech, but my approach to life in general as well. I possibly owe her a good part of my grade in mathematical modelling, too. Devon Headen's commitment to his work, intelligent inputs, and exciting life outside of the lab continue to amaze and inspire me. Jose Garcia was ever-present to answer quick questions and humored me when I vented frustrations that were not entirely research related. Efrain Cermeno always made longer days in the lab better by blasting music, from Salsa to EDM. I am glad I shared my time in lab with his infectiously exuberant personality. Chris Johnson's strategic placement behind me in the lair meant he knew when I was on imgur.com, and made sure to call me out when my productivity was slipping. I am grateful to have shared my time at Garcia Lab with Dr. Rachit Agarwal,

Dr. Ankur Singh, Dr. Shalu Suri Singh, and Dr. Cristina Gonzalez. I am thankful to have learned from their experienced approach to science and life. The next generation of Garcia Lab: Ricardo, Dennis, and Allen will surely uphold a high standard and I look forward to hearing about their accomplishments in the upcoming years.

Dr. Julia Raykin, Yogi Patel and Brandon Williams have helped provide direction to parts of my thesis where I was less technically skilled, and I am grateful for their patient and persistent help. I am thankful for the members of the Michael Davis Lab at Emory University with whom I share my first scientific publication. Dr. Michael Davis, whose collaboration enabled the production of a very interesting interdisciplinary project, and Milton Brown, with whom I spent many hours performing surgery on rats.

I am glad to have shared the space in the lair with the enthusiastic and entertaining members of the Guldberg Lab: notably Alice Li, Lauren Priddy, Lakshmi Narayanan, Brennan Torstrick, Albert Cheng, Ashley Allen.

To the faculty and staff of IBB who have accommodated my needs and helped me avoid administrative catastrophes, notably, Mrs. Laura Paige, Ms. Karen Ethier and Mr. Allen Echols, thank you.

To Meghan Popcick and Charles Hammons at the Office of International Education who were invaluable in their support and advice as I navigated the complicated terrain of US law.

To my close friends in Atlanta, Madona Cumar and Rohit Ghosalker, thank you for being a source of comfort and joy. I cannot imagine these past five years without you.

Finally, gratitude is due to my family. My grandfather, Shri. Gangadharayya Hiremath, who was among the first to encourage me to pursue a Ph.D. To my grandparents and my parents, Dr. Uma and Dr. Swamy Kalasuramath, who have sacrificed more than I will understand and have believed in my ability long before I did. I owe them everything I have the privilege to achieve today. To my in-laws, Dr. Bharathi and Dr. Paramahans Salimath, whose scientific expertise is overshadowed by their love and affection for a daughter-in-law still adjusting to her role. Thank you all for your patience and unconditional love.

My husband, Sangam Salimath, who has put up with me through three years of marriage and five years of friendship and love. Thank you for always being there when I needed you. I am the luckiest woman in the world.

Thank you all.

TABLE OF CONTENTS

LIST OF TABLES

LIST OF FIGURES

Page

LIST OF SYMBOLS AND ABBREVIATIONS

ANOVA	Analysis of variance
ATP	Adenosine triphosphate
C2C12-MM	C2C12 mouse myoblasts
CK	Creatine kinase
CPC	Cardiac progenitor cells
DMEM	Dulbecco's modified eagle medium
DTT	Dithiothreitol
ECM	Extracellular matrix
EDTA	Ethylenediaminetetraacetic acid
ELISA	Enzyme-linked immunosorbent assay
FBS	Fetal bovine serum
HEPES	4-(2-hydroxyethyl)-1-piperazineethanesulfonic acid
HGF	Hepatocyte growth factor
IGF-1	Insulin-like growth factor 1
MHC	Myosin heavy chain
MMP	Matrix metalloproteinase
MRF	Myogenic regulatory factor
MYF	Myogenic factor
PBS	Phosphate buffered saline
PEG	Polyethylene glycol
PEG-4MAL	4-arm PEG-maleimide
RGD	Peptide sequence: GRGDSPC
ROI	Region of interest
SEM	Standard error of mean
SKM	Skeletal muscle
SMTE	Skeletal muscle tissue engineering
TEA	Triethanolamine
TE-MR	Tissue engineered muscle repair
VEGF	Vascular endothelial growth factor A
VML	Volumetric muscle loss

SUMMARY

Skeletal muscle tissue damage costs the US government hundreds of billions of dollars annually, and there are currently no suitable tissue replacements for skeletal muscle. In addition, there is great potential to use skeletal muscle as a scalable actuator system, covering wide length scales, frequencies, and force regimes. Hence, the interest in soft robotics and regenerative medicine methods to engineer skeletal muscle has increased in recent years. The challenges to generate a functional muscle strip are typical to those of tissue engineering, where common issues such as cell source, material scaffold, bioreactor method or configuration play key roles. Specifically, it is important to translate myogenesis knowledge into engineering constructs by examining the impact of the cell microenvironment on growth, alignment, fusion, and differentiation of skeletal muscle cells. The motivation behind this thesis was to generate a contractile 3D skeletal muscle construct utilizing biochemical and physical cues to guide muscle cell differentiation and maturation. Such a construct is expected to play an important role in medical applications and the development of soft robotics. To do this, 3D, swollen hydrogels were chosen to provide tailorable platforms that support cellular activities to similar extents as native matrices.

We utilized an engineered bio-functionalized poly(ethylene glycol)-(PEG)-hydrogel with maleimide (MAL) cross-linking reaction chemistry that gels rapidly with high reaction efficiency under cytocompatible reaction conditions. To develop an effective soft biomaterial for the development of an aligned, functional muscle construct, we (i)

screened hydrogel properties for differentiation, (ii) recreated alignment of skeletal muscle cells, (iii) determined effective generated force upon action of an external agonist. The impact of this study will be significant in the construction of biological machines while providing a unique regenerative solution for skeletal muscle tissue repair and regeneration.

CHAPTER I: SPECIFIC AIMS

The overall goal of this project is to create a functional skeletal muscle construct for the development of (i) skeletal muscle tissue engineering therapies when native tissue is lost due to trauma and age-related muscle loss, and (ii) soft actuators for biological machines.

First, the development of a contractile muscle unit for regenerative medicine applications would play a significant role in ameliorating conditions due to skeletal muscle damage, and further the field of tissue engineering. Volumetric muscle loss (VML), is an example of skeletal muscle damage that occurs as a result of trauma from accidents, sports or surgery; degenerative disease (cachexia); aging (sarcopenia); or inactivity (atrophy). Although skeletal muscle has an innate capacity to regenerate, this ability is compromised in conditions of severe trauma [8]. Available therapeutic options for VML are limited due to the complex process of skeletal muscle regeneration [8]. Second, utilizing skeletal muscle powered soft actuators in combination with a variety of cell types such as endothelial cells, fibroblasts, and neurons would enable the construction of biological machines. These machines will consist of sensing, information processing, actuation, protein expression and transport elements that can be effectively combined to create functional units [9, 10].

With increasing knowledge of the cellular and biochemical mechanisms associated with cell growth and maturation, there is greater interest in materials that provide biochemical cues to modify the *in vitro* microenvironment to facilitate development of

differentiated tissue, suggesting the viability of a skeletal muscle construct in a bio-functionalized scaffold [11].

Engineered bio-functionalized poly(ethylene glycol)-[PEG]-hydrogels with maleimide (MAL) cross-linking reaction chemistry gel rapidly with high cytocompatibility while still allowing "plug-and-play" design variation [12]. The non-fouling hydrogel network requires bioadhesive proteins to promote cell attachment, while its rate of degradation is controlled using protease-cleavable cross-linkers, creating a matrix capable of being tuned to support a variety of cell types. This project focuses on engineering a microenvironment, using these PEG-MAL hydrogels, to promote the development of differentiated contractile muscle tissue from skeletal muscle progenitor cells.

Preliminary data with these gel systems demonstrate that 3D gels of 5% (w/v) 4-arm PEG-maleimide (PEG-MAL) macromers functionalized with 2 mM RGDS adhesion peptide, and cross-linked by the addition of cysteine-flanked MMP-degradable peptide sequences (VPM) provide an optimized matrix for C2C12 mouse myoblast proliferation and differentiation. Based on this, ***we hypothesize that modulating matrix elasticity, adhesion, rate of degradation, and physical configuration of the hydrogel will enable us to create a critical microenvironment for the attachment, proliferation, differentiation and stable formation of multinucleated myotubes for functional skeletal muscle tissue constructs.*** To address this hypothesis, we investigated the following specific aims:

<u>Specific Aim 1:</u> To elucidate the effects of 3D PEG-MAL hydrogel properties on C2C12 skeletal muscle cell proliferation and differentiation. In this aim, we varied hydrogel parameters (polymer density, adhesive ligand type/concentration, rate of hydrogel degradation) and cell density for skeletal muscle progenitor C2C12 cell differentiation and contractile function within 3D poly(ethylene glycol)-[PEG]-hydrogels. We assessed viability of the cells with a range of hydrogel stiffness using periodic live/dead stains. Next, we observed the extent of differentiation by analyzing images of samples stained for sarcomeric myosin. *We hypothesized that hydrogel properties will influence the viability and differentiation of encapsulated cells*, allowing us to engineer the desired outcome: functional muscle tissue within a hydrogel scaffold. By varying the gel parameters mentioned, we were able to generate gel-muscle constructs containing myotubes and identify conditions that promoted myogenesis.

<u>Specific Aim 2:</u> To create an aligned muscle construct capable of contraction and measure the force generated due to the action of an external contractile agonist. In this aim, we established polymer microfabrication techniques using polydimethylsiloxane (PDMS) stamps for use with gels to align embedded cells in 3D, generating gel-muscle patches that can be separated from the original PDMS scaffold. *We hypothesized that physical cues in conjunction with the bioadhesive ligands and a mechanically supportive hydrogel microenvironment would aid in aligning differentiated myotubes and provide a cellular construct capable of agonist-induced contraction*. Alignment and maturation of cells was assessed by quantifying orientation of cellular actin using a combination of image analysis software and custom MATLAB code. It is

also important to be able to characterize contractile output with magnitude and frequency of force generated in order to create a functional and controllable contractile muscle strip or gel patch. We assessed force generated by the gel-muscle construct as it relates to change in length obtained by the excitation of muscle constructs using a custom-built device. During these studies, use of a contractile agonist and inhibitor further demonstrated effective contractile ability of the gel-muscle actuator. *We hypothesized that the muscle strip will be able to produce myosin-dependent contractile forces.*

The impact of this study in generating a controllable force actuator will be significant in the construction of biological machines. Concomitantly, this study will provide a unique regenerative solution for skeletal muscle tissue repair and regeneration.

CHAPTER II: INTRODUCTION

Skeletal Muscle

Skeletal Muscle Physiology

Skeletal muscles are one of the largest organs of the human body accounting for up to 40-50% of body weight. Their functions involve force production for locomotion, breathing, and postural support while contributing to heat production during cold stress [2]. This highly complex tissue contains an organized structure essential to its contractile function: each muscle is made up of bundles of long, cylindrical, multi-nucleated muscle fibers aligned in parallel. These muscle fibers consist of myofibrils that contain the sarcomere contractile units. Myofibrils, and consequently, muscle tissue, are uniaxially aligned to ensure efficient contraction as well as load transfer to the skeleton and ligaments (Fig.1A). Hence, skeletal muscle alignment is a classic example of the correlation of structure and function [2].

Cells within skeletal muscle tissue can be classified into two main groups: undifferentiated, normally quiescent, satellite cells and mature, adult myotubes which constitute 95% of myonuclei in healthy adult muscle tissue. [13]

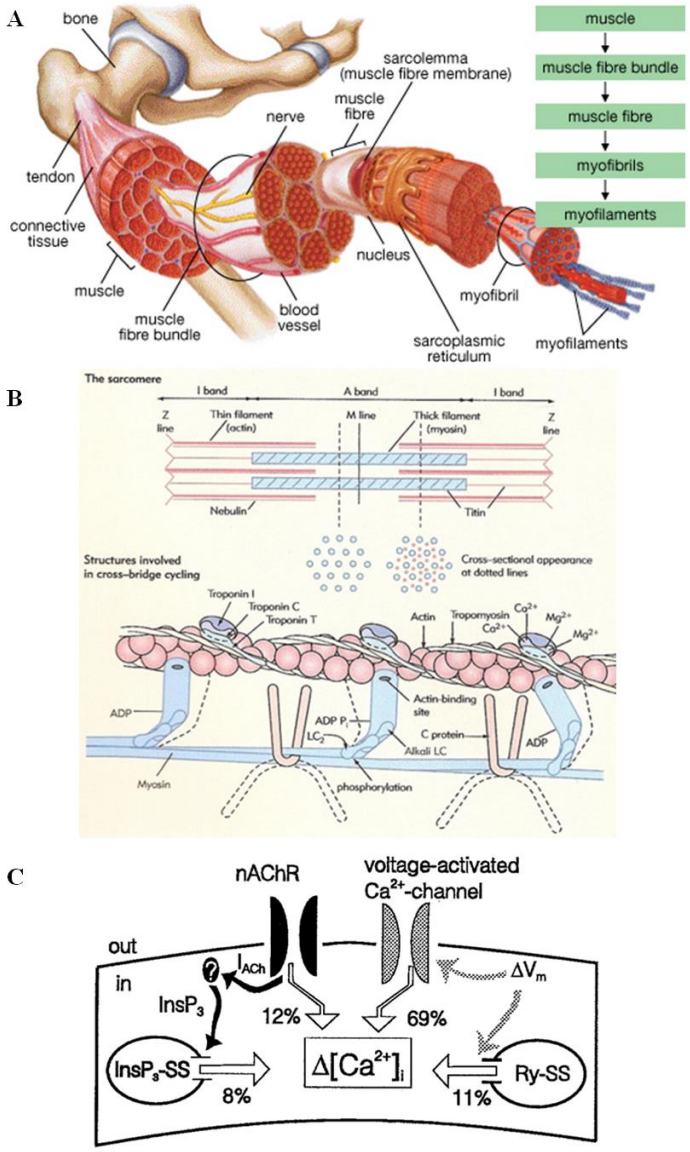

Figure 1: A. Muscle tissue consists of fascicles made of muscle fibers that contain myofibrils. The filaments within myofibrils are responsible for contraction as part of the sarcomere. Muscle fascicles are bound with connective tissue, in close proximity with neurons and blood vessels, and arranged with their long axes in parallel. B. Organization of a sarcomere and necessary proteins involved in cross-bridge cycling involving calcium ion (Ca^{2+}) . C. Schematic composition of acetylcholine (ACh)-evoked Ca^{2+} influx into the cytoplasm. The percentages represent the relative contribution of each Ca^{2+} source to the total peak change in intercellular Ca^{2+} as determined experimentally by Grassi et al. The activation of nicotinic ACh receptor (nAChR) causes current influx (I_{ACh}) and membrane depolarization (V_m). Intercellular calcium ion stores are the inositol triphosphate sensitive stores ($InsP_3$-SS) and the ryanodine senstivei sores (Ry-SS). I_{ACh} stimulates $InsP_3$ and ΔV_m triggers the opening of the voltage-gated Ca^{2+} channels and release of calcium from Ry-SS. [2-4]

Myofibers appear striated due to a highly organized arrangement of subcellular structures: sarcomeres (Fig.1B). A sarcomere consists of thick and thin filament arrays which form the basic contractile unit, and these arrays repeat in each myofibril. The sliding filament model is most commonly used to describe the muscle contraction at a molecular scale. [13-15] The model states that the molecular motors of muscle are the 'heads' of the myosin molecules (thick filament) which hydrolyze ATP and interact with other proteins, namely, actin (thin filament), in a process known as cross-bridge cycling, causing the filaments to slide past each other and muscle to shorten in length. [16, 17] The signal to contract is delivered via depolarized motor neurons to muscle fibers through the release of acetylcholine (ACh), a neurotransmitter, at the neuromuscular junction, causing the subsequent depolarization of muscle fibers. There are two types of ACh receptors: muscarinic and nicotinic, the latter being more involved in muscle physiological processes, localized at neuro-muscular junctions. In adult mammalian skeletal tissue, the rates of release and re-uptake of calcium ions from the sarcoplasmic reticulum play a vital role in defining the length and intensity of muscular contractions. Calcium ion influx into the bulk cytoplasm gives rise to an upstroke of the calcium transient [2, 3].

Using a specific model of differentiated C2C12 myotubes, it has been shown that nicotinic AChR (nAChR) activation prompts elementary cation currents for Ca^{2+} entry into the muscle fiber. ACh induced depolarization further elicits Ca^{2+} entry through the voltage activated channels, but more prominently, Ca^{2+} mobilization from the sarcoplasmic reticulum mediated by voltage and ryanodine-sensitive stores [4]. Calcium influx through voltage gated channels allows troponin C to bind to calcium ions,

allosterically modulating tropomyosin, which unblocks myosin binding sites for cross-bridge cycling to occur (Fig 1) [2, 3]. Magnesium ions are involved in closing calcium channels to restore resting state [2, 3].

Gene Regulation of Skeletal Muscle Development

The development of striated muscle is orchestrated by a complex series of mechanisms that reprogram gene expression and drive the reorganization of cellular structures [18-20]. This process occurs through the regulation of a network of intracellular signaling pathways that impact certain sequence-specific myogenic transcription factors (Table 1) [21-24].

Satellite cells are present in an undifferentiated, quiescent state around individual muscle fibers. The regulation of transcription factors *Pax3* and *Pax7* (paired box proteins 3 and 7) activate these cells to exit dormancy and expand, generating large numbers of myogenic progenitor cells. Quiescent satellite cells are held in undifferentiated state by the positive expression of *Pax7*, which is downregulated to limit proliferation and form myotubes. This process can be triggered during embryonic myogenesis or muscle regeneration after injury. [25]

In the intermediate stages of myogenesis, *MyoD* and/or *Myf5* genes are expressed in these proliferative myogenic cells which are then termed myoblasts [26-28]. Myoblasts express secondary myogenic regulatory factors (MRF's) and acquire a long, tubular structure to become myocytes [29, 30]. Finally, mononucleated myocytes fuse with each other to form multinucleated syncytium, which mature into contracting muscle fibers [29-31]. Throughout the process, a subpopulation of myoblasts, the satellite cells, remain

undifferentiated and associate with the surface of developing myofibers [26]. The embryonic origin of satellite cells remains to be determined; however, *Pax7* expression is essential for the specification and expansion of the satellite cell population. Cells failing to express *Pax3* or *Pax7* die or assume a non-myogenic fate. [26, 32]

Full differentiation entails skeletal muscle becoming a stable tissue characterized by multinucleated post-mitotic muscle fibers [33]. Mature myofibers, or individual myotubes, contain markers of functional differentiation that include sarcomeric myosin (which includes MHC, thick filament), troponin, desmin, titin, nebulin, and α-actin (thin filament) [34].

Table 1: Temporal chart of key genes and transcription factors (TF) regulating skeletal muscle development

Stage (Hours)	Genes and/or TF's Upregulated	Target(s)	Effect(s)
Early (0)	*Pax3*	Mesodermal somitic cells	Shift from quiescent into activated state, proliferation of which is termed myogenic precursor cell (mpc) expansion [26-28]
Early (0)	*Pax7*	Somitic cells and/or endothelial cells	Activation of satellite cells [26-28] Expansion of mpc population [26]
Mid	*MEF2D*	Skeletal muscle-specific genes MAPK pathway genes, EP300	Upregulation of creatine kinase and troponin production [35, 36] Regulates cell growth and division [37-39]
Mid (12+)	Primary MRF's: *Myf5* *MyoD*	Mesodermal somitic cells (during embryonic development) Myogenic precursor cell	Commitment to myogenic leniage, cells are termed myoblasts [26-28]
Late	Secondary MRF's: *Myogenin* *MRF 4*	Myoblasts	Terminal differentiation into myocytes [29, 30]
Full	*Myogenin* *MRF4*	Myocytes	Myocyte fusion, production of multinucleated myofibers [29-31]

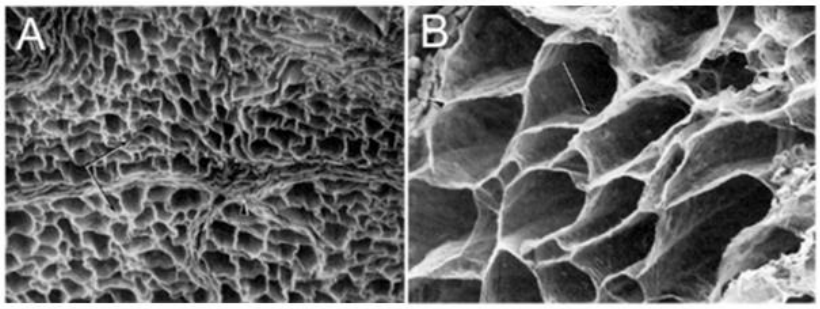

Figure 2: Scanning Electron Microscope Images at A, low, and B, high power magnification of the collagenous endomysial network around muscle fibers observed after NaOH digestion [7].

Skeletal Muscle Extracellular Matrix

The extracellular matrix (ECM) of skeletal muscle plays an important role in muscle fiber force transmission, maintenance, and repair [40]. There is increasing evidence to suggest that the ECM strongly regulates muscle's normal function, its load-bearing ability, its adaptability, and the reservoir of muscle stem cells it provides [40]. Pathological changes in muscle tissue are to some degree associated with ECM fibrosis, underlying its importance in a functional role [7]. Current knowledge suggests the division of the complex geometry of muscle ECM into three main categories: endomysial (around the muscle cell), perimysial (around groups of muscle cells) and epimysial (around the whole muscle) [7]. The most prominent features visualized in 3D through tissue sections indicate the presence of highly organized and extensive structure that cannot be appreciated in 2D. However, due to a lack of objective information about this ECM compared to that of other connective tissues, it is suggested that a higher order of muscle ECM organization exists that is yet to be defined. Figure 2 shows the endomysium as an array of tubes which surround the digested (not shown) muscle fibers. [7, 40, 41]

Key components of skeletal muscle ECM include (i) collagen, of which types I and III are most abundant, accounting for up to 10% of dry muscle mass; (ii) proteoglycans (PG) and glycosaminoglycans, mainly from the small leucine-rich proteoglycans (SLRPs) family; and (iii) matrix remodeling enzymes, namely MMP-2 and MMP-9. Comprising major structural components, there are notable collagen-proteoglycan interactions, including those of type I collagen with the major PG decorin and biglycan [40]. The most important specific interaction of skeletal muscle cells and its basement membrane is with laminin-211. Laminin-211 is a cell adhesion molecule and ligand for both the integrin isoform α7ß1 and dystroglycan. This interaction is believed to protect the muscle fiber from damage under the constant stress of contraction and influence signal transmission events [42].

Skeletal Muscle Contraction

The smallest functional skeletal muscle unit that can generate contractile force is the sarcomere. These are self-assembled in uniform alignment within a single myotube. Hence, functionality of muscle tissue can be examined, in order of increasing scale, by observing the response to stimuli of (i) sarcomeres, (ii) individual myotubes (multi-nucleated cells that share a cytoplasm), (iii) more mature muscle fibers, consisting of several myofibrils, and (iv)whole muscle tissue. Muscle contraction is characterized by the relationship between movement velocity and the amount of force exerted during muscular contraction. A single unit contraction in response to a stimulus is known as a 'twitch'. In humans, a single muscle twitch with an average of 40 ms contraction, 50 ms relaxation is produced (Figure 3A). Tests on single muscle fibers isolated from mouse

hind limb muscle (flexor brevis) show twitch forces of comparable time scale with 40 ms contraction periods in response to electrical field stimulation [43]. Increasing frequency of the stimulus results in a sustained, fused contraction response known as ‘tetanus’ as depicted in Figure 3B. Tetanic contractions correspond with maximal force produced by the contracting tissue [44].

Muscle tissue can act isometrically, without changing length to maintain a position, or isotonically, in a dynamic fashion (Figure 3C, D). In the force-length graph, considering the context of thick/thin filament overlap and ability of cross-bridge formation: the ascending limb represents the decreasing force output of the muscle as it is shortened beyond resting length. Peak muscle force is generated at the plateau: when length is equal

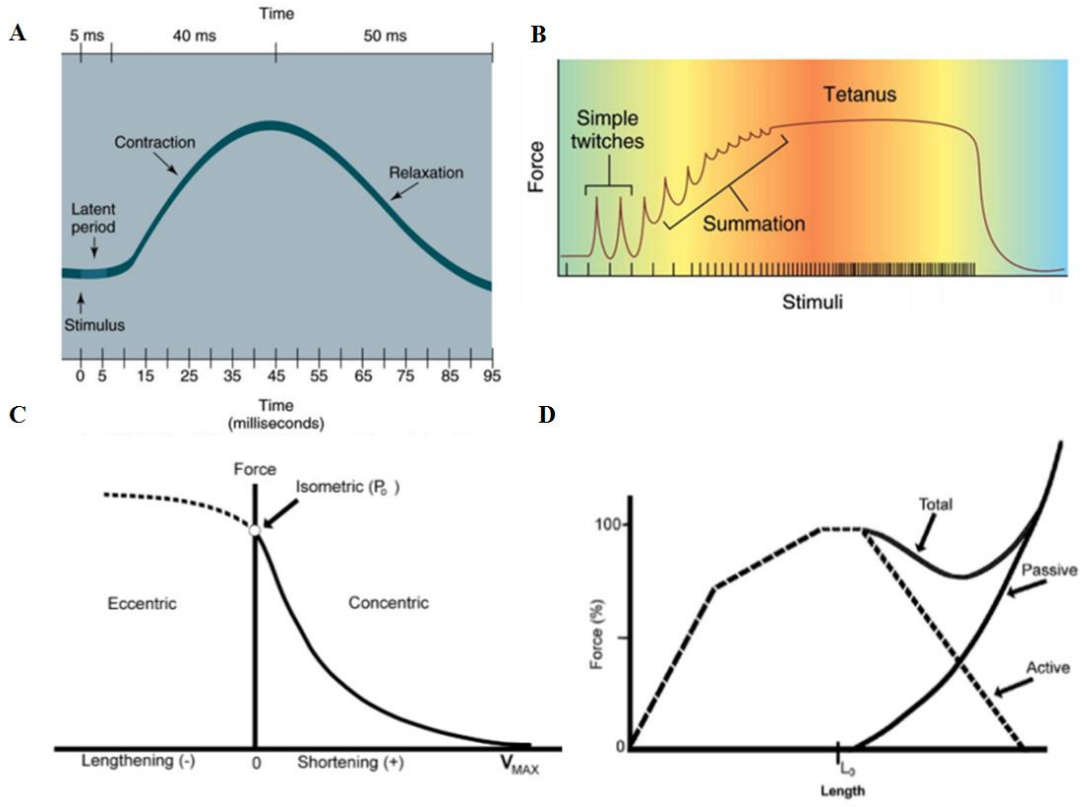

Figure 3: A. Force-time curve to show a single twitch, B. Force-time to show the approach towards tetanus force from repeated, high frequency stimulation. C. Force(F)-Velocity(V) graphs for power(P)=FxV, D. Force-Length(dL) curve for work done(W)=FxdL [2].

to resting length (L_0), where there is greatest cross-bridge overlap. The descending limb represents the decreasing active tension of a muscle when elongated beyond resting length [44].

In summary, the amount of force generated during muscular contraction is dependent on the following factors: (1) types and number of motor units recruited, (2) the nature of the motor units' neural stimulation and (3) the initial muscle length. The peak force generated by muscle decreases as the speed of movement increases. However, in general, the amount of power generated by a muscle group increases as a function of movement velocity [2].

Clinical Motivation for Skeletal Muscle Regeneration

In 2000, the World Health Organization estimated the total cost of musculoskeletal disease in the United States to be $254 billion and, in developing countries, the figure is estimated at $100 billion [45]. In 2004, the total estimated cost to the US Healthcare system (including lost wages) associated with musculoskeletal diseases was $949 billion [46].

Skeletal muscle tissue impairment can occur due to atrophy, neuromuscular disorders, or trauma [47, 48]. Muscle atrophy is the loss or wasting away of unused muscle tissue as a result of lack of activity, or poor neurological innervation [49]. Aging (sarcopenia) is responsible for some muscle atrophy cases, while others occur due to malnutrition, immobilization, injuries, and diseases such as osteoarthritis, rheumatoid arthritis, muscular dystrophy and myositis [49]. Neurogenic disorders result in a sustained

disassembly of tissue – due to disease or loss of nerves that control muscles – and include spinal cord injury (SCI), stroke, amyotrophic lateral sclerosis (ALS), Guillain-Barre syndrome, neuropathy and polio [50]. Finally, traumatic muscle injuries can result in both direct muscle tissue loss, and indirect muscle damage from poor innervation. Injuries commonly occur to the extremities during sports, resulting in contusions or strains, or from motor vehicle accidents, causing volumetric muscle loss (VML) [48]. Up to 88% of combat wounds in previous US armed conflicts involved traumatic soft tissue injuries, including VML, to the extremities [51]. VML is the traumatic or surgical loss of skeletal muscle resulting in severe functional impairment [52, 53]. Left untreated, or after deficient therapy, regional skeletal muscle atrophy can exacerbate muscle weakness throughout the limb that can persist for years [53].

VML treatment options vary with the severity and bodily location of muscle damage, though a universal consensus on how to manage such injuries and resulting functional deficits, has not been clearly defined [54]. Current treatments include (some combination of): (i) surgical options - functional free muscle transfer (autologous muscle flaps), debridement or muscle sarcoma excision [13, 48], (ii) growth factor delivery [54], (iii) amputation followed by the use of prosthetics [48], (iv) advanced bracing with stimulation (power-bracing) [55], and (v) physical therapy.

Surgical treatment options typically entail autologous muscle grafts (fasciocutaneous flaps) or muscle transposition that restore muscle mass and function [48, 56]. However, these approaches do not regenerate the lost muscle tissue, and are limited by associated donor site morbidity having caused alterations of the anatomy and biomechanics for both the recipient and the donor sites. Approximately 50% of patients suffer from pain and

37% report problems with physical activities 7-10 years after treatment [57, 58]. Patients that received radical debridement after a severe crush injury were more likely to suffer from motor disability [59]. In a study that compared limb function after excision of a muscle sarcoma, larger muscle excisions resulted in lower functional scores compared to partial muscle excisions [60], indicating the overall insufficiency of current surgical treatment options. Cell-based therapies are in their infancy and, to date, have largely focused on hereditary disorders such as Duchenne muscular dystrophy [48].

Soft tissue injuries begin with inflammation and edema compromising the vascular supply, resulting in hypoxia and tissue necrosis [61]. Skeletal muscle possesses a robust capacity to repair itself from minor traumas (tears, lacerations, and contusions). However, the endogenous repair mechanisms fail when 20% of total muscle volume is damaged, resulting in the accumulation of scar, denervation of distal skeletal muscle, and overall loss of function [54, 62]. The ability to enhance the inherent skeletal muscle repair process would significantly advance the treatment of congenital muscle disorders and severe muscle trauma for which, even with the best of present-day treatments, result in some form of physical handicap ranging from minor muscle asymmetries to permanent impaired function. Severe trauma patients often experience damage to ancillary systems, leaving amputation as a last resort limb-salvage technique.[48]. For endogenous repair therapies to advance, it is essential to build understanding of the biochemical, cellular and mechanical cues that promote skeletal muscle repair while minimizing scar formation to improve the potential for muscle regeneration [48]. Treatment options to promote the natural repair process include (i) the direct use of human recombinant growth factors

(IGF-1 [63], HGF [64], LIF [65]), (ii) gene therapy for growth factor delivery [66], (iii) inhibition of fibrosis through operative procedures [67], (iv) reduced fibrosis through antibiotic therapy by blocking overexpression of TGF-ß1, gamma-interferon [68, 69]. While these techniques were used in the clinical setting with good outcomes, the functional recovery of injured skeletal muscle remains limited [70-74], highlighting the need for further basic research into muscle regeneration.

VML can also be ameliorated by advanced bracing designs, electrical stimulation and physical therapy [52]. However, these techniques are unable to fully restore lost muscle and are often limited to VML below the knee.

The described unmet clinical need for skeletal muscle repair and limited treatment options has resulted in the exploration of regenerative medicine as an alternative or supplemental therapeutic option in the future [52].

Skeletal Muscle Tissue Engineering

Key considerations in skeletal muscle tissue engineering (SMTE) include the choice of an appropriate base matrix, a viable cell source, the incorporation of alignment cues for directed functionality, and vascularization to abet transport concerns with larger tissues.

Properties of the cell microenvironment such as matrix elasticity, amenability for degradation and presence of adhesive ligands play an important role in the cell physiology, or pathophysiology, affecting migration, proliferation, morphogenesis and

differentiation [75-80]. The process of myogenesis involves well-defined biochemical and physical cues to direct myoblast migration and proliferation as prerequisites to alignment and fusion of neighboring myotubes [26, 81]. Previous studies have demonstrated the importance of geometric cues [82] and the extracellular matrix (ECM) in controlling myogenic cell differentiation for skeletal muscle development [83], function [84], and structure [85]. Hence, the interest in engineering biomaterials to modify cellular microenvironment in vitro and facilitate the development of differentiated skeletal muscle tissue constructs [48].

Naturally-derived acellular scaffolds from mammalian tissues or components from non-mammalian sources (alginate, chitosan) provide structural properties in addition to signals and molecules that augment many aspects of cell behavior. Preclinical animal studies have shown that materials derived from small intestinal submucosa (SIS) and urinary bladder matrix (UBM) facilitate constructive remodeling of skeletal muscle tissue when implanted into a site of muscle injury [86]. Fibrin [87, 88], alginate [89], gelatin [90], keratin [91], and collagen [92, 93] have also been explored as matrices for muscle constructs. However, widespread application of naturally derived ECM scaffolds has been limited by variability in batch composition, potential immunogenicity, and challenges with modification, characterization and presentation of natural ECM materials.

Synthetic materials offer certain advantages over naturally derived materials in that they can be precisely characterized and fabricated with great control over physical and chemical properties. Synthetic scaffolds or materials used for SMTE include: polypropylene, polyesters such as poly(lactic acid) (PLA), poly(glycolic acid) (PGA),

poly(ε-caprolactone) (PCL) [94, 95], and their copolymers [96, 97], and various polyurethanes [98, 99]. These polymers have a limited efficacy with SMTE due to their non-physiological methods of manufacture for viable cell encapsulation during synthesis (as opposed to cell seeding after scaffold generation), and lack of biochemically relevant components.

Hybrid materials incorporating synthetic configurations in combination with naturally occurring components such as peptides show great promise for modulating bio-architecture as multi-component polymer matrices can be created by exploiting simple physiological reaction mechanisms [75]. Synthetic hydrogels that are closely related to biopolymer systems provide a platform to decouple material properties such as elasticity, degradation, and presence of adhesive ligands to examine ECM properties in a modular fashion [100]. The mechanical and chemical properties of synthetic polymers are typically easier to control; they can be non-toxic, readily available and consistently reproducible [101].

In vitro, muscle stem cells have been shown to contribute to muscle regeneration on soft 2D poly(ethylene-glycol) (PEG) hydrogel substrates [102], and within 3D PEG-based hydrogel constructs [103]. In vivo, PEG-fibrinogen hydrogel scaffolds for tissue engineering offer a potential therapeutic solution by providing biomaterial adjuvants that improve survival and engraftment of donor cells [104].

Producing highly organized, uniaxial microstructure during SMTE is essential for effective muscular contraction. This can be achieved by generating (i) cell-scaffold constructs of several uniformly aligned layers, (ii) scaffold constructs with uniform alignment, later seeded with cells, (iii) homogenous matrix and cell suspension to which

appropriate boundary conditions (mechanical tension, electrical stimulation, free surfaces) are applied when the construct is developing to direct remodeling and generate the desired structure, or (iv) enable 3-D alignment within a matrix seeded with homogenous cell suspension and allow cells to align within the construct during development [105]. Rapid vascularization of engineered muscle is critical as cells more than a few hundred microns from a blood supply are typically metabolically inactive or necrotic due to limited nutrient diffusion [106].

Applications of Skeletal Muscle to Biological Machines

Robotics is an important and rapidly growing feature of science and technology, dominated by robots constructed using hard materials such as metals (aluminum, steel) and ceramics (silicon, silicon oxide), with joints regulated by electrical, pneumatic, or hydraulic signals [107]. Hard robotics have several limitations: some are mechanical, causing instability on rough terrain or limited ranges of motion due to structural design. Others are due to control complexities: hard robotic plans are not able to handle fragile, anomalous-shaped objects (for example, internal organs during surgery).

Hence, soft robotics emerged as a field inspired by biology that attempts to build upon the abilities of traditional robotics, but with polymeric components that mimic biological actuators [107]. Elastomeric materials for force actuators can be reproducibly developed from tunable components that can modulate material properties for high strength and strain sustainability without fracture, enabling the production of soft robots that are flexible and strong.

While there is no current technology that can replicate the balanced performance of muscle [107], muscle-like contraction and dilation can occur in polymeric gels with changes in pH or salinity of a surrounding solution [108]. Electroactive polymers (EAPs) include dielectric elastomers, electrolytically active polymers [109], polyelectrolyte gels [110], and gel-metal composites [108]. Soft, acellular pneumatically-driven robots are still in the development phase but are able to walk [111, 112], swim [108], grip [113], bend and manipulate objects [114].

As the development of soft actuators potentially progresses fields from machine assembly to intricate surgery [107], opportunities for the use of biological machines arise. Biological soft robots incorporate cellular components to create force actuators as basic machine constituents. Biological machines explore an environmentally friendly technology that is renewable and biodegradable, while furthering the understanding of the science of emergent behaviors that will need to be employed to build such machines [5]. It is believed that biological machines will enhance our ability to accomplish tasks such as detecting and removing unwanted species from a food or drug, harvesting energy, monitoring the environment, or mimicking certain aspects of organ function [5].

Skeletal muscle serves as a primary actuator system in animals, performing tasks over a wide range of length and time scales, spatial configurations and force regimes [115]. The potential scalability of skeletal muscle makes it an ideal candidate for soft robotics and related applications. The unique performance metrics of skeletal muscle, namely, superior power-to-weight ratio, force-to-weight ratio, mechancial compliance and systems control compared to traditional mechanical actuators [116]. Specfically, muscle

fibers can be selectively activated and spatial and temporal signal summation allows the control and modulation of force generation in a dynamic fashion [117]. Lastly, an advantage of biological soft actuators as opposed to man-made actuators is the potential ability of self-repair.

The long-term goal of the Science and Technology Center (STC) on Emergent Behavior of Integrated Cellular Systems (EBICS) is to develop millimeter scale biological machines constructed with polymers and living cells that consist of sensing, information processing, actuation, protein expression and transport elements that can be effectively combined to create functional units (Fig.4) [5].

The development of such integrated cellular system has been a challenge due to technical issues that remain unaddressed. These include: controlled 2 and 3 dimensional patterning of living cells in bio-instructive materials; development of these biomaterials that allow cell growth and proliferation in 3D; alignment of cells to create muscle strips for desired actuation; development of in-vitro neuro-muscular junction and neuronal circuit to control the actuation of the muscle strips; coordination of the biological actuators for net movement; sensing of target neuro-toxins; release of the neutralization agents by cell-based factories embedded in the biomaterials, just to name a few [5].

With regards to force generation for locomotion, different processing units will require distinct actuators in specific micro-environments [5]. In a liquid or viscoelastic environment for instance, a ‘swimming’ motion may be most viable. Meanwhile, for movement along a surface, or prescribed path, a ‘walker’ or ‘crawler’ would need to be designed.

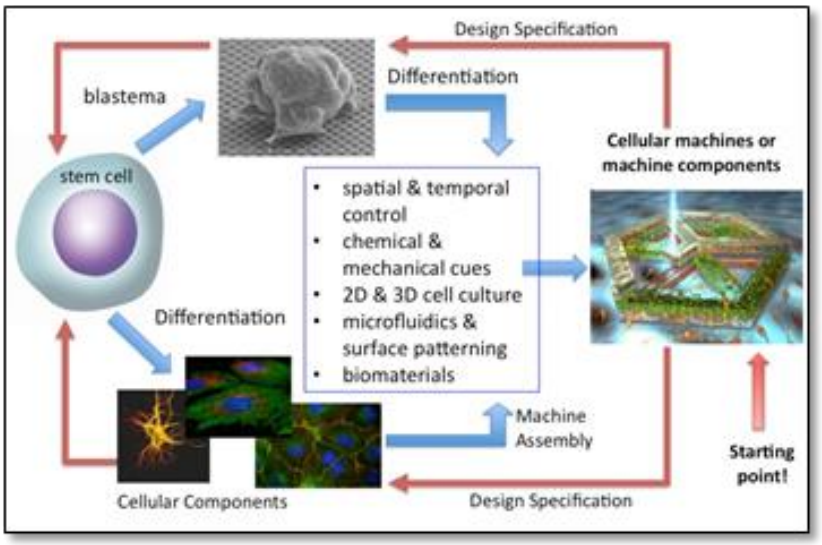

Figure 4: Pathways to a Biological Machine: A classical engineering approach involves defining the specifications for the cellular machine, desired functionalities and developing the necessary parts followed by assembly to construct machines. Meanwhile, a systems biology approach requires first understanding the emergent behaviors of cells and cell clusters to harness those properties to evolve interacting cell clusters that function within a biological machine with specific capabilities [5]

The microenvironment of cellular clusters is a critically important determinant of end cell fate. Hence, the creation of biologically relevant components for a cellular machine will require understanding of critical environmental features, modes of interaction for particular cell types, dominating growth and biochemical factors, and signaling mechanisms. It is expected that force actuators for the purposes of contractile function for locomotion will consist of myocytes (cardiac or skeletal). Myocytes will be studied to understand how they differentiate into myotubes to provide coordinated contractile function. A cellular-level understanding will then aid in the development of uniaxial muscle gel strips capable of efficient contraction mediated by external agonists. [5]

Recent attempts to engineer a robot capable of motion involved soft-lithography techniques to create acellular devices using poly(ethyleneglycol)-diacrylate (PEGDA) and polydimethylsiloxane (PDMS). In these cases, motion is generated by engineering

and exploiting unique properties of the polymer-based scaffolds [111, 118]. However, these constructs lack the biological component which is the core concept of cellular machines. Independent actuators utilizing living cells have till date, relied upon a non-degradable 2D substrate or utilized natural, plant or animal-derived scaffolds [10, 119]. These technologies will be further explored in the next section.

Relevant Work in Developing Muscle Constructs

Skeletal Muscle Constructs

Cells used in the generation of skeletal muscle constructs include human primary skeletal myoblasts [120], primary adult rat myogenic precursors [121], primary adult rat skeletal muscle derived cells [122], primary neonatal rat skeletal muscle derived cells [123-127], and the C2C12 mouse myoblast cell line [120, 128, 129]. The usage of primary cell lines is limited by characterization difficulties, short lifespans, slow proliferation rates, and finally, the tendency to suffer from high variability, complicating comparisons across laboratories. On the other hand, the C2C12 skeletal muscle progenitor cell line was established for the exploration of stem cell use for regenerative purposes upon grafting or transplantation [130]. Previous work has shown that specific ECM molecules such as laminin [131], collagen [132], fibronectin [133], and the adhesive peptide sequence ‘G-RGD-SPC’ [134] are able to modulate proliferation and differentiation of C2C12 cells, into mature mouse myoblasts, making this a suitable cell line to use in conjunction with biofunctionalized materials for SMTE.

Past research utilizing C2C12 cells to generate muscle strips involved the use of micropatterned substrates to induce cell alignment [135] and multi-layering of cells on PDMS [136]. The use of non-degradable substrates limited these designs to cell monolayers, that is, two dimensions. Consequent attempts utilized scaffold-less structures [137], or centered on seeding myogenic cells in three-dimensional (3D) scaffolds [89, 138], on surfaces of micro-threads [87], differentiating high-density myogenic cell pellets [139], and cell sheet tissue engineering with thermoresponsive polymer substrates for 3D oriented sheets of myotubes [140-143]. These methods have yielded 'thicker than 2D', and 3D constructs. Yet, while these studies show the production of skeletal muscle marker proteins and morphological suggestions of myogenesis they do not directly examine the influence of the scaffold and/or biological functionalization on myogenic differentiation in a modular manner.

Specifically, work involving seeding myogenic cells in 3D scaffolds of macroporous [89] or mesh form [138], do not produce densely populated constructs thicker than 1 mm. Furthermore, the extent of presented differentiation is intermediate, at the pre-myofibril stage [89, 138]. Meanwhile, Page et al.'s works involving microthreads [87] show incorporation of muscle cells into more differentiated muscle fibers, but this development is shown to occur in an in vivo microenvironment. In addition, the contractile function of the isolated microthreads themselves, in vitro, is not explicated [87]. Marquette et al. demonstrated the in vitro development of syncytia, unique to skeletal muscle, using C2C12 cells in a rotary cell culture system (RCCS) [139]. This work is unique in that it shows the development of 3D skeletal muscle from C2C12 without the presence of a scaffold, cell guidance, or growth factors. However, the syncytia detected is not aligned,

due to the lack of cell guidance cues and thus contractile function cannot be determined [139]. Cell sheet tissue engineering through thermoresponsive polymer substrates have enabled the development of anisotropic skeletal and cardiac muscle sheets [140-142] by the Okano lab in Japan. This method is able to generate aligned sheets of tissue-like cell layers, but the functionality of the skeletal muscle tissue stacks has not been described.

Notable examples of 3D skeletal muscle constructs (summarized in Table 2) that are amenable to force production and measurement include aligned 'myooids' [121, 122], muscle bundles with Velcro anchors [123], mesoscopic-scale porous cell networks [124, 125], and magnetic force-based tissue engineered constructs [128, 129]. Independent constructs, such as the free-floating collagen-muscle film strips by Fujita et al. [120, 144], optogenetically controlled collagen-matrigel constructs by Sakar et al. [145], and the 'miniature bio-artificial muscles' (mBAMs) of collagen-fibrin scaffolds by Vandenburgh et al. [146], show promise for the development of similarly functional biosynthetic hydrogel-based devices.

The contractile function of the described 3D systems is summarized in Table 2. The matrix supports for the functional 3D constructs, when used, are naturally derived. The disadvantages of naturally-derived scaffolds considering clinical translation and engineerability have been previously discussed. At the time of this review, no purely synthetic soft tissue scaffolds exist for the benefits of functional skeletal muscle tissue engineering. The cell types utilized in these constructs range from C2C12 cell lines [120, 144] to primary neonatal [124-127] and adult [122] rat skeletal muscle derived cells. Constructs also utilized muscle cells in combination with other cell types, such as mouse embryonic fibroblasts (MEFs) [146], or cells infected with GCaMP3 lentivirus [123]. The

force produced by these constructs covers a wide range from 0.88 μN (49.7 Pa for a tissue width of 150 μm) [144] to 26 mN (8.28 kPa for a tissue width of 1mm) [123]. This encompasses the active tension generated by a single myotube to the force produced by muscle bundles at the end of a 4-week incubation period.

There do not appear to be specific trends linking cell type with measured force as the output is a function of several factors, including, but not limited to: construct configuration, time of incubation, and method of stimulation. To put these force values in context, the adult mouse extensor digitorum longus (EDL) produces a peak isometric force of about 500 mN in vitro (240 kPa on 2.1 mm^2 cross sectional area, while the adult mouse soleus muscle can generate a peak isometric force of 200 mN (220 kPa on 1 mm^2) [147]. In vitro, the twitch force of an isolated adult mouse EDL muscle fiber of 25 μm diameter is 200 μN (400 kPa) [148]. This force is on the same scale as constructs discussed here, but taking a representative diameter of 1 mm in comparison, the force generated by native tissue is 40-fold higher. This suggests significant tissue engineering and regenerative medicine (TERM) progress is required before in vitro generated 3D muscle constructs are able to recapitulate by natural tissue.

The skeletal muscle tissue engineering (SMTE) constructs discussed have succeeded with the use of biological, not synthetic, scaffolds and are not easily and independently handled without tether to a surface. Hence, the field of SMTE could be further progressed through the exploration of synthetic scaffolds for the generation of free-formed constructs that are amenable to external control.

Table 2: Summary of 3D skeletal muscle-based constructs, in order of increasing 'cell layers', as reported (1o = Primary, Ad = adult, NN = neonatal, Imm = Immortal, myob = myoblasts, SKM = skeletal muscle, L = Length, W = Width, D = diameter, H = height/thickness, SA: surface area, NR = not reported)

Construct	*Cell layers*	Cell Type	Adhesion prevention	Matrix Support	Excitation Method	Force Measured	Overall Dimensions
Myooids [121]	*Cylindrical monolayer*	1^{o} Ad. rat myogenic precursors	PDMS with degradable laminin	No scaffold, laminin on silk end sutures pinned to PDMS	Electrical stimulation, Spontaneous 1Hz contraction	3-30µN; 215 µN peak twitch; 440 µN max tetanus.	L: 12mm D: 0.1-1mm
Microfeature guided Myooids [122]	*Cylindrical monolayer*	1^{o} Ad. rat SKM	PDMS with degradable laminin	Fibrin, laminin, buckled PDMS pattern for alignment	Electrical stimulation	100-200 µN peak twitch ; 200-400 µN aligned tetanus	L: NR D: 254µm
Bio-artificial muscles: mBAMs [146]	*Several, 3D*	Imm C57 + *mdx* myob	None mentioned	1% Collagen-I + 0.5mg/mL fibrin, hydrophobic PDMS µposts	Electrical stimulation	45µN max tetanic force	L: 5mm D:1-1.5mm
Magnetic force-based TE [128, 129]	*2D cell sheets self-contract to form 3D constructs*	C2C12	Ultra-low attachment TCP	Collagen-I + Gelatin	Electrical stimulation	33.2µN twitch force	L: NR D: 150µm
Mesoscopic scale cell network with hexagonal pores [124-127]	*100-400 µm; 127-384µm thick*	1^{o} NN rat	0.2% (w/v) Pluronic F-127	Fibrin + Matrigel, Velcro frame as anchors	Spontaneous contraction, macroscopic scale	1-3mN [126]	L: 1.4mm W: 1.4mm SA: 0.5-2cm^{2}
Opto-genetically controlled µtissue [145]	*3-7 myotubes*	C2C12	0.1% (w/v) Pluronic F-127	Collagen-I + Matrigel	Optical stimulation	Tension: Active: 1.41 ±0.25 mN, Static: 10.8±0.18 mN	L: 300µm W: 100-200µm D: 19µm
TE-SKM [149]	*NR, Compacted fibre*	1^{o} rat myob	Hydrophilic PDMS mold	Collagen-I + Matrigel, 2 anchorage points	Electrical stimulation to mimic EMG	Force N/A, δ = 5 µm as observed by 30 fps CCD camera	L: 2.3mm W: 1-0.1mm
Muscle Bundles [123]	*NR*	1^{o} NN SKM + GCaMP3 lentivirus	0.2% (w/v) Pluronic F-127	Fibrin + Matrigel, PDMS molds, Velcro anchors	Electrical stimulation	Twitch // tetanus 1wk: 8 / 17mN 2 wk: 17 / 28mN 4 wk: 22 / 26mN	L: 1.5cm D:1.5-3mm

Methods to Determine Muscle Construct Functionality

The experimental set-up designed to measure force of a multinucleated muscular construct is dependent upon the construct size and design. Direct measurements of force typically involve the twitch or tetanic response and isometric force generation detected using a force transducer [120, 122, 123, 127, 143, 150, 151], or a high speed camera to relate the motion of muscle constructs to the force generated [152, 153], using known mechanical properties of materials used. For instance, to measure the forces produced by miniature Bioartificial Muscles (mBAMs), Vandenburgh's group captured images monitoring the deflection of posts to which the mBAMs were anchored, at 4 frames per second (fps), to calculate the force that would have caused the observed displacement [146]. Similarly, the contractile function of microfabricated tissue gauges (μTUGs) was determined by examining the deflection of cantilever tips on which the constructs were formed [154].

Indirect measurements include the use of lentiviral transduction with an intracellular sensor for calcium ion flux that is attributed as proportional to functional muscle activity [123], and tracking the movement of secondary objects of estimated mechanical properties due to the supposed action of the primary muscular construct.

Activating agents for the controlled contraction of myoblasts range from custom-made solutions with high calcium ion or ATP content [155] and Tyrode's solution [43]; to small molecules such as dithiothreitol (DTT) [156, 157] and caffeine [43]; to the use of parallel platinum wire electrodes for electrical stimulation [121]. De-activating pharmacological treatments utilize agents such as blebbistatin [158], *N*-benzyl-*p*-toluene

sulphonamide (BTS), 2,3-Butanedione monoxime (BDM) [159], and tubocurarine chloride - an antagonist for the acetylcholine receptor [160].

Motivation for Research

Skeletal muscle tissue damage costs the US government hundreds of billions of dollars annually. Meanwhile, there is great potential to use skeletal muscle as a scalable actuator system, covering wide length scales, frequencies, and force regimes. Hence, the interest in soft robotics and regenerative medicine methods to engineer skeletal muscle has increased in recent years. The challenges to generate a functional muscle strip are typical to those of tissue engineering, where the triad of common TERM issues: cell source, material scaffold, bioreactor method or configuration play key roles. Specifically, it is important to translate the existing body of myogenesis knowledge into engineering muscle constructs by examining the impact of the cell microenvironment on growth, alignment, fusion, and differentiation of skeletal muscle cells. Thus, the main motivation behind this thesis is to generate a contractile 3D skeletal muscle construct utilizing organized biochemical and physical cues to guide muscle cell differentiation and maturation. Such a construct is expected to play an important role in medical applications and the development of soft robotics.

3D, swollen hydrogels provide tailorable platforms that support cellular activities to similar extents as native matrices. For this work, we utilized an engineered bio-functionalized poly(ethylene glycol)-(PEG)-hydrogel with maleimide (MAL) cross-linking reaction chemistry that gels rapidly with high reaction efficiency under

cytocompatible reaction conditions [12]. PEG alone has been shown to have low protein adsorption, a minimal inflammatory profile, well established chemistry, and a long history of safety in vivo. The PEG-MAL system in particular allows "plug-and-play" design variation, control over polymerization time, and small degradation products that are excreted via urine [161, 162]

CHAPTER III: BIOFUNCTIONAL HYDROGELS FOR SKELETAL MUSCLE CONSTRUCTS *

Abstract

Hydrogel scaffolds encapsulating C2C12 mouse skeletal muscle cells have been engineered as in vitro constructs towards regenerative medicine therapies for the enhancement and inducement of functional skeletal muscle formation. Previous work has largely involved two-dimensional (2D) muscle strips, naturally occurring hydrogels and incomplete examination of the effects of the scaffold and/or biological functionalization on myogenic differentiation in a controllable manner. The goal of this study was to identify key properties in functionalized poly(ethylene glycol) (PEG)-maleimide (MAL) synthetic hydrogels that promote cell attachment, proliferation and differentiation for the formation of multinucleated myotubes and functional skeletal muscle tissue constructs. Significant differences in myoblast viability were observed as a function of cell seeding density, polymer weight percentage and bioadhesive ligands. The identified optimized conditions for cell survival, required for myotube development, were carried over for differentiation assays. PEG hydrogels (5% weight/volume), functionalized with 2.0 mm RGD adhesive peptide and crosslinked with protease-cleavable peptides, incubated for 3 days before supplementation with 2% horse serum, significantly increased expression of differentiated skeletal muscle markers by 50%; 17% more multinucleated cells and a

---

* Adapted from: Salimath AS, Garcia AJ. *Biofunctional hydrogels for skeletal muscle constructs*. Journal of Tissue Engineering and Regenerative Medicine, 2014 Feb 26. doi: 10.1002/term.1881. [6]

40% increase in the number of nuclei/differentiated cell compared to other conditions. Functionality of cell-laden hydrogels was demonstrated by a 20% decrease in the extruded length of the hydrogel when stimulated with a contractile agent, compared to 7% for a saline control. This study provided strategies to engineer a three-dimensional (3D) microenvironment, using synthetic hydrogels to promote the development of differentiated muscle tissue from skeletal muscle progenitor cells to form contractile units.

Introduction

The development of a contractile muscle unit is significant to: (a) ameliorating impairment of morphological and physiological function conditions, such as volumetric muscle loss (VML) due to trauma; (b) aiding reconstructive and cosmetic faciomaxillary surgeries; and (c) engineering functional substitutions for lacking or deteriorated skeletal muscle in degenerative disease (cachexia), ageing (sarcopenia) or inactivity (atrophy) [52, 53]. Current therapeutic options are limited to skeletal muscle grafts, as *in vitro*-engineered tissues are incapable of recapitulating natural muscle bundle architecture and function, hence necessitating research into innovative tissue-regeneration approaches [126]. Additionally, contractile muscle constructs provide actuators for emerging cell-based machines [9].

Skeletal muscle tissue consists of striated multinucleated myotubes, collectively called myofibrils, which form the contractile structures of a muscle fibre and are uniaxially aligned to ensure efficient contraction and load transfer to the skeleton and ligaments

[163]. The process of myogenesis involves well-defined biochemical and physical cues to direct myoblast migration and proliferation, as prerequisites to the alignment and fusion of neighboring myotubes [26, 164]. Previous studies have demonstrated the importance of geometric cues [82] and the extracellular matrix (ECM) in controlling myogenic cell differentiation for skeletal muscle development [83], function [84], and structure [165]. With increasing knowledge of the cellular and biochemical mechanisms associated with skeletal myoblast growth and maturation, there is greater interest in improving our understanding of suitable materials that provide biochemical cues to modify the *in vitro* microenvironment and facilitate development of differentiated tissue, suggesting the viability of a skeletal muscle construct in a biofunctionalized scaffold [48].

In this study, we used the C2C12 skeletal muscle progenitor cell line, established for the exploration of stem cell use for regenerative purposes upon grafting or transplantation [130], to engineer 3D muscle constructs. Previous work has shown that specific ECM molecules, such as laminin[131], collagen [132], fibronectin [133] and RGD [134] modulate the proliferation and differentiation of C2C12 cells. Past research utilizing C2C12 cells to generate muscle strips involved use of micropatterned substrates to induce cell alignment [135] and multilayering of cells on PDMS [136]. However, the use of non-degradable substrates limits these designs to two dimensions. Therefore, efforts centered on seeding myogenic cells in 3D scaffolds [89, 138] or microthreads [87], differentiating high-density myogenic cell pellets [139], cell sheet tissue engineering [92] and thermoresponsive polymer substrates for 3D oriented sheets of myotubes myotubes [90] have been explored to yield 3D constructs. However, these studies did not directly examine the influence of the scaffold and/or biological functionalization on myogenic

differentiation in a controllable manner. Naturally occurring biological hydrogels are a popular choice, due to their resemblance to native tissue. Fibrin [87, 88], alginate [89], gelatin [90], and collagen [92, 93] have been explored as matrices for muscle constructs using C2C12 cells, but these hydrogels are limited in terms of precisely controlling their properties, processing and biofunctionality.

Synthetic scaffolds such as hydrogels show great promise for modulating bio-architecture, as multicomponent polymer matrices can be created by exploiting simple physiological reaction mechanisms [75]. The resulting 3D swollen hydrogels provide tailorable platforms that support cellular activities to a similar extent to native matrices. For this work, we utilized an engineered biofunctionalized poly(ethylene glycol)–(PEG) hydrogel with maleimide (MAL) crosslinking reaction chemistry, which gels rapidly, with high reaction efficiency, under cytocompatible reaction conditions (Figure 5) [12]. The PEG backbone has low protein adsorption, a minimal inflammatory profile, well-established chemistry and a long history of safety *in vivo*. The PEG–MAL system in particular allows modular design variation, control over polymerization time and small and non-toxic/non-inflammatory degradation products that are excreted via the urine [161, 162]. This paper focuses on engineering a PEG–MAL hydrogel microenvironment to promote the development of differentiated contractile muscle tissue from skeletal muscle progenitor cells. The goal of this research was to generate a dense, yet self-sustaining, cell–hydrogel composite with high cell viability and potential for proliferation and differentiation to develop a functional muscle strip. To this end, we examined the effects of hydrogel polymer weight concentration, adhesive ligands and growth and differentiation medium conditions in the development of a skeletal muscle construct.

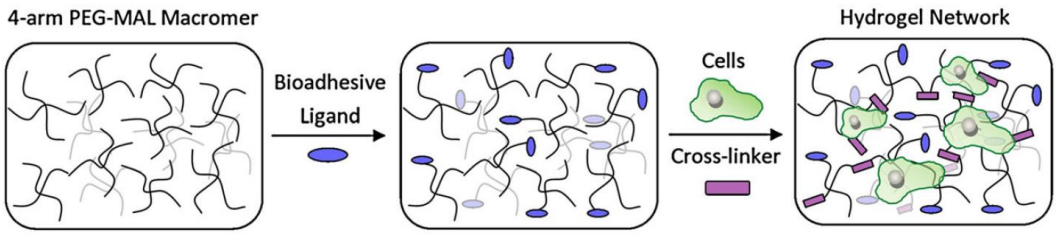

Figure 5: Formation of a hydrogel network to support encapsulated cells for tissue formation. PEG–MAL hydrogel network formation with encapsulated cells utilizing four-arm PEG–MAL macromer functionalized with bioadhesive ligand and crosslinker peptides

Materials and Methods

Cell culture

Skeletal murine myoblasts C2C12 cells were obtained from ATCC (Manassas, VA, USA). Dulbecco's modified Eagle's medium [DMEM; 4.5 g/l D-glucose, L-glutamine (+), sodium pyruvate (–)], insulin–transferrin–selenium (ITS-X), Dulbecco's phosphate-buffered saline (PBS), penicillin/streptomycin, trypsin/EDTA and fetal bovine serum (FBS) were obtained from Life Technologies (Carlsbad, CA, USA). Horse serum was supplied by Hyclone (Logan, UT, USA). Cells were cultured in 20% FBS and 1% penicillin/streptomycin in DMEM (growth medium, GM) until passage 4, prior to hydrogel encapsulation, and further growth and differentiation in 2–10% horse serum (HS), 1% ITS-X and 1% penicillin/streptomycin in DMEM (differentiation medium, DM).

Cell encapsulated hydrogel fabrication

C2C12 cells were encapsulated in collagen-I (3 mg/ml; BD Biosciences, San Jose, CA, USA) or protease-degradable PEG-based hydrogels, prepared as previously

described (Figure 5) [12]. PEG–maleimide (PEG–MAL) four-arm macromers (20 kDa, > 95% maleimide functionalization; Laysan Bio, Arab, AL, USA) and custom-synthesized peptides (AAPPTec, Louisville, KY, USA) were used. PEG–MAL macromers were prefunctionalized with GRGDSPC (RGD) adhesion peptide or GRDGSPC (RDG) non-bioactive ligand in 2.0 mMtriethanolamine (TEA) solution for 30 min. PEG polymer density was varied in the range of 4–6% w/v, and RGD or RDG density was maintained at 2.0 mM. The precursor molecules and cell suspension solution (for a final concentration of 0.1–10 × 10^6 cells/mL) were crosslinked into a 40 µl hydrogel by the addition of a cysteine-flanked protease-degradable peptide sequence, GCRDVPMSMRGGDRCG (VPM), for 15 min. The concentration of crosslinker peptide was proportional to the macromer concentration in order to react with the appropriate number of maleimide groups in the macromer and generate a fully crosslinked hydrogel network. The cast hydrogels had a 5.0 mm diameter × 2.0 mm thickness. The hydrogels were left to swell in growth medium overnight, and the medium was changed daily. The resulting gel phase is transparent, which allows visualization of cellular activity without disruption of the cellular microenvironment.

Live/dead and immunofluorescence staining and image analysis

Hydrogels containing encapsulated cells to be analysed for cellular viability were incubated in PBS for 10 min to remove serum, followed by the live/dead stains calcein AM (2 µM) and TOTO-3 iodide (2 µM) (Life Technologies, Carlsbad, CA, USA) for 10 min. Samples stained for sarcomeric myosin, as an indicator of differentiation, were fixed in 4% methanol-free paraformaldehyde for 30 min at room temperature, permeabilized and blocked with 0.5% Triton X-100 in 1% bovine serum albumin (BSA;

Sigma-Aldrich, St. Louis, MO, USA) before being incubated with primary antibody. Monoclonal antibodies against sarcomeric myosin (MF20, 1:200) and Troponin-T (CT3, 1:100) were obtained from the Developmental Studies Hybridoma Bank, Iowa City, IA, USA. Secondary antibody AlexaFluor 488-conjugated anti-rabbit IgG and DAPI were obtained from Life Technologies (Carlsbad, CA, USA) respectively. Gels were incubated in antibody solutions (10 and 1 μg/ml for secondary antibody and DAPI, respectively) overnight at room temperature and rinsed thoroughly between all steps in PBS containing 0.05% Triton X-100 and 1% BSA. The hydrogels were transferred into fresh PBS solution and imaged in Lab-Tek chamber slides, using a Nikon-C2 laser scanning confocal microscope with a × 20 air objective. Z-stack projections through 100–300 μm thick sections of the hydrogels were rendered. Individual slices/image were analyzed using customized macros on ImageJ software (NIH, Bethesda, MD, USA), and projected into maximum-intensity images for the purposes of illustration. For samples stained for live/dead, the fractional viability was calculated as the number of live cells/total cells. The number of cells stained positively for Calcein (live only) was divided by the number of cells stained positive for TOTO-3 iodide (dead only), plus the number of Calcein - positive cells. Projected spread area was determined as the total area occupied by Calcein stain. For samples stained for sarcomeric myosin and DAPI, percentage differentiation was calculated as the number of cells stained positive for myosin over the total number of cells/imaged plane. Number of multinucleated cells and number of nuclei/differentiated cell were determined using binary layers, applied with Nikon Instruments Software (NIS)-Elements. Image slices were chosen from stacks at 10 μm (*z* axis) intervals, to avoid counting the same cells more than once using ImageJ and NIS-Elements. For

multinucleation analysis, the NIS-Elements software was used to distinguish between DAPI and sarcomeric myosin by application of layers to individual image slices. In very few instances, images were discarded because multinucleated cells were found in close proximity to each other, resulting in poor discrimination by the program. Live/dead images were taken in LiveCell System (Pathology Devices, Westminster, MD, USA). All images were taken at the same settings and subjected to consistent threshold values during image processing.

Muscle contractility assay

To induce gel contraction, a stimulant solution (5 mM $CaCl_2$, 5 mM $MgCl_2$, 100 mM KCl, 5 mM EGTA, 1 mM ATP in PBS, pH 7.4) was used. Hydrogels in saline were used as controls. All gels were placed in 200 µl test solution and immediately extruded unidirectionally, using a transfer pipette, onto parafilm adhered to ruled paper. The change in length of the hydrogel along the horizontal axes was observed for up to 15 min, although no visual changes were observed after the first 5 min.

Statistics

Data are expressed as mean ± standard error of the mean (SEM). Statistical analysis was performed using *t*-test for comparison of two different groups, one-way ANOVA for comparisons among different groups, and two-way ANOVA for comparisons between different groups at different time points, using GraphPad Prism software. Significance was set at $p < 0.05$.

Results

Cell-seeding density influences encapsulated C2C12 cell viability and spreading

To generate cell-laden hydrogels, four-arm PEG–MAL macromers were functionalized with RGD and cells, followed by crosslinker, were added to form a gel (Figure 5). To create a functional, dense, hydrogel–tissue composite without vasculature, it was necessary to identify a cell density that would be high enough to promote sustained cell survival, as a prerequisite for cellular differentiation into skeletal muscle-like tissue. Initial cell encapsulation was confirmed to be uniform in a 3D field of view, according to live/dead staining with laser-scanning confocal microscopy (Figure 6).

Different cell suspension concentrations were explored, in the range 0.1×10^6–10×10^6 cells/mL and constructs were stained for viability at days 1, 3 and 7, where day 0 is the day when the hydrogels were formed. The images in Figure 6B show similar levels of cell viability and spreading at day 1. However, after a week in culture, differences among seeding densities become evident and visual observation suggested that the highest survival was obtained at 4–8 × 106 cells/ml and was limited in gels seeded with 0.1, 1.0 and 10×10^6 cells/mL.

Figure 6C shows quantification of live cells within gels, showing time- and cell density-dependent differences. The overall percentage of live cells decreased from day 1 to day 3 and was restored by day 7, with the exception of the lowest cell-seeding density. Whereas significantly different from other groups, the 4 and 8×10^6 cells/mL were not significantly different from each other at days 1 or 3. By day 7, the 8×10^6 cells/mL

group was significantly different to all other conditions ($p < 0.05$). Cell spreading and extension of cell processes were assessed as projected spread area (Figure 6D). In general, the spread area decreased from day 1 to day 3, corresponding to decreases in the percentages of live cells, but then increased from day 3 to day 7. Whereas significantly different from other groups ($p < 0.05$), the groups for 4 and 8×10^6cells/ml were not different from each other at days 1, 3 and 7.

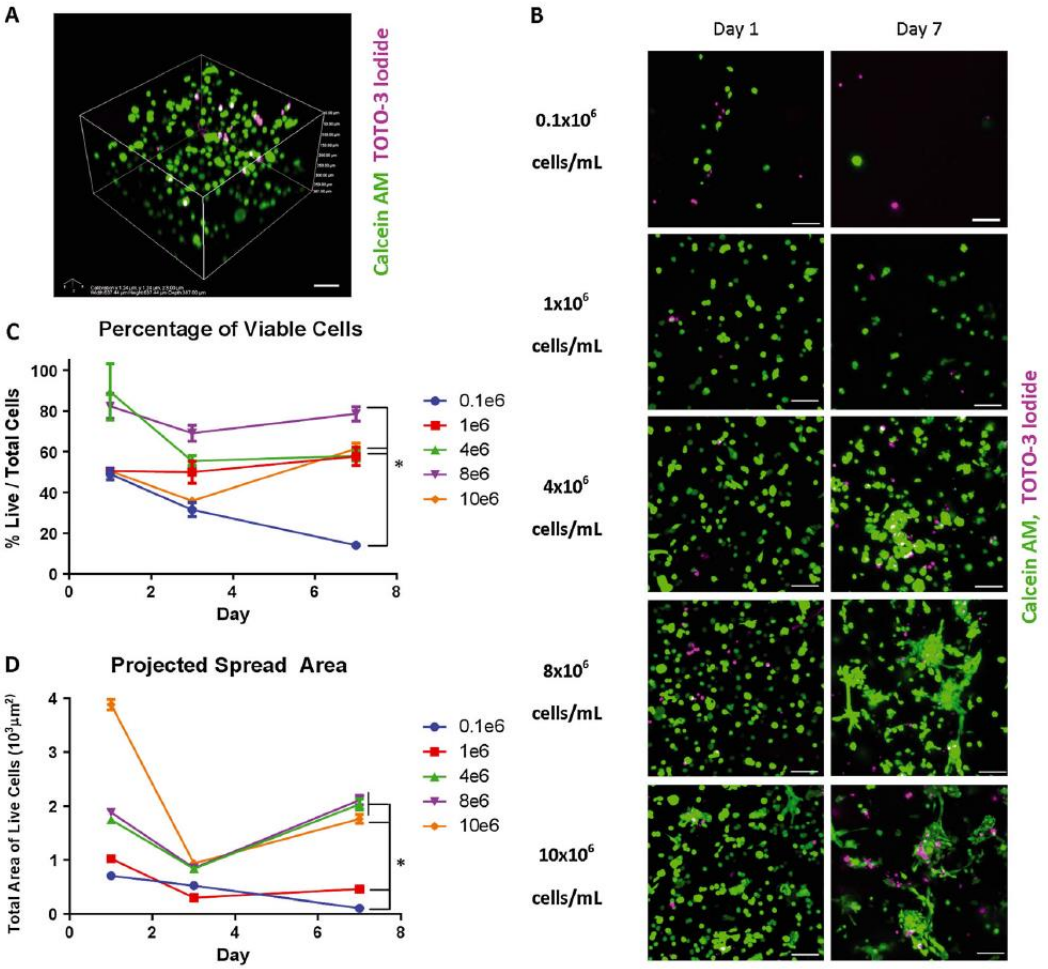

Figure 6: Viability of C2C12 cells in 3D hydrogels to varying cell seeding densities. (A) Volume view of 400 µm stack of live/dead staining to show uniform cell seeding density throughout gel seeded at 8 × 106 cells/mL. (B) Representative maximum intensity projection confocal images stained for live/dead. (C) Highest percentage of viable cells existed in gels seeded with 8 × 106 cells/mL (~79%), with a significant difference between 8 × 106 and 10 × 106 densities and all other conditions at day 7. (D) Projected spread area occupied by live-cell stain is quantified as extent of spreading. All scale bars = 100 µm. $n \geq 5$/condition/time point; *$p < 0.05$

The greater projected spread area for 10×10^6 cells/mL throughout culture was related to the higher seeding density and the difficulty of using image analysis methods in this case to distinguish the two.

These data indicate a threshold for the concentration of cells that remain viable within a 40 µl hydrogel in the absence of a vascular network or convective culture conditions.

As contact-dependent cells, C2C12 cells require a seeding density enabling intracellular interactions to mediate survival [166], which the densities of 0.1 and 1×10^6 cells/mL are unable to provide. In contrast, at 10×10^6 cells/mL, increased competition for nutrients and space results in lower levels of sustained survival. Hence, the 8×10^6 cells/mL cell seeding density was chosen thereafter as a concentration with the greatest potential for dense tissue exhibiting low levels of long-term cell mortality.

Polymer weight percentage influences encapsulated cell viability

It has been shown that matrix elasticity provides biophysical cues that impact skeletal muscle stem cell behavior, such as viability and lineage commitment [77, 78]. Varying the weight by volume proportion of polymer in the hydrogel modulates matrix elasticity, as well as crosslink density, rate of gel degradation and permeability for soluble factors. The range 0.45 kPa at 4 w/v% to 0.8 kPa at 6 w/v% Phelps et al., 2012 was selected on the basis of preliminary studies, which showed variations in C2C12 development dependent upon alterations of the polymer weight percentage used. To quantify C2C12 response to hydrogel weight percentage (w/v%), we assessed the fraction of live cells in PEG hydrogels of various w/v% and a 3 mg/ml collagen type I gel (as a reference to natural matrices) at days 1, 3 and 7 (Figure 7). Fractional values calculated at days 3 and 7 were normalized to day 1 values for each condition (Figure 7B). A fractional value of 1.0 at day 1 reflects the highest levels of viability observed 24 h after encapsulation for that polymer w/v% condition. By day 7, the viabilities of cells in 5% PEG and collagen gels were not significantly different from each other, but were observed to be significantly higher than the rest of the groups ($p < 0.05$). Importantly, 5% PEG hydrogels supported higher levels of viability compared to 4% and 6% hydrogels,

showing an optimal polymer weight concentration for C2C12 culture in 3D. The lower viability for 4% hydrogels can be attributed to its weak mechanical structure from fewer crosslinks. Fewer protease-degradable crosslinks allow faster cell-mediated matrix degradation and loss of the physical scaffold. Conversely, the 6% hydrogels probably supported lower cell viability due to decreased permeability arising from the higher polymer network density. As previously described, the presence of protease-degradable sites in appropriate concentrations play a key role in cell viability and differentiation (Patterson and Hubbell, 2010; Phelps et al., 2012. In this case, fast-degrading VPM crosslinker at the concentration used to form networks with 5 w/v% PEG–MAL–RGD enables cells to remodel their microenvironment at a time scale appropriate for promoting C2C12 cell viability and proliferation, as precursors to differentiation.

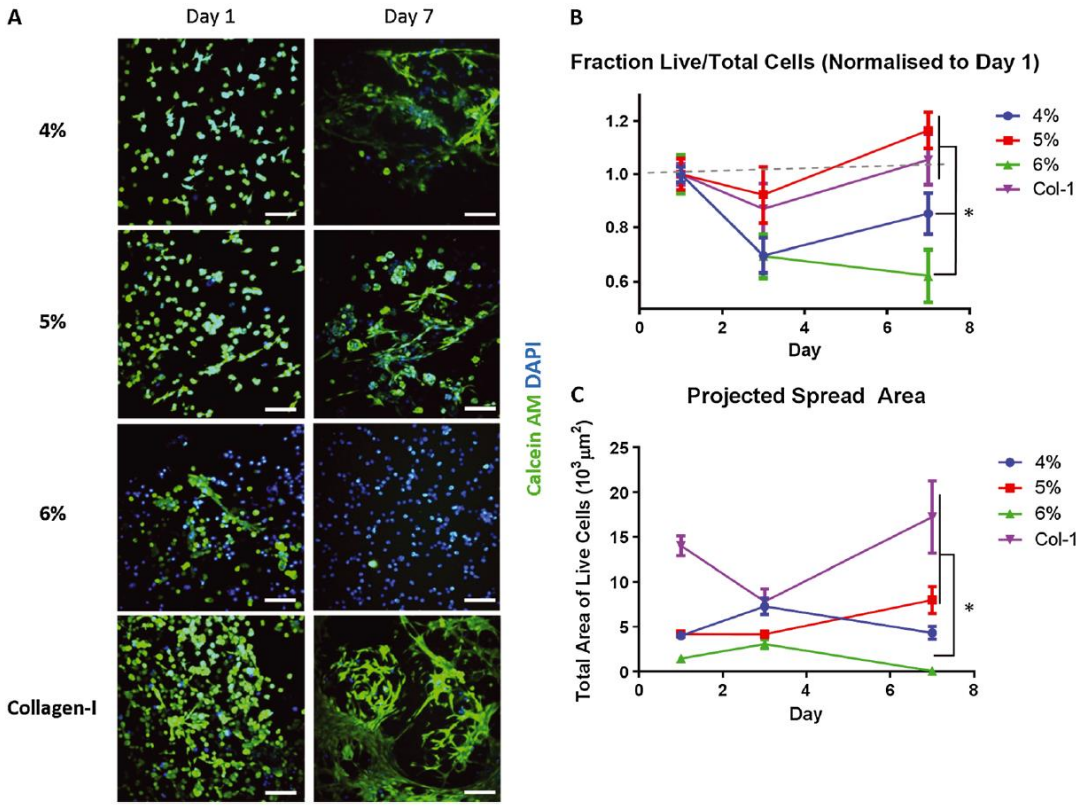

Figure 7: Viability response of C2C12 cells in 3D hydrogels to varying polymer weight percentage. (A) Representative maximum intensity projection images of live/total cell stains in gels of varying polymer percentage and collagen type-I, used as a biological control. (B) Fraction of cells alive shows differences between 5% gels compared to 4% and 6% gels at day 7. No differences between collagen type-I and 5% gels was found. (C) Projected spread area occupied by live-cell stain is quantified as the extent of spreading, showing differences among gels at day 7. All scale bars = 100 µm, $n \geq 5$/condition/time point; *$p < 0.05$

Skeletal muscle constructs require bio-adhesive cues within the scaffold to promote cell viability

To examine the impact of a bioadhesive ligand within the synthetic hydrogel environment, two peptides were used: the active RGD peptide from fibronectin, as a bioactive ligand to induce adhesion; and the scrambled RDG peptide, as an inactive substitute that would not alter hydrogel structure. 5% PEG and 3 mg/ml collagen type I hydrogels (as a reference) were cast with a seeding density of 8×10^6cells/mL. C2C12

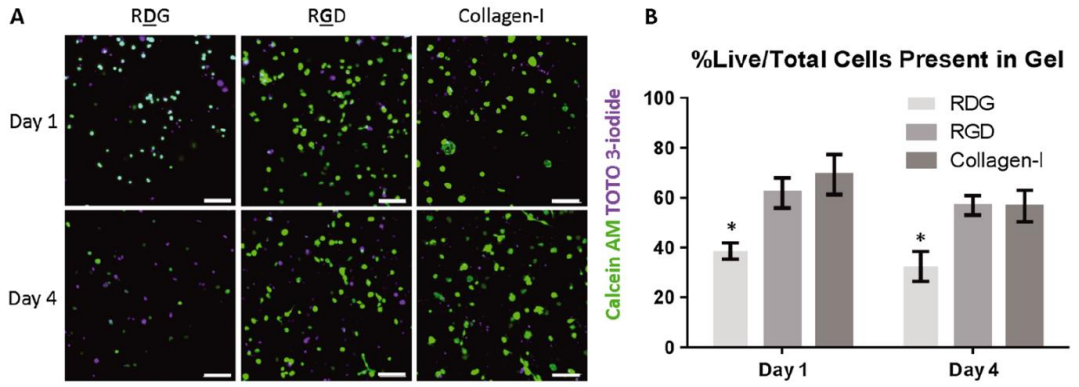

Figure 8: Viability of C2C12 cells in 3D hydrogels in the presence and absence of bioadhesive ligands. (A) Representative maximum intensity projection images of live/dead cell stains in gels presenting RDG (non-adhesive), RGD (adhesive) peptides and collagen type-I, used as a biological control. (B) Percentage viable cells analysis shows differences between RDG and collagen-I groups, suggesting that cell viability is maintained in the presence of bioactive ligands. All scale bars = 100 μm; *$p < 0.05$

mouse myoblasts showed high viability in the presence of RGD in a manner comparable to that of the natural collagen matrix. Significantly reduced viability was observed in RDG gels (Figure 8). These results demonstrate the need for cell–matrix adhesion, demonstrated with RGD in the synthetic environment.

Horse serum concentration in differentiation medium influences the extent of C2C12 differentiation

Determining the specific conditions that supported cell survival for up to 7 days was considered a prerequisite to studying the differentiation potential. Serum deprivation is a common approach to forcing myoblasts to exit the cell growth cycle and begin differentiation into skeletal muscle cells (Lawson and Purslow, 2000). We therefore examined the extent of differentiation for different serum concentrations in the culture medium, as quantified by: (a) degree of maturation, reflected in the number of cells expressing muscle-specific proteins divided by total number of cells ('% differentiation');

and (b) degree of fusion, analysed as the number of multinucleated cells and number of nuclei/cell stained positive for differentiation markers (Bajaj et al., 2011).

Using the hydrogels in which C2C12 myoblasts showed good viability (5% PEG, 2.0 mM RGD, 8×10^6 cells/mL), up to 75% of cells were found to be differentiated over a period of 4 days in differentiation medium (DM) when the DM was supplemented with 2% HS. Figure 9A, B shows immunofluorescence staining for sarcomeric myosin and troponin, used to assess differentiation markers, while Figure 9C, D shows quantification by image analysis. The percentage of differentiated cells in 2% HS was significantly different from other groups ($p < 0.05$). Low serum concentration conditions (0%, 0.1%) produced lower differentiation, with a maximum of approximately 60%, while high serum concentration (10%) resulted in the lowest levels of differentiation (30%) amongst

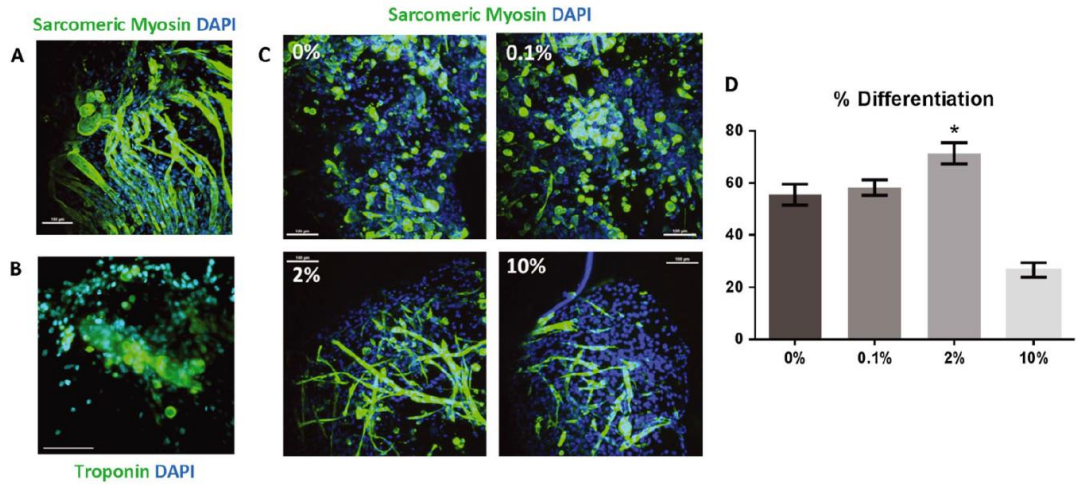

Figure 9: Differentiation of C2C12 cells, as indicated by sarcomeric myosin and troponin expression is modulated by horse serum (HS) concentration in differentiation medium (DM): (A) presence of sarcomeric myosin; (B) troponin indicates differentiated skeletal muscle; (C) representative images of myosin and DAPI stain show that 2% HS concentration in DM improves the extent of differentiation, indicated by self-assembly and alignment of myotubes; (D) percentage differentiation is quantified as cells positive for differentiated marker out of total nuclei; > 75% cells were differentiated in 2% HS, significantly more than 0%, 0.1% or 10% HS samples. All scale bars = 100 µm; *p < 0.05

all the groups tested. These results demonstrate an optimal serum concentration for differentiation. We attributed the lower differentiation for low serum concentrations to reduced cell viability, and the reduced differentiation in high serum concentrations to enhanced proliferation, which is antagonistic to differentiation. Hence, the impact of modifying soluble factor cues should be considered while engineering differentiated skeletal muscle tissue, and 2% HS was found to be optimal for this system. These results also show that differentiating skeletal muscle myoblasts and multinucleated cells possess the intrinsic ability to self-align in the absence of direct topographical cues (Figure 9A).

Incubation period in growth medium prior to differentiation modulates the extent of C2C12 differentiation

We observed that the extent of myogenic differentiation varied with the incubation time in growth medium (GM) prior to induction of differentiation. To further examine these effects, we experimented with different incubation periods prior to using a fixed 4 day differentiation protocol, where the DM contained 2% HS. Gels were created as previously determined with 5% PEG, 2.0 mM RGD and 8×10^6 cells/mL. Zero-day incubations (0 days) refers to hydrogels that were cast and immediately transferred to DM. Figure 10A, B shows the benefit of an incubation time longer than 1 day, with an upper limit being reached at a 5 day incubation period, due to gel degradation and handling difficulties; 3 days in GM allowed the cells to reach differentiation levels exceeding 50%, which was significantly different to all other conditions ($p < 0.05$). The formation of multinucleated myotubes was analysed, as shown in Figure 10C, to show the number of multinucleated cells/unit area and the extent of multinucleation/cell

(Figure 10D, E). A 3 day incubation period resulted in the highest levels of multinucleated cells and extent of multinucleation/cell. An average of eight multinucleated cells/μm^2 was observed, with at least two nuclei/cell. These results show that controlled growth and differentiation conditions, in combination with microenvironmental cues provided by the hydrogel, regulate C2C12 cell survival and eventual differentiation into self-aligning myotubes. In summary, biological and physical properties essential to skeletal muscle, shown by the degree of maturation and degree of fusion, respectively, can be engineered into synthetic hydrogel systems.

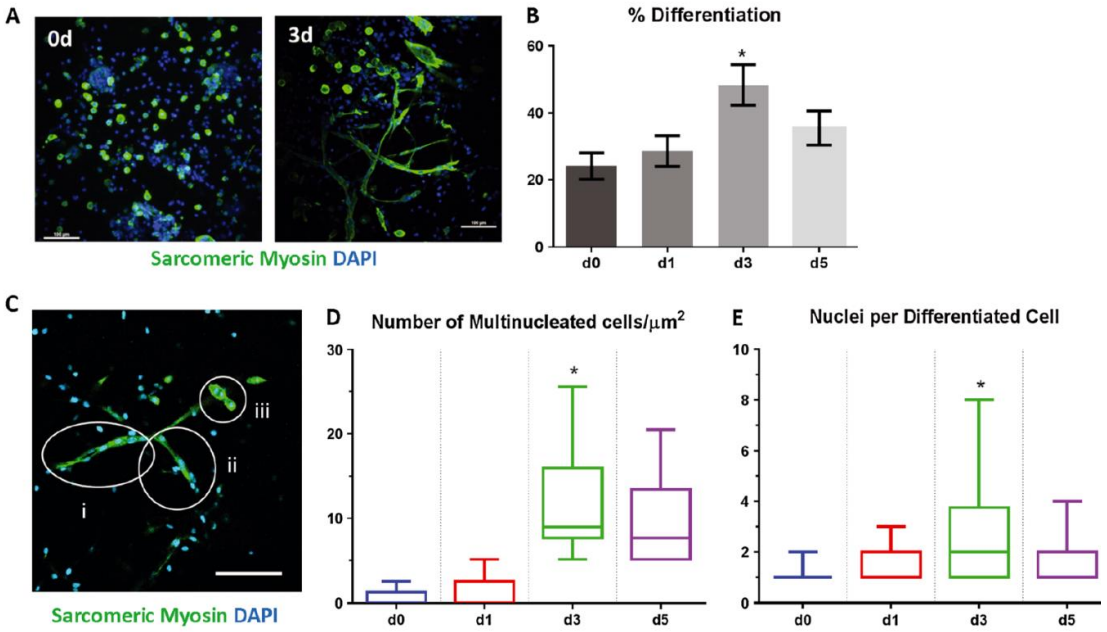

Figure 10: Differentiation of C2C12 cells as indicated by sarcomeric myosin expression is modulated by incubation time in growth medium (GM) prior to 4 days in DM: (A) representative maximum intensity projection images of myosin and DAPI stain show that 3 days in GM improves extent of differentiation, indicated by self-assembly and alignment of myotubes; (B) percentage differentiation is improved (~55%) and significantly different in 3 day-incubated samples compared to 0, 1 or 5 days of incubation; (C) schematic of analysis for multinucleation extent, as assessed by number of multinucleated cells/unit area and number of nuclei/multinucleated cell (i = 7, ii = 5, iii = 3); (D) images obtained from GM incubation were also analysed for multinucleation extent, as described previously. Differences between 3 day incubation and all other groups with regards to both metrics was found. All scale bars = 100 µm; *$p < 0.05$

Hydrogel with differentiated cells exhibit contraction under external stimuli

Hydrogels with encapsulated cells differentiated under the previously described methodology were exposed to a contractile stimulant or PBS control before being immediately extruded into a rod-like shape (Figure 11). Changes in length were measured over a 15 min period, but no additional changes were observed beyond 5 min. In contractile solution, the extruded hydrogels began to decrease in length instantly. The average reduction in length was $18.4 \pm 2.75\%$ ($n = 6$), which was significantly different to the hydrogels in PBS, which decreased in length by $7.2 \pm 3.15\%$ ($n = 4$, $p < 0.05$). Cell-free hydrogels did not contract upon exposure to contractile agonist or in the presence of PBS control. Although the myoblasts are not provided with direct signals for alignment and differentiate in random directions, they are functional by their ability to contract and reduce the length of an extruded hydrogel. These results demonstrate a simple functional response of the differentiated skeletal muscle cells acting upon the hydrogel constructs in response to contraction-inducing conditions.

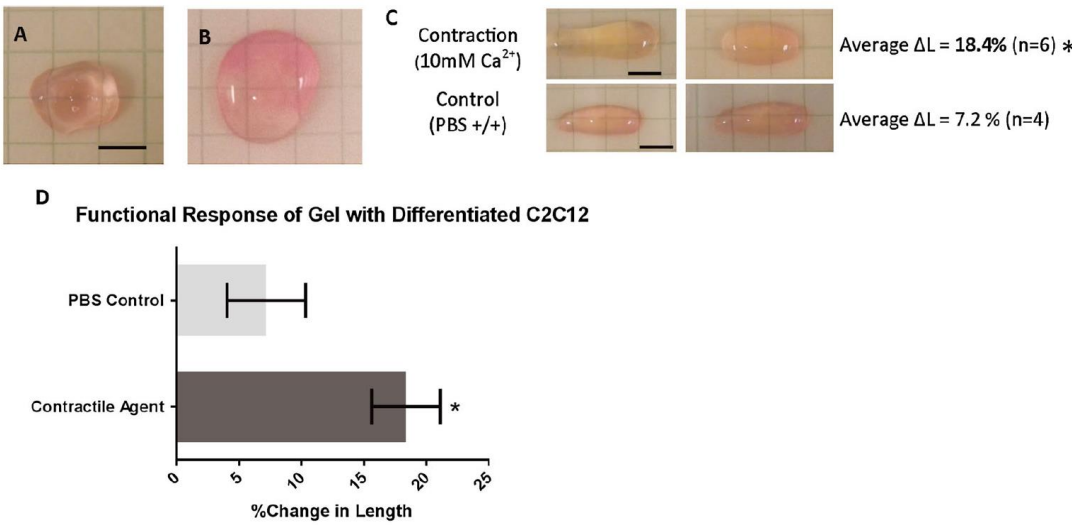

Figure 11: Functional response of 3D gels containing differentiated C2C12 cells to contraction-inducing conditions: (A) initial gel removed from solution; (B) gel in 100 µl testing solution for 10 s, followed by immediate extrusion using transfer pipette; (C) contraction was induced using appropriate solutions; gels in contraction solution shortened in length (horizontal dimension); (D) quantification of contraction as a result of contractile agent or PBS control (SD); images at t = 0 and 5 min; no changes in length were observed after 5 min; scale bar = 0.5 cm; *p < 0.05

Discussion

Limited treatment options for skeletal muscle repair have entailed exploration into regenerative biomaterials that encourage muscle cell growth, proliferation and differentiation *in vitro*. In particular, synthetic hydrogels can be controllably engineered to design a microenvironment that directs cell fate. We identified an optimal hydrogel formulation of 5% w/v four-arm PEG–MAL macromers functionalized with 2.0 mM RGD adhesion peptide, and crosslinked by a MMP-degradable peptide that supports C2C12 mouse myoblast proliferation and differentiation. Additionally, 3 days of incubation in growth medium, prior to differentiation in 2% HS for 4 days, produced multinucleated cells that exhibited intrinsic alignment and demonstrated simple

contractility. We note that the range of parameters presented in this study was derived from either our experience with other cell types in this hydrogel system, or from pilot experiments that are not included in this report. Unlike their naturally derived counterparts, synthetic hydrogel properties can be precisely tuned to study matrix requirements of a cell from its environment. Characteristics such as matrix elasticity, permeability and degradability arise from the balance between polymer weight percentage and the required number of protease-degradable crosslinks necessary to form the gel. It has been shown that the interactions of a cell with its hydrogel surroundings can dictate decisions of cell fate. Hence, the ability to control the extent of these interactions with the modular design variation afforded by this PEG–MAL system allows us to examine and recapitulate properties necessary for tissue regeneration.

We posit that C2C12 cells require a certain amount of time to remodel the hydrogel for higher differentiation potential, hence exploring the incubation period for cell acclimatization. In this particular system, 0–1 days of encapsulation prior to DM results in insufficient remodelling and reduced differentiation potential. However, 5 days of incubation and greater remodelling also result in lower differentiation values, due to reduced mechanical integrity of the scaffold hydrogel. Such incubation times may have to be optimized for differing systems of hydrogels and cells, but should be regarded as an important consideration during *in vitro* tissue regeneration.

The original hydrogels were cast as discs of 5.0 mm diameter × 2.0 mm thickness. During culture, the hydrogels swelled significantly until day 3 and then decreased in volume until days 7–11, as the embedded cells proliferated and contracted the hydrogels. It should be noted that, for a system of this size, mass transfer is expected to occur by

diffusion, without enhanced transport due to convection or vascularization. Potential scale-up for therapeutic use will necessitate a mechanism for adequate nutrient and waste transport, comparable to native vasculature. Indeed, we have previously used similar PEG–hydrogel formulations to deliver the vasculogenic factor VEGF and establish a robust *in vivo* vasculature within the implanted hydrogel [80, 161].

While the hydrogel used in this study does not possess mechanical properties comparable to those of skeletal muscle or present physical cues, it does provide appropriate signals for the development and self-alignment of myotubes (Figure 9A) to begin to emulate native skeletal tissue. An inadequate degree of cell fusion and formation of self-aligned fibres limits the effectiveness of the current hydrogel system. Hence, future work will include investigation of topographical cues for directed alignment and improved contractile function. In addition, methods of incorporating vasculature are being considered to create self-sustained muscle actuators of greater dimensions. The hydrogel must be further engineered to support the infiltration of host cells, such as macrophages, fibroblasts and endothelial cells, while promoting vasculature through the release of growth factors or soluble mediators to promote cell survival and engraftment [167]. Beyond the development of skeletal muscle constructs for therapeutic applications, the use of synthetic hydrogels as scaffolds for the generation of muscle constructs provides an important step in engineering tailorable contractile units for cell-based actuators and machines.

C2C12 cells were employed as a well-characterized myogenic cell line and an established cell type to interface with neurons and use external signals for further studies. The techniques developed here can be translated to other cell lines, including human

primary or stem cell-derived cells, such that, in the future, an injectable or entirely *ex vivo* explant/transplant graft can be generated for restored functionality, wound healing or cosmetic surgery.

Conclusion

The goal of this study was to develop a scaffold as the first step towards building contractile muscle implants to mimic the cellular organization and physiological function of dense skeletal muscle, for the repair and replacement of lacking, diseased or damaged tissue. By modulating the compositional characteristics of a synthetic hydrogel, we identified key microenvironment cues to direct the adhesion, viability, growth, differentiation and formation of myotubes for functional skeletal muscle tissue constructs, as a regenerative solution to skeletal muscle loss, as well as a force actuator for cellular machines [9]. This study aims to add to the current knowledge of cooperative cellular behavior, leading to a deeper understanding and possible recapitulation of the organization of larger structures found in nature.

Acknowledgements

We acknowledge helpful suggestions from Ted T. Lee and Edward A. Phelps, for imaging optimization and cell encapsulation, respectively. The myosin, sarcomere and troponin monoclonal antibodies were obtained from the Developmental Studies Hybridoma Bank, developed under the auspices of the NICHD and maintained by the

University of Iowa, Department of Biology, Iowa City, IA 52242, USA. This study was supported by the National Science Foundation under the Science and Technology Center Emergent Behaviors of Integrated Cellular Systems (EBICS; Grant No. CBET-0939511).

CHAPTER IV: TOROIDAL SHAPE PROVIDES GEOMETRIC CUES TO ALIGN MYOBLASTS WITHIN HYDROGEL CONSTRUCTS THAT DEMONSTRATE FUNCTIONAL CONTRACTION IN RESPONSE TO EXTERNAL AGONISTS

Abstract

Cellular alignment is crucial for the development of differentiated myotubes that support contractile machinery for functionality of in vitro generated constructs. Previous works to introduce anisotropy in 3D tissues have utilized geometric cues on scaffolds printed with microarchitecture for cell guidance, or utilized naturally-derived materials in combination with mechanical and electrical stimulation signals. Of the synthetic scaffolds available, hydrogels show great promise for modulating bio-architecture, as multifunctional polymer matrices can be created for highly viable cell populations after encapsulation [75]. The first goal of this study was to identify geometric cues for biofunctional poly(ethylene glycol) (PEG)-maleimide (MAL) hydrogels to prompt directed alignment to encapsulated cells in vitro. We found that toroidal shaped constructs (generated by casting the hydrogel around spires of defined sizes) containing C2C12 skeletal myoblasts increase cell viability and alignment over time compared to free floating or linear hydrogel constructs. Meanwhile, demonstration of functionality is essential for the development of skeletal muscle constructs intended for use in tissue engineering or soft robotics. Previously, constructs at this size scale have utilized secondary structures for the measurement of force as a result of the deflection of a construct anchor. The second goal of this study was to directly measure the forces generated by toroidal hydrogels of aligned cells, upon action of external agonists, using a

custom built setup and analysis method. We found that the 1.0 mm spire-toroids generated the highest alignment, as quantified using an alignment index, compared to other spire-toroid sizes. In addition, the 1.0 mm spire-toroids produced the greatest contractile force of 46.8±7.9 μN upon activation with a 50 mM caffeine solution, and this contractile force was completely abrogated in the presence of contractility inhibitors. Hence, we demonstrate a positive correlation with extent of alignment and efficiency of contraction. Overall, these two goals are aimed at developing alignment and demonstrating contractile functionality within skeletal muscle engineered constructs. Additionally, the techniques described here can be translated across cell and tissue types to further the exploration of biomaterials for tissue engineering.

Introduction

Uniaxially aligned myotubes that contain developed sarcomeric contractile machinery are key characteristics of skeletal muscle tissue [163]. For this study, we utilized previously generated biofunctional hydrogels to examine strategies to (1) promote cellular alignment and (2) measure contractile function. Typical in vitro strategies for skeletal muscle tissue engineering (SKMTE) utilize biomaterial substrates with added cells until the tissue has evolved into a functional form that can be transplanted in vivo or controlled by external stimulation [47, 123, 139, 145, 168-172].

Challenges to generating mature and contractile constructs are multifold [8]. First, the construct must be able to withstand physical handling while maintaining a high concentration of differentiated, fused and aligned cells. Tractability is important as it enables the construct to be easily subjected to methods of preparation for microscopy,

visualization, and mechanical testing in vitro without relying on the support of an external substrate with different material properties that can confound force production results or make it difficult to directly measure force from the tissue itself. In addition, a tractable construct is more suitable for in vivo implantation. Although injectable hydrogels have been explored, their efficacy in skeletal muscle cell delivery has not been demonstrated as frequently as their ability to repair cardiac muscle, or deliver growth factors for limited skeletal muscle regeneration [104, 162, 173, 174]. Second, the construct needs to be amenable to mass transport by diffusion in the absence of well-defined vascularization [175]. Third, the engineered tissue must be functionally able to generate physiologically relevant forces [176].

Biomaterial scaffolds are an important factor in muscle construct development as they enable the modulation of encapsulated cell behaviors through physical or biochemical cues, spatiotemporal drug release, and protection from immune response due to injury. These functional properties can be achieved by a combination of features, including the choice of biomaterial, its 3D architecture, chemical composition, functionalization with biological molecules, biodegradability, mechanical and physicochemical properties [8]. In the previous chapter, we established that synthetic PEG scaffolds provide a consistent, modularly controllable starting material for myotube differentiation. We previously showed engineering a specific microenvironment for C2C12 mouse skeletal myoblasts and modulating growth conditions would enable the development of biofunctional hydrogels for skeletal muscle constructs, here we examine the application of geometric cues on the development of alignment and consequent functionality [6]. We understand the limitations of using cell lines in replicating in vivo myogenesis, yet the widespread

use of C2C12 myoblasts and their ease of use make them an ideal choice for technology development platforms such as those described in this study. Furthermore, we have established the PEG-MAL material to be a suitable delivery system for in vivo use (Appendix A,[162]).

Typically, biomaterials can promote cellular alignment in static or dynamic form. Static physical cues include (i) topographical cues on flat, two dimensional (2D) surfaces [177-180], from which a cell-scaffold construct of several uniformly aligned layers can be constructed [136]; (ii) 3D anisotropic scaffolds generated prior to the addition of cells, such as electrospun fibrous meshes [87, 181], or anisotropic porous scaffolds [182], which promote alignment within the construct during development [105, 123, 168].

2D approaches to alignment are limited due to the production of cellular monolayers that cannot deliver the required tissue thickness for physiological functionality. Additionally, aligned monolayers cultured using contact guidance such as microcontact printing (μCP) of parallel grooves on a planar surface, are not easily separated from their substrate while maintaining physical integrity [177, 178]. The ability to strip monolayers from substrates is important to further process 2D tissues into 3D constructs for long-term stability and physiological relevance [115].

Millimeter scale, 3D skeletal muscle constructs have been engineered by embedding cells in scaffolds that contain anisotropic cues, often created using electrospinning [87, 181]. Constructs have also been generated as anisotropic sheets using custom designed molds with intermittent polygonal posts to create porous networks of skeletal muscle [123]. Cylindrical tissue constructs such as myooids or bioartificial muscle (BAMs) were produced without scaffolds through the self-organization of muscle and fibroblast co-

cultures. Muscle fascicles [169], microtissue gauges (μTUGS) [183], and myooids [121] demonstrate that it is possible to engineer functional 3D skeletal muscle as a linear muscle bundle with anchor points on two ends and a roughly circular cross-section, similar to that found in vivo. Fascicles and μTUGS are limited for use in practical or medical application due to their small-scale thickness of around 100 μm and lack of scalability potential. Other limitations of previously generated 3D constructs involve the use of anchorage for support, base elastomer for stability, and the use of naturally derived scaffold materials. Ideally, anchorage in SKMTE would be sufficient to induce tension as a static geometric cue or behave as conduits for dynamic stimulation. The use of least two anchorage points to provide mechanical stability and tension for aligning cells necessitates the design of a custom functional measurement setup [123, 132]. Yet the support provided should be amenable to removal on-demand, to allow facile detachment of the construct for use in contraction analyses or in vivo transplantation. Lastly, developed 3D constructs are constrained by size to 1 mm or less due to the absence of a vascular network [115]. The resulting diversity in the exploration of SMTE constructs and measurement devices complicates comparisons between labs that likely use different materials and cell sources.

In terms of actuators developed for soft robotics, many structures consist of 2D layers of cells attached to a flexible elastomer, such as PDMS, that provides structural support and basal attachment for the cells as contractility is explored [10]. Resulting constructs adhere strongly to their elastomeric base materials and separation is not presented as possible, or important, though necessary for translation to tissue engineering applications.

Dynamic signals for inducing alignment and myofiber hypertrophy include electrical stimulation [153, 184-188] or cyclic mechanical stretching [189, 190]. Electrical stimulation depolarizes the myotubes, causing contraction and mechanical stress that increase differentiation, alignment, and force generation [186]. Although these approaches improve morphology, force production and tissue density are still not comparable to native skeletal muscle: the peak stress generated was 60–120 Pa, considerably less than the 100 kPa and higher stress of native skeletal muscle [115, 147]. Meanwhile, several limitations accompany the continuous excitation of cell culture using electrodes, such as electrolysis of the media, consequent heating, pH changes, and electrode corrosion. Contactless and miniaturized electrodes are being explored to combat these issues but with limited success [191, 192].

Mechanical signals have been shown to increase force generation through the improvement of cellular anisotropy, increase in the myofiber diameter and relative cross-sectional area compared with controls [186, 190, 193-195]. Work with C2C12 myoblasts prior to differentiation has shown mechanical signaling, through cytoskeletal remodeling, had significantly greater impact on alignment than electrical stimulation due to the lack of excitation-contraction mechanism development [196]. Dynamic, or cyclic, mechanical signals are created by stretching muscle constructs using an externally applied load, in a distinctly different manner than the mechanical stresses experienced as a secondary feature of electrical stimulation signaling. Further improvements to muscle construct alignment and force generation may be possible by changing the mechanical or electrical stimulation patterns, exploring drug release for hydrogels or taking a step back and improving the biomaterial from which the constructs are engineered [197]. Accordingly,

while the use of stimulation is an important tool, the availability of a simpler solution, such as biomaterial modification, may provide a facile and reproducible strategy without extensive custom equipment or stimulation profiles. Using fewer cues at initial stages may also force cells to rely on their inherent properties to align [6], which may be enhanced or developed further through the addition of dynamic signaling.

The first goal of this study was to further develop our cell–hydrogel composite to promote cellular alignment for the development of a functional muscle strip. To this end, we explored the utility of simple geometrical constraints that provide mechanical cues during fabrication of the cell-laden construct to align myotubes by utilizing the intrinsic ability of skeletal muscle cells to grow, differentiate, and fuse without excessive external aides. We used the C2C12 skeletal muscle progenitor cell line, encapsulated in biofunctional hydrogels cast with a spire mold to generate a toroidal shaped gel configuration for circumferential alignment (Figure 12). The resulting 3D swollen hydrogels provide tailorable platforms that support skeletal muscle progenitor cell alignment. We examined the effects of different spire configurations and hydrogel volumes for viability and degree of alignment. Initial choices for toroid dimensions were obtained from the positive results of Yamamoto et al. generating 12 mm outer diameter (OD) toroids gels using magnetic tissue engineering techniques [129] and the negative (unaligned) results seen in the 360 μm OD toroids of Bajaj et al [82]. From these experiments, we gather that spire dimensions provide geometric cues, that produce internal stresses, which could induce encapsulated C2C12 alignment when the OD is greater than 360 μm, but within 12 mm. We hypothesized that a toroidal shape would allow the generation of circumferential stresses [82] that would drive cell alignment and

further contractile potential. Our understanding of the term ‘geometric cues’ includes the effect of macroscopic properties such as the ratio of surface area to volume over time, gel swelling and compaction with the resultant mechanical, or Von Mises stresses, produced throughout the hydrogel-cell composite. Though encapsulated cells generate traction within a matrix, the toroidal geometry explored here should support greater circumferential, as opposed to radial, stresses, enabling tension within the construct despite the absence of externally applied tension.

Briefly, we cast hydrogels around a solid spire mold to generate toroidal constructs. We varied spire diameters of 0.5, 1.0 and 2.0 mm diameter, and initial hydrogel seeding volumes of 12.5 and 25 μL, and then determined DNA content, viability, and extent of alignment. We expected the spire sizes and gel volumes to be relevant design parameter through the modulation of stress patterns within the hydrogel with higher circumferential stress patterns inducing greater cell viability and alignment [82].

Our second goal of measuring muscle functionality was vital to the development of bio-actuators. In this portion of the study, our aim was to measure the forces generated by toroidal hydrogels containing aligned and differentiated C2C12 myoblasts. Contractibility for differentiated C2C12 myotubes subject to 4-7 days of differentiation is dependent upon the extent of functional sarcomeric muscle protein development and presence of active calcium release channels on the membranes of the sarcolemma (sarcoplasmic reticulum (SR) and transverse-tubules). Previously, we have demonstrated the presence of sarcomeric myosin in upwards of 70% of all myoblasts [6], suggesting the potential for myosin-mediated contraction.

Force production mechanisms in intact mammalian muscle is a chain of processes begun by a muscular action potential, that activates an excitation-contraction coupling causing myofibrils to contract [198]. Nicotinic acetylcholine receptors (nAChR), localized at neuro-muscular junctions, transmit signals from acetylcholine neurotransmitters to mediate the depolarization of the cell membrane and consequent calcium ion mobilization from intercellular SR stores as mediated by voltage and ryanodine-sensitive ion channels [2, 3]. An increase in cytoplasmic calcium ion concentration promotes binding to troponin C, allosterically modulating tropomyosin, which unblocks myosin binding sites for cross-bridge cycling to occur (Fig 1) as per the sliding filament theory [2, 3].

Hence, the criteria necessary to measure contractibility in C2C12-based skeletal muscle constructs are (i) availability of nAChRs, and (ii) presence of functional sarcomeric units. Expected forces for native mouse tissue and C2C12-based constructs are provided in Table 3. Although the tissue constructs are of different dimensions, forces are normalized by cross-sectional area, a plane perpendicular to the direction of force production, and entered as stress values. It must also be noted that both representative examples in Table 3 were electrically stimulated. In this work, our use of an agonist is not expected to lengthen the time to peak force due to diffusion times on the scale of nanoseconds (Appendix B.4), while still enabling toroidal hydrogels to attain peak forces on a comparable scale.

Table 3: Measured contractile forces produced by mouse extensor digitorum longus (EDL) muscle and in vitro generated C2C12 myoblast constructs. Duration of contraction includes the time taken to reach peak contraction through the time taken to return to initial steady state.

		Mouse EDL muscle [147]	C2C12 in-vitro engineered construct [128]
Twitch	**Time to peak**	50 ms	500 ms
	Duration of contraction	140 ms	250 ms
	Peak Force	200 µN	15 µN
	Stress	407 kPa	1.06 kPa
Tetanus	**Time to peak**	50 ms	500 ms
	Duration of contraction	0.2 – 6.4 sec	4 sec
	Peak Force	1.8 N	33.2 µN
	Stress	1.2 GPa	2.35 kPa

Force values provided for mouse EDL muscle are target values, though the C2C12 construct values from in vitro work are most comparable to this project, mainly due to the use of the C2C12 cell line. It must be noted that there exists a 400-fold difference in twitch stress between native mouse tissue and engineered C2C12 constructs, though the contractions occur on similar time scales.

The experimental set-up designed to measure force of a multinucleated muscular construct is dependent upon the construct size and design. For this study, construct sizes ranging in length from 200 µm to 5 mm, and width from 100 µm to 2 mm are considered, because they constitute the bulk of existing work and are comparable in size to native mouse muscle tissues. Direct measurements of force typically involve the twitch or tetanic response and isometric force generation detected using a force transducer [120, 122, 123, 127, 143, 150, 151], or a high speed camera to relate the motion of muscle constructs to the force generated [152, 153], using known mechanical properties of materials used. For instance, to measure the forces produced by miniature Bioartificial Muscles (mBAMs), Vandenburgh's group captured images monitoring the deflection of posts to which the mBAMs were anchored, at 4 frames per second (fps), to calculate the

force that would have caused the observed displacement [146]. Similarly, the contractile function of microfabricated tissue gauges (μTUGs) was determined by examining the deflection of cantilever tips on which the constructs were formed [154]. Dennis and Kosnik measured the contractile ability of 'myooids' using an in-house designed force transducer that detected changes in muscle construct length with time upon the action of external agonists [121]. Notable examples of functional skeletal muscle constructs are summarized in the table below.

Table 4: Measured forces from skeletal muscle constructs, (1^o = Primary, Ad = adult, myob = myoblasts, L = Length, W = Width, D = diameter, NR = not reported)

Construct	Construct Size	Cell Choice	Scaffold Material	Initial Cell Density	Culture duration	Maximum Stress
Excitation: Electrical Stimulation						
mBAMs [146]	L: 5mm D:1-1.5mm	1^o Ad. mouse myob	1% Collagen-I + 0.5mg/mL fibrin, hydrophobic PDMS μposts	NR	Up to 12 days	1.12 kPa (55μN tetanic)
Myooids [121]	L: 12mm D:0.1-1mm	1^o Ad. rat myob	Fibrin, laminin, buckled PDMS pattern for alignment	NR	12 days	4.63 kPa (440 μN tetanic)
Magnetic TE-based rings [128, 129]	Toroidal Shape D: 150μm	C2C12	Collagen-I + Gelatin	1.0×10^6	Up to 17 days	2.35 kPa (33.2μN twitch)

Alternatively, indirect measurements include the use of lentiviral transduction with an intracellular sensor for calcium ion flux that is attributed as proportional to functional muscle activity [123], and tracking the movement of secondary objects of estimated mechanical properties due to the supposed action of the primary muscular construct. Ideally, direct force measurements would be made with a force transducer in response to biochemical agonists or electric pulse stimulation.

Activating agents for the controlled contraction of myoblasts range from custom-made solutions with high calcium ion or ATP content [155] in physiological solutions such as

Tyrode's, Ringer's, Dulbecco's or Normal External Solution (NES); to small molecules such as caffeine and acetylcholine (ACh) [43]; to the use of parallel platinum wire electrodes for electrical stimulation [121]. Myosin inhibitors used to block force production without altering depolarization or calcium release include blebbistatin [158], N-benzyl-p-toluene sulphonamide (BTS) and 2,3-butanedione monoxime (BDM) [159]. Specific ACh inhibitors that block neuromuscular excitation include pancuronium bromide and tubocurarine chloride [160]. A hallmark of sarcomeric contraction is reversibility of the force production, once the stimulation is removed, to restore membrane potential and seize force production.

In this study, we used a custom-made measurement device to measure contraction produced by external agonists, ACh and caffeine, using the previously described toroidal gels. In this aim, we used the C2C12 skeletal muscle progenitor cell line, encapsulated in biofunctional hydrogels cast with a spire mold to generate a toroidal shaped gel configuration for circumferential alignment, and hooked the resulting 3D swollen hydrogels on the custom built setup. We hypothesized that the use of agonists will prompt sarcomeric contraction in the 1-4 kPa stress range, and removal of the contractile agents will cease force production. The goal of this research was to determine the functional output of the cell–hydrogel composite hydrogels and also develop a custom contraction measurement apparatus that could be used for other tissues generating forces in the same scale.

Materials and Methods

Spire Mold Production

Aluminum negative molds (Figure 12) were designed in AutoCAD and milled using a CNC Lathe (Biomedical Engineering student machine shop, Georgia Institute of Technology, Atlanta, USA). Negative molds were sonicated with 100% ethanol to clean before pouring 10:1 ratio of SYLGARD® 184 elastomer to curing agent (Sigma Aldrich, MO, USA). Negative molds with PDMS were placed under vacuum for a minimum of 2 hours to release air bubbles trapped in spires. PDMS was cured at 70^0C for 3 hours or overnight and peeled off gently. The first two PDMS casts from aluminum were discarded due to the presence of metal dust adhered to its surface. Acceptable PDMS casts were cut to separate individual spire-reservoirs, and placed in glass dishes for overnight silanization. Samples were autoclaved the next day and ready to use for cell culture immediately.

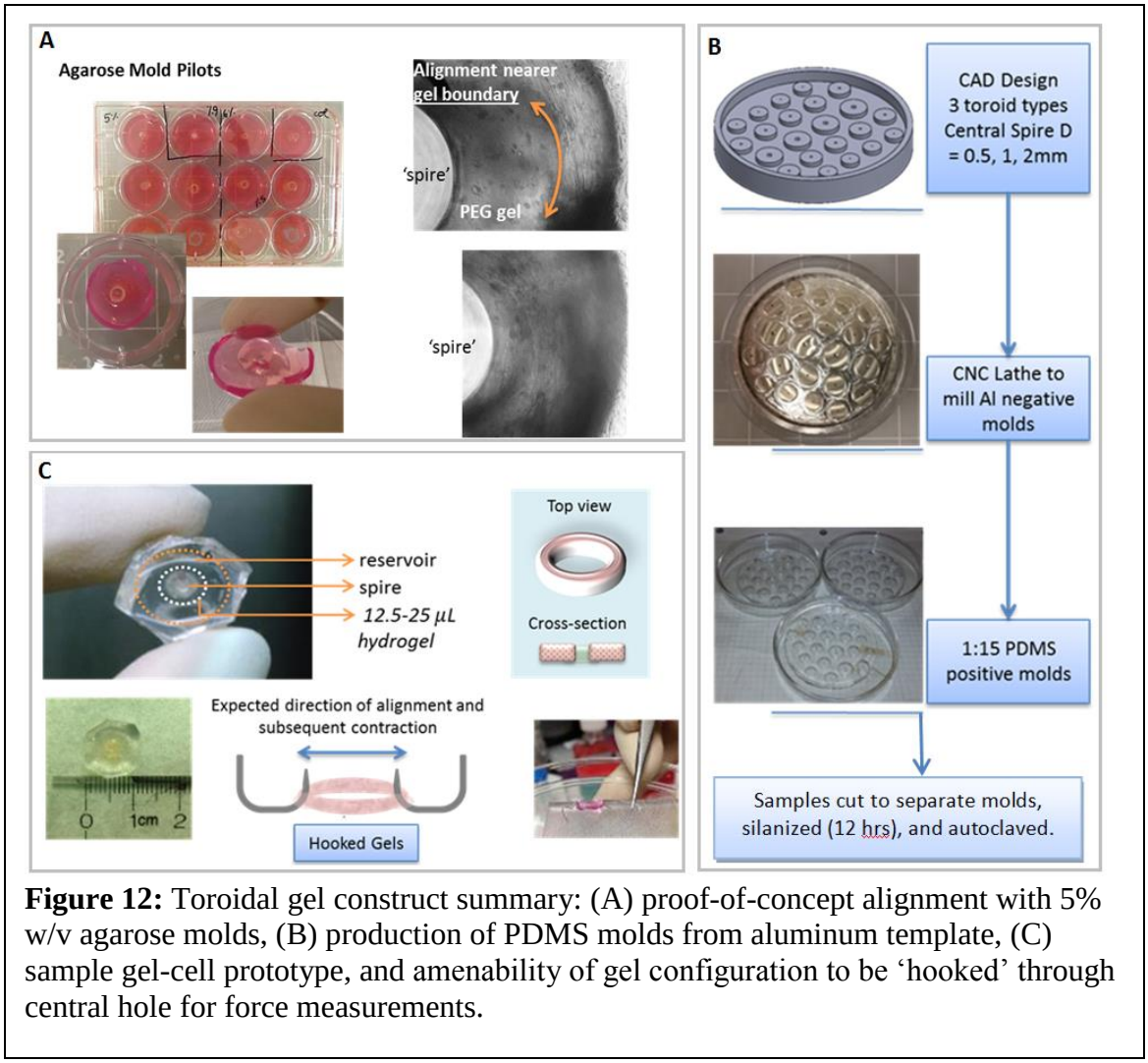

Figure 12: Toroidal gel construct summary: (A) proof-of-concept alignment with 5% w/v agarose molds, (B) production of PDMS molds from aluminum template, (C) sample gel-cell prototype, and amenability of gel configuration to be 'hooked' through central hole for force measurements.

Table 5: Final mold dimensions where spire diameter, height and reservoir diameter as per milled aluminum mold and subsequent PDMS dimensions

Spire Diameter (mm)	Spire Height (mm)	Reservoir Diameter (mm)
0.5	8.0	8.0
1.0	10.0	9.0
2.0	5.0	11.0

Cell Culture and Hydrogel Casting

Skeletal murine myoblasts C2C12 cells were obtained from ATCC (Manassas, VA, USA). Dulbecco's modified Eagle's medium [DMEM; 4.5 g/l D-glucose, L-glutamine (+), sodium pyruvate (–)], insulin–transferrin–selenium (ITS-X), Dulbecco's phosphate-

buffered saline (PBS), penicillin/streptomycin, trypsin/EDTA and fetal bovine serum (FBS) were obtained from Life Technologies (Carlsbad, CA, USA). Horse serum was supplied by Hyclone (Logan, UT, USA). Cells were cultured in 20% FBS and 1% penicillin/streptomycin in DMEM (growth medium, GM) until passage 4, prior to hydrogel encapsulation, and further growth and differentiation in 2–10% horse serum (HS), 1% ITS-X and 1% penicillin/streptomycin in DMEM (differentiation medium, DM).

C2C12 cells were encapsulated in either collagen type I (3 mg/ml; BD Biosciences, San Jose, CA, USA) gels or protease-degradable PEG-based hydrogels, prepared as previously described [12]. PEG–maleimide (PEG–MAL) four-arm macromers (20 kDa, > 95% maleimide functionalization; Laysan Bio, Arab, AL, USA) and custom-synthesized peptides (AAPPTec, Louisville, KY, USA) were used. PEG–MAL macromers were prefunctionalized with GRGDSPC (RGD) adhesion peptide in 2.0 mM triethanolamine (TEA) solution for 30 min. PEG polymer density was maintained at 5% w/v, and RGD density was maintained at 2.0 mM. The precursor molecules and cell suspension solution (for a final concentration of 8×10^6 cells/mL) were crosslinked into a 25 μL or 12.5 μL hydrogel by the addition of a cysteine-flanked protease-degradable peptide sequence, GCRDVPMSMRGGDRCG (VPM), for 15 min. The concentration of crosslinker peptide was proportional to the macromer concentration in order to react with the appropriate number of maleimide groups in the macromer and generate a fully crosslinked hydrogel network. The hydrogels were left to swell in growth medium overnight, and the medium was changed daily. Hydrogels were cultured for 3 days in growth medium and 7-11 days in differentiation medium, dependent upon the assay. The resulting hydrogel phase is

transparent, which allows visualization of cellular activity without disruption of the cellular microenvironment.

As geometrical controls, hydrogels were also cast on Parafilm and placed into wells as free-floating gels, hereon referred to as ‘free’ hydrogels and control without spires. ‘Linear’ hydrogels were cast in 4 or 8 welled chambered coverglass and used as geometric controls.

To generate cell-laden hydrogels, four-arm PEG–MAL macromers were functionalized with RGD and cells, followed by crosslinker, and immediately cast around spires (Figure 13). Preliminary data (Figure 12A) shows toroidal gels cast on agarose

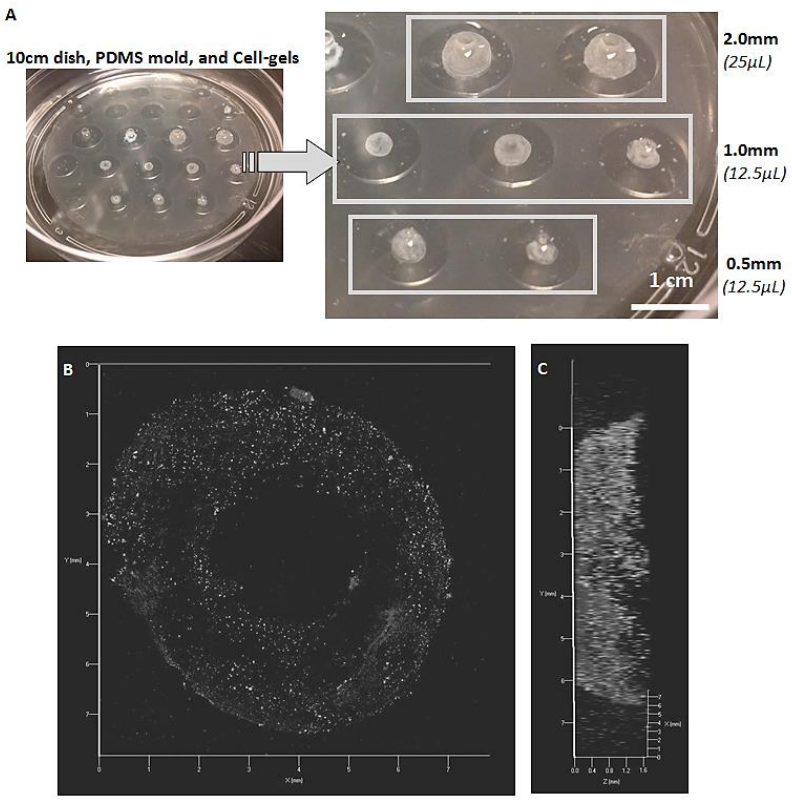

Figure 13: (A) Macroscopic image showing PEG-4MAL gels cast in silanized PDMS spire-molds, prior to separation and swelling in growth media. Cloudy appearance of gels is due to high cell seeding density of 8×10^6 cells/mL. (B&C) 3D confocal reconstruction of cell-encapsulated 2.0 mm spire-toroid on day 3 from a top-down and side-view, where C2C12 cells are fluorescent.

molds generate circumferentially aligned cells distributed evenly through the hydrogel as viewed by light microscope. Aluminum negative molds (Figure 12B) were milled with three different spire configurations to study the effect of different spire geometries on encapsulated cell alignment. PDMS molds were cast off the aluminum surface generating spires that gels could be cast around (Figure 12C, Figure 6). Spire configurations are henceforth referred to using the diameter of the central cylinder, or spire: 0.5 mm, 1.0 mm and 2.0 mm spires. The hydrogels cast from around these spires are referred to using the spire dimension, and the term 'toroidal hydrogels', for example: 2.0 mm spire-toroidal hydrogel.

Measuring Hydrogel Surface Area and Volume

Hydrogels cast and swollen in growth media for at least 24 hours were imaged with engineering paper for scale using a digital camera. A sterile microcapillary pipette tip was graduated with a scale and slid vertically along the spire to determine gel height. Dimensions were measured as per the requirement of equations below and Figure 14, to be able to solve for volume and surface area of the hydrogels.

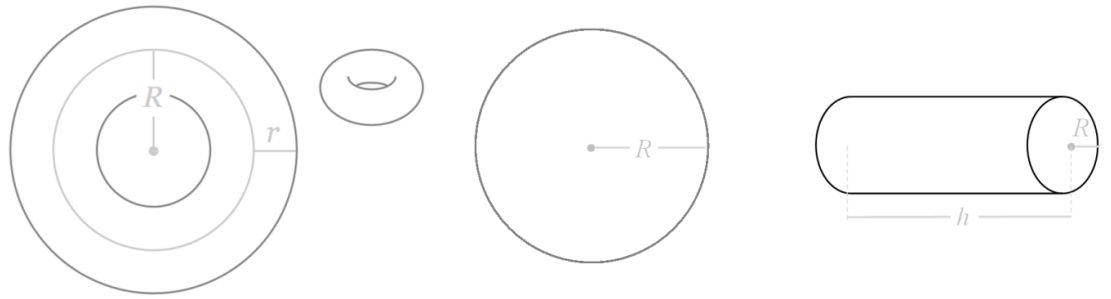

Figure 14: Dimensions used to estimate surface area and volumes of different gel configurations, A. Torus shape, B. Sphere, C. Cylinder. Equations used as described in text.

Toroidal hydrogels, using torus formulae:$Volume\ (torus) = (\pi r^2)(2\pi R)$; $Surface\ Area\ (torus) = (2\pi r)(2\pi R)$. Free Floating hydrogels, using sphere formulae: $(sphere) = \frac{4}{3}\pi R^3$; $Surface\ Area\ (sphere) = 4\pi R^2$. Linear hydrogels, using cylinder formulae:$Volume\ (cylinder) = \pi R^2 h$; $Surface\ Area\ (cylinder) = 2\pi Rh + 2\pi R^2$.

Cross-sectional data of the toroid is shown in Figure 13.

DNA Content Analysis

Gels were gently placed in microcentrifuge tubes containing 50 µL of 1 mg/mL collagenase-type I (Worthington Biochemical Corporation, Lakewood, NJ, USA), and incubated for 1 hour at 37^{o}C to degrade completely. Whole cell lysate was extracted using Tris-HCL buffer and probe sonication. DNA content was assayed as per the instructions of the CyQUANT® Cell Proliferation Assay Kit (Life Technologies, Carlsbad, CA, USA). Plates containing samples along with collagenase and Tris buffer blanks were read at 480/520 with HTS 70000 Plate Reader.

Live/dead and immunofluorescence staining and image analysis

Hydrogels containing encapsulated cells to be analyzed for cellular viability were incubated in PBS for 10 min to remove serum. Hydrogels removed from media and placed in PBS were observably different in color (between pink and orange) compared to the surrounding clear PBS solution. Hydrogels appeared translucent but colorless due to the diffusion of media out of the gel within 5 minutes, and an additional 5 minutes was provided to ensure more complete serum removal by diffusion. Next, the hydrogels were stained with the Live/Dead stains Calcein-AM (2 μM) and TOTO-3 iodide (2 μM) (Life Technologies, Carlsbad, CA, USA) for 10 min. Samples stained for sarcomeric myosin as a marker of muscle differentiation, and actin for alignment studies, were fixed in 4% methanol-free paraformaldehyde for 30 min at room temperature, permeabilized and blocked with 0.5% Triton X-100 in 1% bovine serum albumin (BSA; Sigma-Aldrich, St. Louis, MO, USA) before being incubated with primary antibody. Monoclonal antibodies against sarcomeric myosin (MF20, 1:200, 3 μg/mL) and actin (Alexa Fluor Phalloidin 555, 1 μM) were obtained from the Developmental Studies Hybridoma Bank (Iowa City, IA, USA) and Life Technologies (Carlsbad, CA, USA) respectively. Secondary antibody AlexaFluor 488-conjugated anti-rabbit IgG and DAPI were obtained from Life Technologies (Carlsbad, CA, USA). Gels were incubated in antibody solutions (10 μg/mL and 1 μg/mL for secondary antibody and DAPI, respectively) overnight at room temperature and rinsed thoroughly between all steps in PBS containing 0.05% Triton X-100 and 1% BSA. The hydrogels were transferred into fresh PBS solution and imaged in Lab-Tek chamber slides, using a Nikon-C2 laser scanning confocal microscope with a 20X air objective, (0.75 NA). Live/dead images were taken in LiveCell System

(Pathology Devices, Westminster, MD, USA). All images were taken at the same settings and subjected to consistent threshold values during image processing. Z-stack projections through 100–300 μm thick sections of the hydrogels were rendered. Individual slices/image were analyzed using customized macros on ImageJ software (NIH, Bethesda, MD, USA), and projected into maximum-intensity images for the purposes of illustration. For samples stained for live/dead, the fractional viability was calculated as the number of live cells/total cells. The number of cells stained positively for Calcein (live only) was divided by the number of cells stained positive for TOTO-3 iodide (dead only) plus the number of Calcein-positive cells. Projected spread area was determined as the total area occupied by Calcein stain. For samples stained for sarcomeric myosin and DAPI, percentage differentiation was calculated as the number of cells stained positive for myosin over the total number of cells/imaged plane. Number of multinucleated cells and number of nuclei/differentiated cell were determined using binary layers, applied with Nikon Instruments Software (NIS)-Elements. Image slices were chosen from stacks at 10 μm (*z* axis) intervals, to avoid counting the same cells more than once using ImageJ and NIS-Elements. For multi-nucleation analysis, the NIS-Elements software was used to distinguish between DAPI and sarcomeric myosin by application of layers to individual image slices. In very few instances, images were discarded because multinucleated cells were found in close proximity to each other, resulting in poor discrimination by the program.

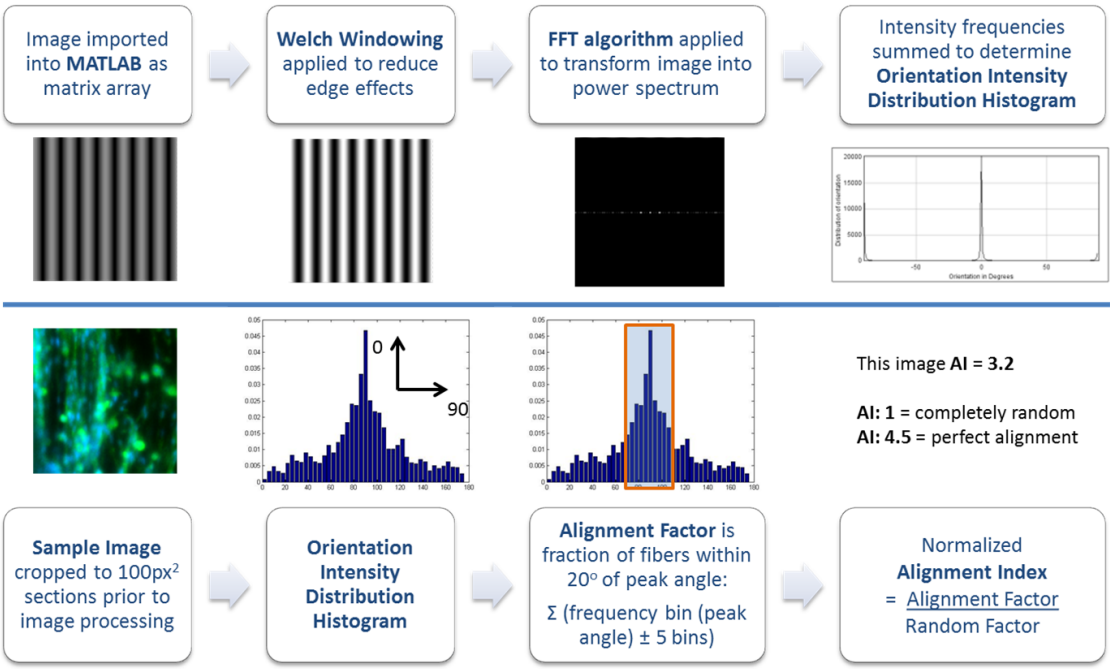

Figure 15: Flowchart to determine extent of local alignment through the calculation of an Alignment Index (AI) by image analysis.

Image Analysis for Alignment Index

As outlined in Figure 15, Images were cropped into 100 squared pixels quadrants, imported to MATLAB, windowed, filtered, and binned into orientation histograms. The peak angle was detected, as measured by aligned pixels, and the fraction of fibers within a 20 degree range was included in the Alignment Factor determination. After normalizing to random data, the Alignment Index was obtained and imported into Microsoft Excel for the completion of analysis [199, 200].

Force measurement setup

The overall force measurement setup is shown in Figure 16, and features three main components: the force transducer setup (Figure 16A), bread boarded circuit to provide power to the force transducer and amplify the signal generated (Figure 16B), and the personal computer (PC) to record and analyze signals (Figure 16C). The force transducer used was the Kronex AE 801 Multipurpose Sensor Element (Kronex, Oakland, California, USA), a strain gauge sensor, hereon referred to as 'sensor'.

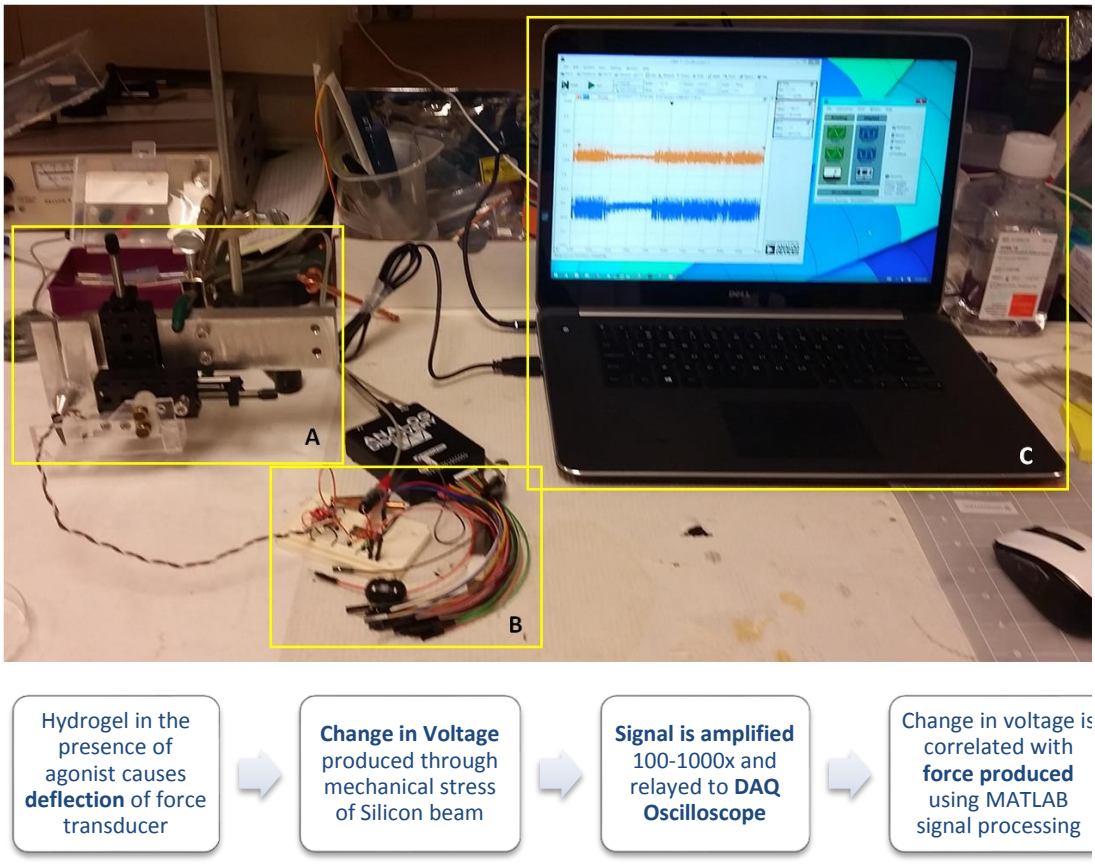

Figure 16: The overall force measurement setup: (A) the transducer setup, (B) circuit and DAQ, (C) PC with waveform software and further MATLAB analysis.

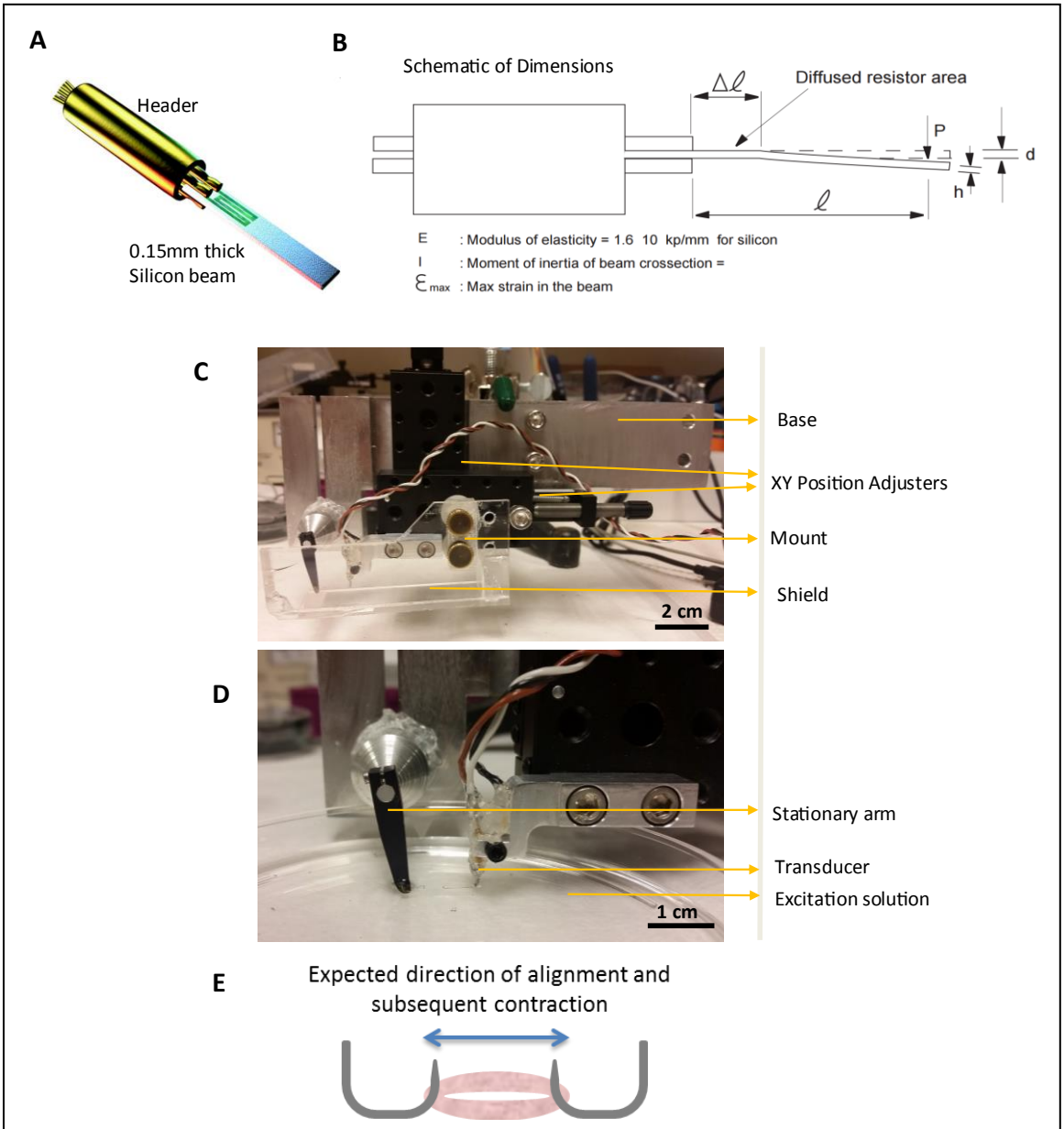

Figure 17: (A) Photo of the sensor element from Kronex. (B) Schematic of sensor dimensions. (C) Measurement setup featuring sensor mounted on base and protected by a clear shield. (D) Close-up of the sensor with attached hook, stationary arm, and immersed in solution. (E) Schematic representation of loading the hydrogels, where toroids are placed on the hooks using the central hole.

The approximate ranges for force measurements reported in the literature for comparable scales of muscle constructs range from 3.8 μN/mm^2 [144] to 2.3 mN/mm^2 [123] for absolute values ranging from 6 μN to 28 mN. An analog force transducer to

make these measurements needed to support at least 28 mN forces and have the sensitivity to detect changes in the μN scale. We chose the Kronex AE 801 Sensor, a silicon strain gauge, for its 120 mN upper limit and high sensitivity.

When the tip of the silicon beam is deflected due to force, the areas where the resistors are located experience mechanical stress. Due to the piezoresistive effect in silicon, these resistors change value, modulating the output voltage of the sensor. The output voltage, as a function of change in resistance, is also determined by extent of deflection and other beam dimensions, in a linear fashion, shown in Equation 1, with further dimensions as described in Figure 17.

$$\boldsymbol{\Delta V} = 0.75 * V * \lambda * \frac{l - \Delta l(0.5)}{l} * \frac{h}{l^2} * \boldsymbol{d}$$

$$d = \frac{\boldsymbol{P}}{E * I} * \frac{l^3}{3}$$

$$\boldsymbol{P} = \frac{4\,E\,I}{V\,\lambda\,h\,(l - \frac{\Delta l}{2})} * \Delta V = C_1 * \Delta V$$

Equation 1: Relationship between change in voltage (ΔV), and force of deflection (P). Also involved are: the gauge factor of the resistors (λ), length of the beam (l), thickness of the beam (h), deflection (d), modulus of elasticity for silicon (E), and moment of inertia of the beam cross-section (I). All these values are either provided by the manufacturer (Figure 17B), or easily calculated from the provided values. The sensor was calibrated using a 40mg weight on the horizontal beam surface to check the theoretical conversion rate and add a constant coefficient or 'correction factor' when converting from voltage change to force experienced

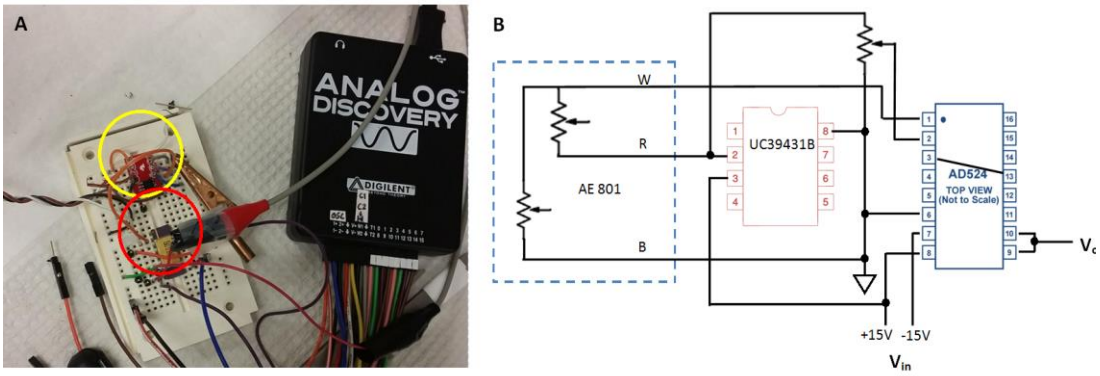

Figure 18: Bread board and corresponding circuit diagram

The bread boarded circuit (Figure 18) featured a Precision Adjustable Shunt Regulator (voltage regulator), Catalog # UC39431B, (Texas Instruments, Dallas, USA) to supply a regulated 5V input voltage to the sensor; and a Precision Instrumentation Amplifier (Product # AD 524, Analog Devices, MA, USA) to amplify the output voltage one of three ways: by 10,100, or 1000 times. Here, the 1000 level gain was employed. The power supply used was Elenco Precision Deluxe Regulated Power Supply (Specs: 0-20 Volts, 3Amps or 0-40 volts, 1.5Amps), used for this purpose at: 15V, 1.5A.

The WaveForms program (Digilent Inc., Pullman, WA, USA) was used to interface with the Analog Discovery DAQ (Digilent Inc., Pullman, WA, USA), which also functioned as an oscilloscope and voltmeter.

The sampling frequency, as the default of the DAQ is 100 MHz, and the cutoff frequency used was 60 kHz. A Savitzky-Golay filter, which functions as a moving average filter, was applied to all signals using MATLAB, with polynomial of order 2 and frame size of 199. This acted as a low pass filter and cleared the signal for peak detection. Peak force produced was translated to total force produced as observed within a 30 second acquisition window. The values used for the filter application were chosen based

upon the fast Fourier transform (FFT) and spectrogram analysis of output voltage readings.

A hook fashioned out of wire was attached to the silicon beam as a means of holding on to the hydrogels during testing. The entire sensor element was protected from short-circuiting by coating conductive portions in small amounts of transparent cyanoacrylate gel (Figure 17C&D). The cyanoacrylate gel does not coat the silicon beam on the force transducer and does not change its stiffness. The opposing hook was attached to a stationary arm. For future studies, this portion can link to an external motor for finely controlled mechanical stimulation or isometric contraction studies [155]. The Analog Discovery DAQ recorded voltage over time from the strain gauge sensor. Readings were converted to text files that could be imported and analyzed in MATLAB.

Contractility Studies

Contractility experiments were conducted on day 12 of construct culture (3 days in GM, 9 days in DM). Hydrogel volumes of 25 µL were used as 12.5 µL were unable to be handled consistently. The experimental design is detailed in the table below, where contractile agonists refer to ACh (100 µM) or caffeine (50 mM) and the myosin inhibitor, blebbistatin (100 µM). All solutions were warmed to 37^{o}C prior to use, as this was deemed necessary for caffeine-mediated cellular activation [4]. Constructs were removed from spire-molds and mounted in measurement setup with PBS solution for up to 5 minutes to stabilize. Tension upon mounting was maintained consistent to tension of fabricated hydrogel by using the toroidal hydrogel outer diameter on the mold prior to mounting as the starting length. For 2.0, 1.0 and 0.5 mm spire-toroids these lengths were

5.0 mm, 4.5 mm and 3.0 mm respectively. Voltage signal was monitored visually during this time. Constructs remained on the setup, attached to hooks, for remaining solution changes. Signal was recorded from time of solution 1 exchange with solution 2, and solution 3, where relevant, or returned to solution 1. Five or more samples were used for each condition ($n \geq 5$).

Table 6: Experimental design setup for contractility studies (PBS is with calcium and magnesium, Blebb = Blebbistatin).

	Hydrogel Geometry	Solution 1 (5 min)	Solution 2 (1 min)	Solution 3 (1 min)	Purpose
1	Toroidal (Aligned) hydrogels	PBS	PBS		Baseline
2		PBS	Agonist		Contraction assessment
3		PBS	Blebb		Myosin inhibition check
4		PBS	Agonist	PBS	Reversibility check
5		PBS	PBS	PBS	Reversibility (Negative) control
6		PBS	Agonist	Blebb	Myosin dependence assessment
7		PBS	Blebb	Agonist	Myosin dependence assessment
8	Free-Floating, bulk gels	PBS	PBS		Geometric control baseline
9		PBS	Agonist		Geometric control
10		PBS	Blebb		Myosin inhibition check
11		PBS	PBS		Cell-free control baseline
12	Cell-free, torus gels	PBS	Agonist		Cell-free control
13		PBS	Blebb		Myosin inhibition check

Statistics

Data are expressed as mean ± standard error of the mean (SEM). Statistical analysis was performed using *t*-test for comparison of two different groups, one-way ANOVA for comparisons among different groups, and two-way ANOVA for comparisons between different groups at different time points, using GraphPad Prism software. Significance was set at $p < 0.05$.

Results

Characterization of Different Gel Configurations by Surface Area to Volume ratios

Different gel volumes were utilized in the generation of toroidal hydrogels as they were found to degrade within 3-6 days when cast with a volume below 10 µL, while alignment was not observed until day 7 with gel volumes greater than 40 µL. To examine this phenomenon, swollen hydrogel dimension (day 1) measurements were used to calculate empirical volume and surface areas for 12.5 µL and 25 µL hydrogels (Table 7). For controls, we also cast free-floating and linear hydrogels.

Significant differences in empirical volume were observed between controls (linear and free) and the 2.0 mm spire-toroids, with the toroidal gels exhibiting higher post-swelling volume, for both volume conditions (12.5 µL and 25 µL). The volume difference between original casting and post-swelling hydrogels may arise due to the different physical hydrogel configurations. Hydrogel swelling is a function of several factors: physical properties of the hydrogel itself as well as those modulated due to cellular behavior. The effect of physical geometry, or volume, reflects an association between osmotic pressure and tension generated within the gel matrix. As described previously, even 1 polymer w/v % change resulted in a 20% shift in cell viability, so it is likely that the converse, a change in cell behavior experienced due to differential stresses in varying geometries would affect the extent of hydrogel swelling or compaction [6]. Secondarily, the hydrogel macrostructure may impact cellular behaviors such as contractility, further changing the final volume, though these effects should be minimal at such a short time after gel casting. For surface area, differences were observed for free,

1.0, 2.0 mm spire-toroidal gels compared to linear gel configurations of 12.5 µL. For 25 µL hydrogel volumes all gel configurations were different to linear hydrogels.

Surface area and volume were lowest for the linear hydrogels, yet the ratio of surface area to volume was the highest for this hydrogel configuration. We have further observed that linear gels cannot withstand more than 3 days in culture, quickly degrading and leaving cells on the 2D dish rather than encapsulated in a 3D hydrogel. The configuration with the second highest surface area to volume ratio is 0.5 mm spires. These toroids were found to be difficult to handle by day 7, in comparison to 1.0 mm and 2.0 mm spire-toroids, but did not degrade to the extent of gel loss as in the case of linear gels. This suggests a potential correlation with the surface area to volume ratio and longevity of the hydrogel configuration. Tractability issues of this extent were not encountered by 1.0, 2.0 mm spire-toroids.

Overall, surface area to volume ratios are consistently highest for 0.5mm and linear hydrogels, while 1.0mm, 2.0mm spires and free floating hydrogels were calculated to have the lowest ratios.

Table 7: Dimensional characterization of PEG-4MAL hydrogel configurations. Day 1, after complete swelling in growth media. Dimensions measured from macroscopic hydrogel images taken on squared graph paper (n=6), during media exchange. Two hydrogel volumes examined: 12.5 µL and 25 µL, in 3 spire configurations with free-floating and linear geometric control.

For the empirical volume data: * indicates significant differences between the empirical volume of 12.5 µL of free and linear hydrogels compared to 2.0 mm spire-toroidal gels. # indicates significant differences between the empirical volume of 25 µL of 1.0, 2.0 mm spires and free hydrogels compared to 0.5 mm spires. ## Indicates significant differences between the empirical volume of 25 µL of free and linear hydrogels compared to 2.0mm spires

For the surface area data: ** indicates significant differences between the surface area of 12.5 µL of free, 1.0, 2.0 mm spire-toroidal hydrogels compared to linear gels. *** indicates significant differences between the surface area of 12.5 µL of 0.5 mm spires and 2.0 mm spires. $ indicates significant differences between the surface area of 25 µL of free, 0.5, 1.0, 2.0 mm spire-toroidal hydrogels compared to linear hydrogels, that is,

the surface area of linear gels is significantly different from all other configurations. [$$] indicates significant differences between the surface area of 25 µL of 0.5 mm spire-toroidal gels and 2.0 mm spire-toroidal gels (all $p<0.05$).

Cast Hydrogel Volume	Configuration	Surface Area (mm2)	Empirical Volume (µL)	Ratio of SA:V
12.5 µL	0.5 S	62.7±11.4 ***	25.3±9.5 *	2.48
	1.0 S	100.8±17.1 **	52.0±11.9	1.94
	2.0 S	131.3±35.8 **, ***	72.3±17.1	1.82
	Free-floating	111.8±6.4 **	55.6±4.84	2.00
	Linear	44.2±17.9	17.3±9.8 *	2.54
25 µL	0.5 S	144.3±26.2 $$	58.7±12.3	2.46
	1.0 S	192.8±23.6	138.8±34.2 #, ##	1.39
	2.0 S	197.3±35.2	126.8±22.9 #, ##	1.57
	Free Floating	179.5±26.4	118.0±61.9 #, ##	1.52
	Linear	83.7±17.2 $	34.4±12.4	2.43

Optimization of Spire-Toroid Hydrogels with 12.5µL and 25µL Volumes

To examine the impact of different hydrogel volumes and spire configurations on proliferation and viability over time, we analyzed DNA content (Figure 19) and percentage of live cells over a period of 14 days (Figure 20). The two volume configurations tested could be expected to produce differences in cell behavior, a consequence of the material swelling (due to high affinity of the PEG chain for water and resisted by crosslinks) which is affected by the configuration, cell-mediated proteolysis of the gel (increase swelling), and cell contractility. We have previously asserted that a highly viable cell population, at a reasonable cell density, is a pre-requisite to efficient differentiation, and in this case, alignment of C2C12 cells.

DNA content increased over time, most notably for the spire configurations (Figure 19A) compared to free floating and linear gel controls. The trend of relative increases in

DNA content was seen for both gel volumes. Absolute differences between 12.5 µL and 25 µL were expected due to differences in volume with a consistent seeding density of 8×10^6 cells/mL. There were significant differences between DNA content at day 14 and/or day 7 for all the spire-toroid hydrogel configurations compared to day 3 for both volumes of hydrogel used. Changes in DNA content from days 0 to 3 were not significant in any case, as were the changes between days 0 to 14 for free hydrogels and days 0 to 3 for linear. Linear hydrogels were completely degraded or not workable by days 7 and 14, as indicated by unavailable data (#) on graphs. Specifically, 12.5 µL hydrogels cast as spire-toroid hydrogels supported 0.5 –1.8 µg DNA per hydrogel (from here on: µg/gel) for days 1 and 3. After day 7 there was a significant, up to twofold increase in DNA content not exceeding 4 µg/gel. A similar trend of increasing DNA content was seen in 25 µL spire-toroid hydrogels, with initial DNA content ranging from 1.5 – 2 µg/gel and final concentration as high as 7 µg/gel (Figure 19A-C). DNA content remained steady in the free floating hydrogels between 0.5 – 1.8 µg/gel for 12.5 µL volumes and 1.8 – 4 µg/gel for the 25 µL volume (Figure 19D). Linear hydrogels supported DNA content until day 3 in the ranges of 0.4 – 1.7 µg/gel for 12.5 µL volumes, and 1.8 – 4.0 µg/gel for 25 µL volumes, before degrading (Figure 19E). Given the only source of DNA were the encapsulated C2C12 cells, knowing that the majority of cells stayed encapsulated and could not exit the gel easily, and finally, knowing that no cells are being added to the gel, we can attribute any changes in DNA content to encapsulated cells only. Increases in DNA content over time for the spire-toroid configurations suggest the occurrence of cell proliferation. Meanwhile, the maintenance of DNA levels over time, as seen in linear and free hydrogels, suggest a lower level of cell proliferation, if at all. These differences in

cellular behavior could be explained by the concept of different stresses experienced by encapsulated cells in varying geometries.

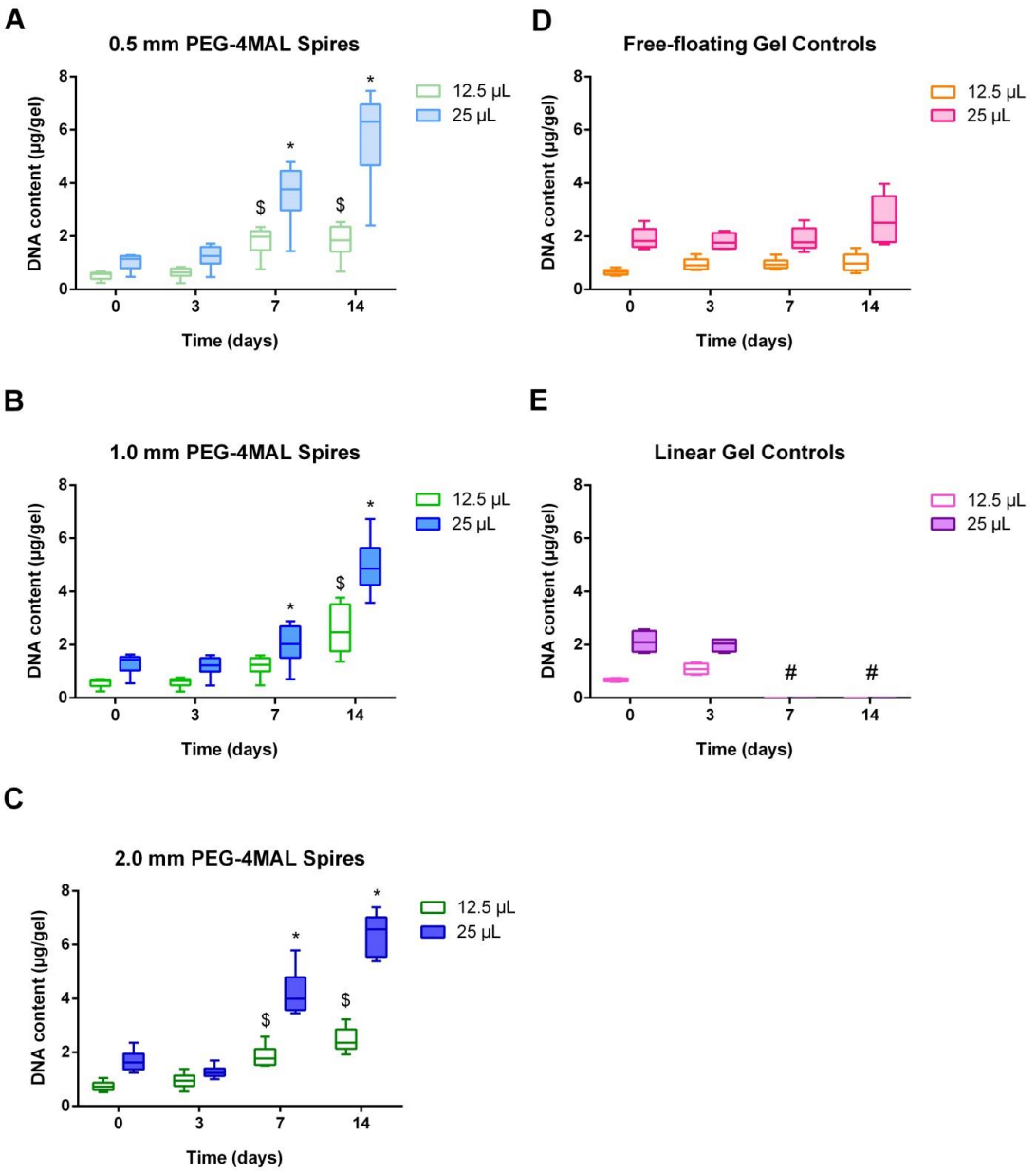

Figure 19: DNA content over time: quantification of comparison between 2.0 mm, 1.0 mm, and 0.5 mm spire-toroid configurations with 12.5 µL and 25 µL gel volumes (A-C) different spire configurations, (D) free hydrogels, (E) and linear controls. '#' indicates no data available due to gel degradation. ($n \geq 6$). '*' for 25 µL, '$' for 12.5 µL indicates significance between day 14 and/or day 7 for spire-toroids compared to day 3 and day 0. Change from days 0 to 3 was not significant for all conditions. No significant change between days 0 to 14 for free gels and days 0 to 3 for linear, all $p < 0.05$. Boxes extend from 25th to 75th percentiles of data; whiskers extend from minimum to maximum data values.

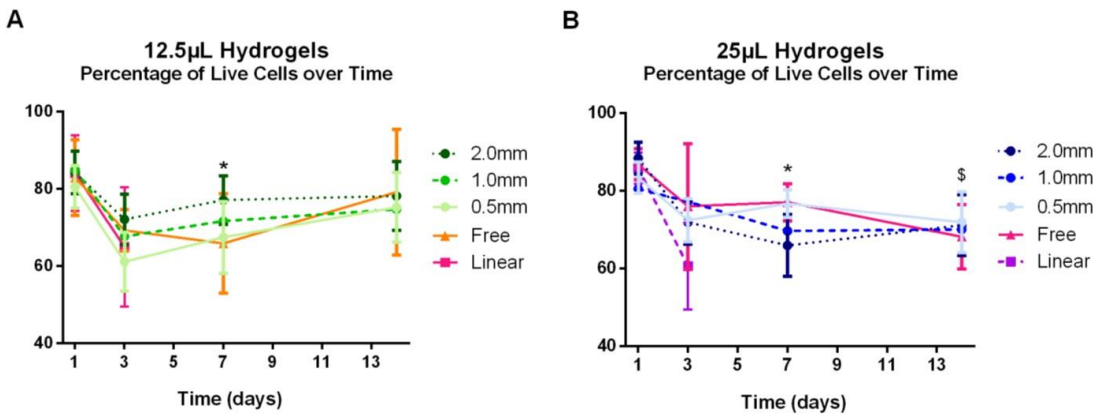

Figure 20: Percentage of live cells over time: quantification of comparison between 2.0 mm, 1.0 mm, and 0.5 mm spire-toroids, free, and linear hydrogel configurations with 12.5 µL (A) and 25 µL (B) hydrogel volumes ($n \geq 6$). '*' indicates significant differences exist between all groups at day 7 compared to day 1, for both volume conditions. '$' indicates significant differences between all configurations at day 14 compared to day 1 for 25 µL volume hydrogels only. No significant differences between configurations at any given time point for a consistent gel volume

The next metric studied was percentage of live cells: the proportion of cells stained for Calcein, as live cells, compared to total number of cells (Calcein-positive + TOTO-3 iodide-positive). As Figure 20 shows, the percentage of live cells stayed constant (majority between 60 – 80%) over time with a small drop at day 3, as previously observed [6]. Consistent with DNA content trends, there were significant differences between the percentage of live cells at day 7 for all the spire-toroid configurations, free and linear hydrogels compared to day 1, for both volume conditions. At day 14, significant differences existed between all configurations of 25 µL volume hydrogels only compared to day 1 (Figure 20B). There were no differences between configurations at any given time point for the same gel volume. The lack of significant differences between the 12.5 µL gels at day 14 compared to day 7 suggest that the viability is better supported in the hydrogel of smaller volume. This difference between the two hydrogel

volumes at day 14 may exist due to smaller diffusion distances for mass transport in 12.5 µL hydrogels compared to 25 µL. There were an overall higher number of cells in 25 µL hydrogels as all gels were seeded with the same cell density at day 0 but with different volumes. Hence, the larger gels supported a higher absolute value of live cells at day 14 (quantitatively, the number of live cells in 25 µL hydrogels was 1.5-2-fold higher than 12.5µL gels at all time points). Additionally, a higher number of cells in the 25 µL hydrogel likely increased nutrient demand, which was limited by diffusion, further contributing to the lower reported percentage viability.

Taken together, the data for DNA content and percent live cells suggests that immediately post-casting, cells encapsulated in hydrogels were at a higher proportion of live to dead (between 70-90%). From day 1 to day 3 the percent live cells dropped though DNA content was maintained. This suggests that although the number of dead cells increased, a relatively constant DNA profile indicated that the total number of cells was constant. The live cells that survived day 3 proliferated from day 3 to 7 to significantly increase DNA content. This trend then continued with proliferating cells increasing the DNA content by day 14 while percent live cells was maintained at a constant, high level (between 60-80%). Differences are most notable over time for individual hydrogel configurations, although not explicit between them for the same time point. This lack of variation among hydrogel geometries suggests that the optimized polymer hydrogel utilized supports cell viability, regardless of hydrogel volumes and configuration. Yet it appears that additional factors are involved in increasing the cell count over time in the toroidal gels. This may be explained by the existence of varying stress distributions between bulk, linear, and toroidal hydrogels that modulate cell proliferation and

alignment behavior, but do not impact survival.

Differences in Alignment Extent between Hydrogel Volumes and Spire Configurations

We observed that the extent of alignment varied with spire configuration and gel volume. To quantify, we utilized the metric "Alignment Index" (AI) to describe the extent of cellular alignment (Materials and Methods, Figure 15). Completely random structures produce an AI of 1.0, while perfect alignment produces an AI of 4.5. This scale is adapted from Swartz et al.[199], where 2D collagen matrices were used for fibroblast alignment. AI ranges from 1.5 to 2.5 were reported in Swartz's work. Using this method of image processing and analysis, we report indices ranging from 1.0 (random) to 3.0 (max value is 4.5 for perfectly aligned). For the spire configurations, alignment extent increased from day 1 to day 14, with the highest alignment indices were measured in days 7 and 14. For 1.0 mm and 0.5 mm spire-toroid configurations, (Figure 21B&C) with 12.5μL gel volume, there was a significant difference between days 1 or 3 compared to days 7 and 14. There were no significant differences for the 2.0 mm spire-toroids between days 7 and 14 for the different volumes (Figure 21A), though a significant increase from day 1 to day 7 was observed. The AI measured from free gels did not exhibit significant differences, for either volume tested, between days 1, 3, 7, or 14 (Figure 21D). Additionally, 0.5 mm spire-toroids showed significant differences between the two different gel volumes, at days 7 and 14. All spire configurations produced significantly more locally aligned cells compared to free gel controls. Day 14 summary graphs (Figure 21E&F) show 1.0 mm spire-toroid of 25 μL gel volume were found to have a significantly higher AI than other groups, while 12.5 μL (Figure 21F) free gels exhibited the lowest AI, significantly lower than the three spire-toroid configurations

($p<0.05$). The interesting outcome to be noted here is that 1.0 mm spire-toroids result in the highest extent of alignment, unaffected by seeding volume. From our data it appears that hydrogel geometry influences alignment and that alignment increases with time until day 14.

Taking the AI produced by free hydrogels to be a baseline random average for our system (~1.8), we deduced the following gels have better comparative final alignment between days 7 and 14: 12.5 µL for 2.0 mm, 1.0 mm, 0.5 mm spires; 25 µL for 1.0mm spires only. Based on our experiences handling these constructs in lab, it is very apparent that 25 µL hydrogels are more tractable to work with than 12.5 µL. Hence, we decided to consider this hydrogel configuration for future work.

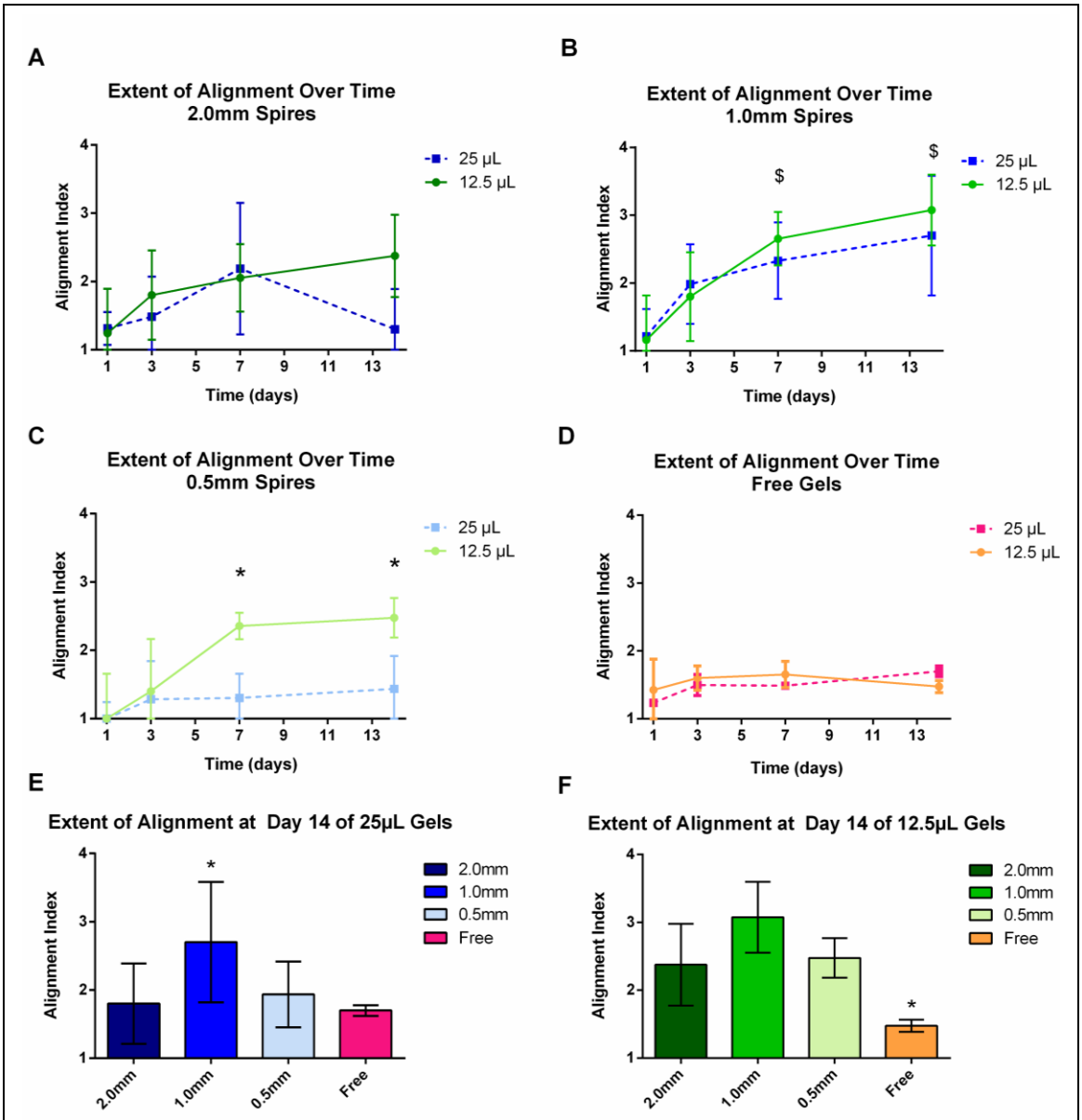

Figure 21: Quantification of extent of alignment in gel configurations between (A) 2.0 mm, (B) 1.0 mm, (C) 0.5 mm spire configurations, and (D) free gels with 12.5 µL and 25 µL toroidal gel volumes by image analysis over time. (E) At day 14, 25 µL gels show differing extents of alignment, as measured by AI, between spire-toroids and free gels. 1.0 mm spire-toroids produce significantly higher AI than all other groups, while differences between 2.0 or 0.5 mm spire toroids, and free gels were not significant. (F) Also at day 14, 12.5 µL gels exhibit differing extent of alignment between the AI for freely-cast, bulk hydrogels compared to all other spire-toroids configurations, where the free gels is significantly different to remaining groups. ($n \geq 6$, $p < 0.05$)

ACh and caffeine-stimulated force production

To generate cell-laden hydrogels, four-arm PEG–MAL macromers were functionalized with RGD, followed by the addition of cells, then crosslinker, and immediately cast around 2.0, 1.0, and 0.5 mm spires. After 12 days in culture, the gels were carefully placed on the measurement setup and immersed in PBS for stabilization, followed by agonists, as described in Materials and Methods. 'Baseline' values for each condition (aligned, unaligned and cell-free hydrogels) when hydrogels did not contract were obtained from constructs exposed to physiological conditions as PBS solution. Agonists ACh and caffeine were used to stimulate force production. Exposure to blebbistatin was used as an inhibitory condition to show that the force generation was myosin mediated. Gels exposed to PBS instead of agonist were used as controls. Cell-laden toroidal hydrogels, cell-laden free-floating bulk hydrogels, and cell-free toroid hydrogels were utilized as test conditions. After PBS stabilization on the measurement setup, constructs were either tested in one, or two additional solutions as described in Table 6. The stabilized measured voltage signal, converted to force values in μNewtons, (hereby referred to as 'signal'), is shown in Figure 22, when the hydrogel is exposed to contractile agonists and placed under physiological conditions.

There are several ways in which a hydrogel-cell composite of the nature generated in this study could shorten in length, or contract. The first is osmotic, where the difference in ion concentration can affect hydrogel swelling or de-swelling, in the case of macroscopic gel contraction. Second, cell-mediated contraction as a result of the contractile machinery present in all living cells as core functionality. Although this type of contraction could be enhanced by stimuli or the cell's microenvironment, it is an

intrinsic property of the cell, and will occur consistently in strength for a given cell type in controlled culture conditions [201]. The type of specialized contraction significant for this study of muscle tissue-constructs is cell-mediated sarcomeric myosin based contraction. We showed that all hydrogel configurations in physiological conditions did not contract as signal measured was not significantly different to baseline readings (Figure 22A). Agonistic and blebbistatin solutions were produced using physiological PBS buffer to ensure osmotic gradients are controlled and do not impact contraction. The lack of contraction in cell-free hydrogels compared to cell-encapsulated hydrogels in response to agonists, acetylcholine and caffeine, suggests the contraction of hydrogels is cell-driven by processes that respond to said agonists. The significant differences observed between the two cell-encapsulated conditions: bulk (randomly aligned) and toroidal (aligned) configuration suggest the positive impact of alignment on the extent of contraction. Finally, the use of blebbistatin as a myosin inhibitor confirms the contraction is myosin mediated and inhibited in the presence of the agent.

Traces in Figure 22A show force development over the course of different experimental solutions: PBS, agonist, and blebbistatin shown across three panels. The traces are shown for 1.0 mm spire-toroids but are comparable to those observed in other hydrogel configurations that produced contraction. First, no force production is observed for the total time spent in PBS (Figure 22A, panel 1). Peak force production occurs in the presence of the agonists occurs within first 20-30 seconds, with an average duration of 16 ± 5 seconds (Figure 22A, panel 2). This time to peak and duration of response is comparable to past work [128, 129], as also previously discussed. Suggested reasoning for this behavior can be drawn from the limited resources available to the tissue-

engineered construct. It is likely that myosin units contract until they fatigue by depleting internal calcium ion stores [148], and are unable to recover within the remaining 30-40 seconds in agonist to contract again. After the duration of time spent in agonist, constructs placed in blebbistatin do not contract, resulting in a baseline force reading (Figure 22A). Contraction forces are inhibited in the presence of blebbistatin applied before (Figure 22B) as well as after the agonist solution. In the presence of PBS or blebbistatin alone no force production is observed.

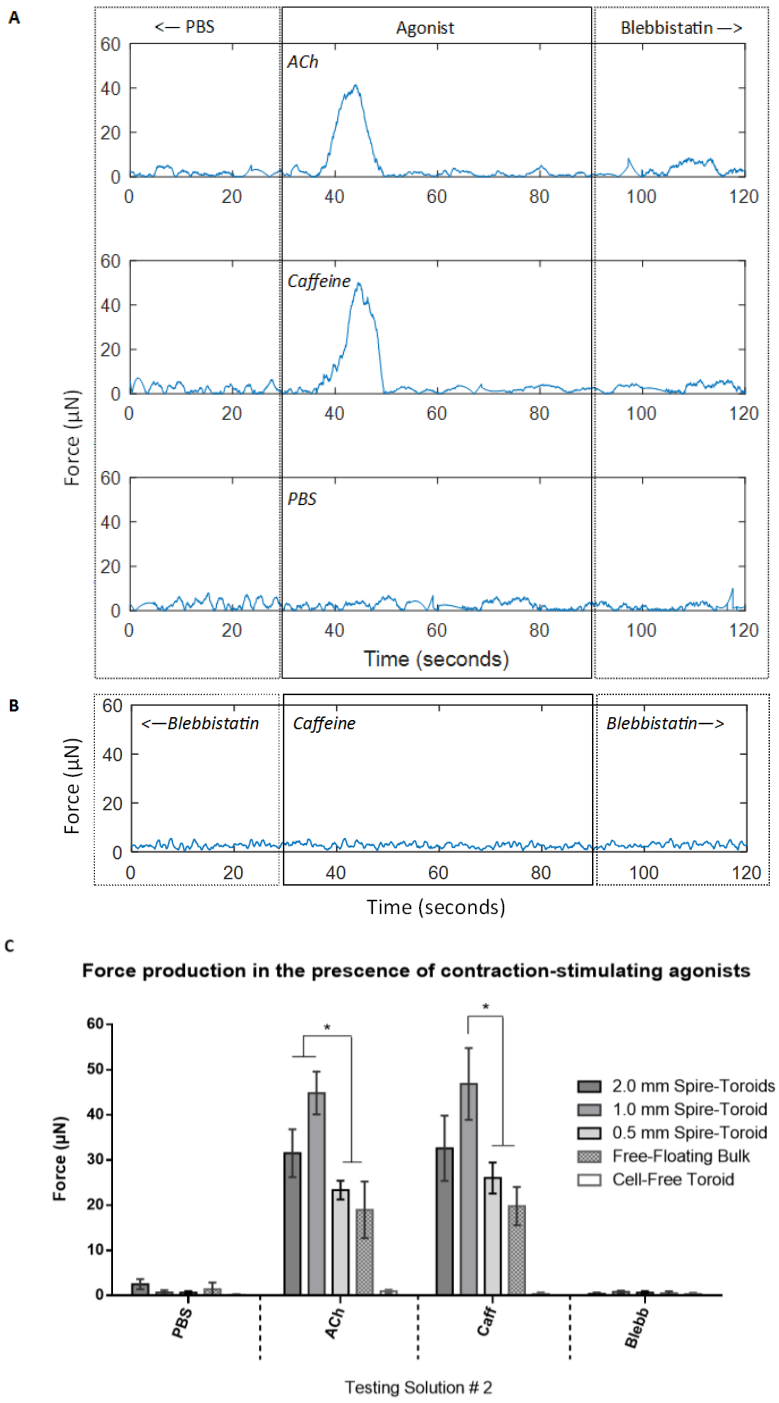

Figure 22: Quantification of contraction forces produced upon activation. (A) Shows traces for 1.0mm spire-toroid samples subjected to three different conditions: PBS for stabilization solution #1, testing solution #2 (60 second duration), and blebbistatin as solution #3. (B) Shows summary data of the spire-toroids, free floating bulk and cell-free gels exposed to different test conditions. No significant differences were found between free-2.0 and 1.0mm toroids under all conditions. Significant differences exist between cell-free hydrogels and all cell encapsulated hydrogel configurations for exposure to each agonist (*). Significance was assessed using $p < 0.05$ and a minimum of five gels were tested per condition ($n \geq 5$).

We observed that contraction is stimulated in the presence of agonists that have been shown to depolarize the cell membrane and enable ion flux for the myosin and actin filaments within sarcomeric units to slide along each other, thereby generating force [14, 198]. When stimulated using ACh, 1.0 and 2.0 mm spire toroids produced the highest forces of 48 μN (Figure 22B) and 36 μN respectively. The free floating hydrogels with cells produced significantly lower forces compared to the 1.0 and 2.0 mm spire-toroid conditions (Figure 22B). When exposed to 50 mM caffeine, 1.0 mm spire-toroids produce forces of up to 53 μN, while 2.0 mm spire-toroids generate 39 μN. The forces generated in 1.0 mm spire-toroids are significantly higher than those generated by free-floating bulk gels and 0.5 mm spire-toroids (Figure 22B). The consistently highest forces measured for 25 μL hydrogel volumes were in 1.0 mm spire-toroids in caffeine (46.8 ± 7.9 μN) and ACh (44.8 ± 4.7 μN). 1.0 mm had previously been shown to have the highest relative alignment index (2.4) of all groups tested. The contraction forces produced by free gels, with encapsulated cells are expected to be the result of randomly aligned cells (previously measured AI for this condition: 1.3) responding to the activating solution.

Discussion

Cellular alignment is a crucial aspect of functional skeletal muscle generation [115]. Yet in vitro methods to create 3D aligned skeletal muscle tissue with synthetic scaffolds are limited, or utilize overly complicated methods of dynamic signaling that vary with setup and choice of biomaterial. Specifically, past efforts to impose mechanical tension on skeletal muscle constructs have relied on externally generated, applied forces. Such

works have suffered from complexity associated with maintaining that tension as the muscle construct develops. In this study, we demonstrate the use of a static geometric cue to generate circumferential stresses in toroids for the development of alignment.

We previously identified an optimal hydrogel configuration using the established PEG hydrogel formulation (5% w/v four-arm PEG–MAL macromers functionalized with 2.0 mm RGD adhesion peptide, and cross-linked by a MMP-degradable peptide) that supported C2C12 mouse myoblast viability and intrinsic-level, random, alignment.

We attribute the physical differences (hydrogel volumes and surface area ratios) between toroidal configurations and free or linear hydrogels to the physical stability and differential stresses experienced by the encapsulated cells as they form alignment. The consistency of cellular viability, as shown using % live cells, however, suggests that viability is generally unaffected by geometry with use of the consistent, previously established, PEG hydrogel formulation.

2D micropatterning techniques have enabled researchers to print organic molecules on substrates, providing geometrical cues that regulate the location, shape and even alignment of C2C12 cells on surfaces [153, 202, 203]. Similarly, the use of geometrical cues in 3D have to some extent replicated this directionality and allowed researchers to study the effect of the physiologically complex microenvironment on cell fate as experienced in vivo [204].

It has been shown that physical cues, in 2D and 3D, lead to different tractional stress patterns and promote cytoskeletal reorganization [82]. Particularly, Piyush et al. show that different physical structures (linear vs. toroidal shapes) induce different stress patterns [205] from differential activation of the Rho/ROCK pathway [206], which

together impact the extent of C2C12 differentiation [207]. It was shown that von Mises stresses vary throughout different gel configurations, where free gels exhibited the highest stress at outer edges, linear gels showed highest stress at the corners of the linear portion and torus shapes (though on an order of magnitude smaller size scale than those generated here with a diameter of 200 μm) showed highest stresses on the outer convex outer edge than the concave inner edge. A positive correlation was found to exist between stress distribution and cellular alignment [82]. It is likely that these physical characteristics impacted cell proliferation and alignment resulting in differences between groups, specifically DNA content and alignment, between the free and spire-toroids hydrogels.

Figure 23 shows the theoretical non-dimensional stresses experienced within a toroid. This model is obtained from the work of Tanner et al, and modified based on findings from Sutcliffe et al and Veličković et al [1, 208, 209]. Though the model is based on the assumption of a circular toroidal cross-section, it demonstrates the changes in stress over distance in the circumferential and radial, or, meridional, directions in a manner similar to toroids with elliptical cross section [208].

The graph depicting the toroidal reconstruction shows non-dimensional stresses in the circumferential direction to be greater than those in the radial one. If the ratio of the ID:OD were to increase (Figure 23C), these stress patterns would change to maintain the integrity of the toroidal shape. The model shows that for a given phase angle on the periphery of the torus, both radial and von Mises stresses decrease proportionally to the increase in ID:OD ratio [209]. This scenario would be analogous to increasing the

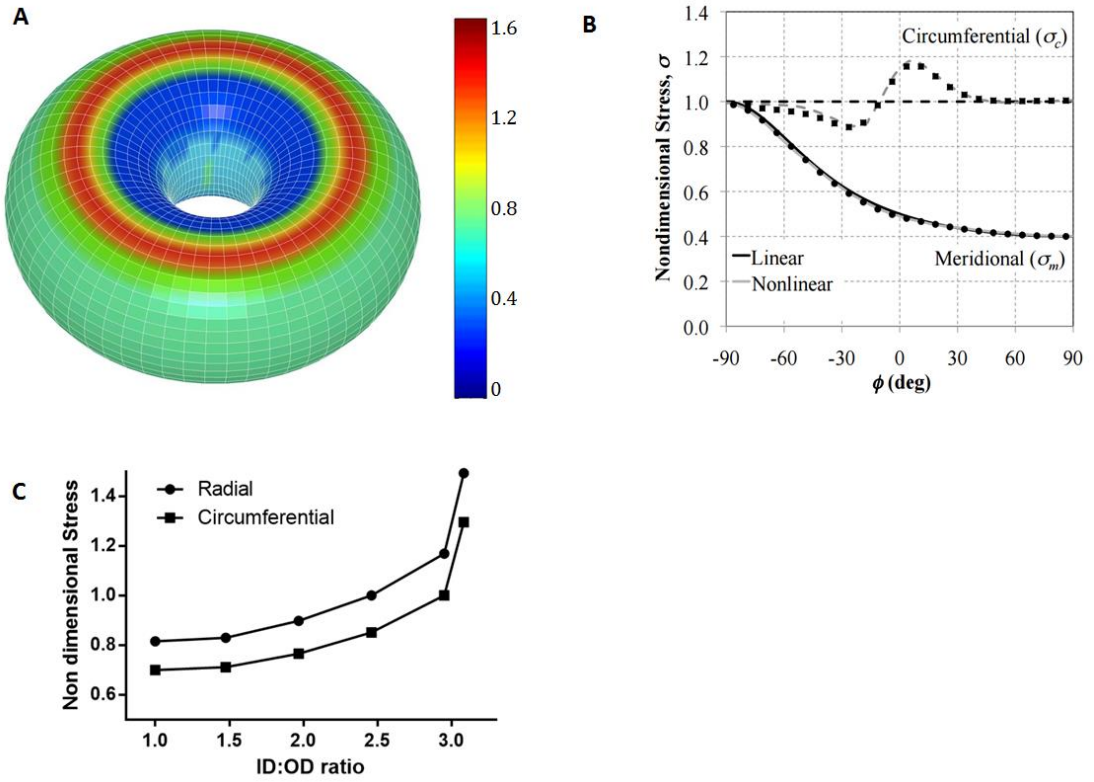

Figure 23: Normalized stress patterns in a toroid, as published by Tanner et al, 2010 [1]. (A) Shows contour lines representing predicted circumferential stress in a toroid (c=2/3, where c is the ratio of minor to major radii), as solved using Sanders' non-linear theory for accurately predicting torus stresses in both the meridional and circumferential directions. Image was generated using finite element method (FEM) analysis in the LS_DYNA stimulation software package. (B) Depicts the change in non-dimensional stress over phase angle from the outer periphery of the circular cross section of the toroid (-90 deg) to the inner radius [1]. (C) Demonstrates the increase in non-dimensional radial and circumferential von Mises stresses, for $\phi = 0$ degrees, as the ratio between the minor radius, (ID) and the major radius, (OD) increases with OD held constant, derived from the model described by Tanner et al [1].

diameter of the central spire diameter in our study, suggesting that the larger the spire-toroid, the smaller the non-dimensional stresses in the circumferential direction. This model would suggest the alignment indices in 1.0 and 0.5 mm spire-toroids be higher than those in 2.0 mm spire-toroids. However, we have observed lower alignment in 0.5 mm spire-toroids, comparable to those of 2.0 mm spire-toroids. This leads us to consider that while geometric cues and resultant stress patterns play a significant role in the development of alignment within toroidal muscle construct, it is likely that a dominant factor in alignment modulation, surface area to volume ratios, and gel swelling and compaction can be attributed to the cellular behavior. Namely, their density, viability, extent of differentiation, and the time spent in culture. Theoretically, higher stress regions should enable greater alignment, even prior to differentiation of cells, as known through the link between matrix environment and cellular behavior [204]. However, as encapsulated cells grow and remodel their matrix, it is expected that these stress patterns change over time.

We have previously detailed how varying hydrogel formulations with different cell densities can modulate encapsulated cell growth and proliferation [6]. However, the effect of these formulations and consequent cellular behavior to study macroscopic changes in hydrogel swelling and compaction were not discussed. In this study we have observed hydrogel configurations impact the ratios of swelling and compaction, through the development of internal stresses that modulate cell proliferation, and in turn, cell spreading, contractility, and hydrogel degradation. A suggested order for this process is (i) initial hydrogel swelling, (ii) cellular proliferation and development, which leads to

(iii) hydrogel remodeling, and finally (iv) long-term stable hydrogel compaction for the support of the cellular structures with their self-generated matrix.

Physical characteristics important for hydrogel longevity and end construct tractability are related to cell density, and the ratio between hydrogel surface area and volume. We observed that a high (above 2.4) surface area to volume ratio, such as those with linear hydrogels increases the rate of hydrogel degradation. A higher ratio of surface area to volume values is known to increase diffusion rate and efficiency [210]. This correlates with increased degradation and loss of tractability of the linear hydrogels possibly through improved transport of degradative enzymes, such as matrix metalloproteases (MMPs) released by cells, and opportunity for cell motility. Additionally, it is possible that the linear gels in this configuration degrade due to their inability to produce internal stress or tension on a scale similar to the toroidal gel.

The increases in DNA content over time with constant percentages of live cells are likely indicators of cellular proliferation. Results show a higher rate of increase in cell numbers in spire-toroid hydrogels, while free and linear samples maintain the DNA content with which they were seeded. We posit the differences in DNA content between spire-toroids and free or linear hydrogels are likely due to the differences in geometrical configuration. It has been shown that physical cues are necessary and can influence the development of alignment [47, 123, 127]. We chose to continue using free floating hydrogels in the comparisons studied as a negative control that previously supported good cell viability but no alignment. The linear hydrogel configuration was intended as a uniaxial, geometrical control with two anchorage points. The use of two (or more)

anchorage points is common [132, 146, 169], though the translation of these constructs for soft robotics or SMTE is limited due to strong adhesion to secondary substrates, and the use of naturally derived scaffolds.

The advantages of the toroidal shaped hydrogel are twofold: (i) a single, constant physical cue allows minimal interference during culture for the production of anisotropy and (ii) the central hole of the torus allows facile attachment to a force-measuring apparatus for the next goal of this study in generating a functional muscle construct. The described technique to generate toroidal hydrogels is high throughput, scalable, and may be useful in when conducting repetitive studies with many groups in vitro, such as for drug screening assays.

It has been demonstrated that cells respond to cues in their microenvironment, and here we show how PEG-MAL hydrogels can be cast in a manner to induce embedded cells to circumferentially align. These methods can be translated to other cell lines that rely on anisotropy for function, or other scaffolds for the exploration of a wider range of biomaterials for tissue engineering.

Methods of contraction measurement vary greatly with the target scale of the tissue construct or cell structures. Myotubes or single cell measures can be made on cantilevers with patch-clamp stimulation [143], while whole muscle tissues can be stimulated with electrical signal , neuro-muscular activation, or biochemical agents, and use commercially available or custom-built force measurement devices. The scale in between these two extremes poses many challenges to force measurement. First, the scale of the

construct is smaller than native tissue, often with weaker mechanical properties, lowering its ease of handleability, and second, the forces produced are on the order of micro-Newtons, and extremely sensitive components are required for their detection. These issues are circumvented by attaching the construct to a stiffer substrate [10], or indirectly measuring force through the observation of secondary structure deflection (posts, anchors, and the like) associated with the tissue construct [132, 146, 154].

For this study, we focused on building a construct measurement device that would characterize forces generated by an actuator not tethered to external materials or bound to permanent anchors. We chose the method of attaching a construct using hooks onto a measurement setup which would only be possible in a minimally invasive manner if there was an avenue for the hooks to be passed through the construct, a configuration provided by a torus shape. Hence, toroidal hydrogels with encapsulated circumferential cell alignment were developed.

Existing works do not provide enough detailed information to rebuild existing force measurement devices [121, 122, 148], resulting in different groups using custom built devices and force transducers to suit their needs. This increases the difficulty of comparing information across groups, highlighting the need for a common method of force measurement for tissue engineered constructs of specific size and force scales. For these reasons, we expect the utilization of this measurement device to span not only skeletal muscle constructs but also enable mechanical stimulation (using the ability of the stationary arm to connect with a motor) and isotonic force measurements.

Our results show that toroidal hydrogels respond to acetylcholine and caffeine when used as agonists in solution form. The highest peak force produced is 48 μN (0.4 kPa) by

the 25 µL toroid gels generated around the 1.0 mm diameter spire. The previously measured AI of 2.4 for the same hydrogel condition underscores the correlation between alignment and force production for engineered skeletal muscle constructs. Reductions back to baseline after continued treatment with agonist are likely due to the inability of the construct to sustain muscular contraction over longer periods of time [148]. Duration and peaks of forces produced are consistent with those previously seen in literature [128, 129] and any differences are likely related to the nature of stimulation (diffusion of molecular agents as opposed to electrical stimulation) and differences in physical characteristics of developed C2C12 construct (dimensions, cell density). The lack of contraction produced by cell-free hydrogels suggests that all contraction is cell-mediated. The loss of force production in the presence of myosin-inhibiting blebbistatin demonstrates the utilization of cellular machinery in developing contraction for force.

Other constructs at this size scale produced with C2C12 cells have reported force values at peak tetanic contraction, in the range of 33.2 µN (2.35 kPa) [128, 129] to 45 µN (1.12 kPa) [146]. Although it is difficult to compare the higher forces generated by these constructs as they utilized biological matrices, and different culture conditions, our use of synthetic scaffolds to generate forces of a comparable scale is noteworthy. The limitations of biological scaffolds have been previously discussed (lack of reproducibility, high immunogenicity). In this study, we have developed a viable methodology for producing aligned and functional SMTE constructs that produce forces comparable to those previously published, but utilizing a synthetic scaffold in combination with a toroidal hydrogel configuration.

It is likely that some portion of cells remained undifferentiated (up to 30% that do not produce sarcomeric myosin, as previously shown [6]). The lack of differentiation would result in diffuse presentation of nAChRs, underdeveloped t-tubules, and poorly connected sarcolemma [211, 212]. These factors likely contributed to decreasing the forces generated by our skeletal muscle constructs. It must be noted that it is unlikely that diffusion based delay affected transport efficiency as the hydrogels can be estimated to 80-95% water, by day 14, resulting in diffusion times on the order of nanoseconds (Appendix B.3).

Functional output is an inherent and essential part to skeletal muscle tissue engineering. Here, we show that the optimal hydrogel configuration using the established PEG hydrogel formulation (5% w/v four-arm PEG–MAL macromers functionalized with 2.0 mm RGD adhesion peptide, and crosslinked by a MMP-degradable peptide) that supports C2C12 mouse myoblast viability and alignment, is also capable of functional contraction. A custom built device enabled these measurements to be taken with a high sampling rate and signal to noise ratio.

Building a custom force measurement instrument in-house allows easy signal modulation at the circuit level, and is amenable for setup configuration modifications to accommodate other constructs, or the addition of dynamic mechanical or electrical signaling. Functional capability of the generated muscle construct encourages the continued exploration of PEG-based hydrogels for skeletal muscle tissue engineering and actuator generation.

Conclusion

The goal of this study was to develop a suitable configuration for the established synthetic scaffold as the second step towards building contractile muscle constructs. Previously, we determined synthetic PEG scaffolds that provide a consistent, engineerable, and modularly controllable starting material as a scaffold for skeletal muscle tissue development. Here, we enabled 3D alignment of C2C12 cells homogenously seeded within this biofunctional matrix.

With our increasing knowledge of myogenesis and tissue regeneration we can further engineer scaffolds that promote myogenesis by (i) utilizing dynamic signaling from mechanical or electrical stimulation, (ii) designing scaffolds for growth factor release, or (iii) further modelling materials to have physical features that promote desired properties of native tissue in vitro.

This study aimed to contribute to the current body of work replicating cellular anisotropy in vitro, leading to a better understanding of cellular developmental processes. The production of functional skeletal muscle tissue constructs, will aid as a regenerative solution to skeletal muscle loss, as well as a force actuator for cellular machines [9].

The secondary goal of this study was to develop a method of force measurement for the toroidal muscle cell-gel composites as the next step towards building contractile muscle constructs. We tested the functionality of this alignment through the use of a custom-built measurement apparatus to find that the most force was generated from hydrogel conditions that had the highest alignment index, suggesting the positive correlation with structure and function for skeletal muscle tissue.

This study aimed to develop a force measurement method that was easily replicable for use with skeletal muscle cell-hydrogels and other tissue constructs that exhibit contraction in the tens of μN to 100 mN range. In addition, the demonstration of contractility of the generated toroidal gel constructs shows the existence of functionality in the constructs produced. This contractile, toroidal cell-hydrogel The production of functional skeletal muscle tissue constructs will aid as a regenerative solution to skeletal muscle loss, as well as a force actuator for cellular machines [9].

Acknowledgements

We would like to acknowledge the assistance of Dr. Julia Raykin in the development of the MATLAB code for the alignment analysis. Dr. Thomas Burkholder provided many vital inputs to the design of the contractile experiments. In addition, acknowledgment is due to Dr. Richard Nichols, Yogi Patel, and Dr. Robert Butera for providing materials and knowledge expertise towards the construction of the force measurement device. Brandon Williams also provided assistance through reverse engineering of the molds, and measurement setup in addition to building and troubleshooting the circuitry.

CHAPTER V: FUTURE DIRECTIONS

Introduction

In this thesis we have detailed a specific skeletal muscle hydrogel construct, its fabrication techniques, and functionality; yet there are other challenges outside the scope of this study that would need to be tackled to move the field of skeletal muscle tissue engineering (SKMTE) and soft tissue robotics closer to the goals of generating (i) dense, innervated, and vascularized 3D muscle at the tissue scale [115] and (ii) a self-sustaining and self-controlled biological machine [213]. Current and future challenges to 3D SKMTE include a viable cell source; in vitro maintenance of constructs; vascularization and innervation strategies upon implantation [115]. To address these challenges, next steps could involve elucidating the effects of co-culture of cells for innervation and vascularization; multifunctional scaffold development for growth factor release; enhanced in vitro myogenesis through the use of mechanical and electrical stimulation, to name a few.

Skeletal Muscle Tissue Engineering

Cell Source

For this study, using C2C12 cells was a simple way to demonstrate the utility of static geometric cues, as well as develop translatable techniques to quantify alignment in complex 3D structures and measure forces on a μN scale. There are significant limitations of using cell lines in replicating in vivo myogenesis, namely, the risk that they

may behave differently to primary cells under stress. Yet the widespread use of C2C12 myoblasts and their ease of use make them an ideal choice for technology development platforms such as those described in this study. Though constructs engineered using primary-derived skeletal muscle generate higher contractile forces, these cells are limited by their ability to be expanded in vitro and loss of myogenic potential with increasing passage number [115]. Ideally, future work would involve the development of an immortalized cell line that can be as easily propagated as C2C12s but with a capacity to differentiate into highly contractile myotubes, similar to those formed by primary-derived and muscle stem cells [115]. Finally, in considering the clinical application of muscle constructs for human volumetric muscle loss (VML) repair, primary myoblasts from humans must be studied for feasibility as a cell source. Derivation of new cell lines is associated with high financial and time costs. Obtaining cells from human tissues additionally raise ethical, legal, authentication, and pathogenicity concerns. Future work in this field would have to address these challenges in order to produce an effective bioengineered human VML solution.

Relevance of Biomolecules

The biomolecules, RGD, RDG, VPM, for short, were used in this study for the development of a simple, reproducible hydrogel matrix for C2C12 support demonstrating the capability of the PEG hydrogel system for biological microenvironment generation. This system facilitates the modular comparison of hydrogel parameters (matrix density, degradation, swelling) in conjunction with cellular factors (survival, functionality) in the

development of biological niches. It must be noted that these parameters are not entirely independent to each other and this constraint must be considered when examining data.

The criteria for success for the translation of these biomolecules for use in other hydrogel systems, or with other cell types would involve testing the capability of system combinations for (i) cell viability, (ii) proliferation (iii) stability post-differentiation. The end goal of the utility of the optimized product: differentiated cells in a matrix, would dictate further application-specific success criteria. These may include, but are not limited to: the directionality of the constructs, cellular functionality (growth factor or cytokine release profiles), and the constructs ability to be implanted, interact with other tissues and integrate into the host.

Long-term maintenance of in vitro Muscle Constructs

Cell culture support of in vitro generated muscle constructs involves operation in a narrow range of environmental conditions, as with any cell culture. However, the maintenance of muscle tissue in stable, differentiated state had proven difficult: in 2D, myotubes on micropatterned substrates peel off after one week of differentiation [153], and in 3D, the longevity of constructs has been described as 2-3 weeks [125-128, 197]. These lifetimes may not impact short-term purposes of soft-robotics (though cost of production could increase), but significantly limits the notion that muscle constructs can be generated to near-full differentiation in vitro before implantation for successful treatment of VML or muscular dystrophies. Future work may involve defining an acceptable time frame for partial differentiation of in vitro culture prior to successful

integration post-implantation, or the exploration of culture techniques, and cell sources that lengthen longevity of stable, differentiated myotubes.

Vascularization and Innervation

Dense, engineered skeletal muscle tissue requires the support of a vascular network at a comparable density to that found in native tissue to meet the metabolic demands of muscle cells. Thickness of current muscle constructs are constrained by the limits of oxygen diffusion in the absence of vascular networks. However, current constructs operate in a large volume of media where this is not a primary concern. Advances in microfabrication and 3D printing have demonstrated that it is possible to build microvessel networks in in vitro[167]. Although these techniques are yet to be utilized for the development of vascular networks in 3D muscle constructs, they demonstrate the potential to do so.

At the cellular scale, recent work involving co-culture of skeletal muscle cells with neural cells has shown increased myotube activation and neuro-muscular junction formation [202]. Additionally, incorporating vasculature is vital to create self-sustained muscle actuators of greater dimensions. Muscle progenitor cells and myoblasts grown with endothelial cells produced tissue constructs displaying improved angiogenesis without the need for external growth factor signaling [214, 215]. Future work in this field seems to be headed in the direction of co-culture for the development of well-differentiated muscle tissue with associated neuronal innervation and vascularization.

The role of Biomaterials

To further generate tissue-scale skeletal muscle constructs in vitro that better replicate native tissue, multifunctional tissue scaffolds for growth factor release; bioreactor designs; and dynamic stimulation using mechanical and electrical signals become relevant. Materials used must be further considered to support the infiltration of host cells, such as macrophages, fibroblasts and endothelial cells, while promoting vasculature through the release of growth factors or soluble mediators to promote cell survival and engraftment for clinical applications [167].

Biomaterials can and will be exploited as tools that modulate cellular behaviors and fate through the presentation of physical and biochemical cues [13]. For instance, the treatment of volumetric muscle loss, or genetic disorders such as muscular dystrophy could be envisioned by using mechanically compatible, morphogen presenting, injectable hydrogels, which not only provide structural support, but also induce endogenous regeneration by selectively activating resident muscle cells [8]. Similarly, traumatized muscles could be repaired using fibrous meshes wrapped around the defect site, guiding muscle regeneration via topographical cues [8]. Fucoco et al demonstrated the ability of PEG-fibrinogen hydrogels to ‘rejuvenate’ adult skeletal muscle-derived pericytes, which typically have impaired myogenic differentiation in vitro, and enable muscle regeneration on a scale comparable to younger muscle-derived pericytes [103], suggesting the value of the choice of artificial matrices when developing muscle constructs.

Multifunctional or hybrid biomaterial scaffolds would modulate cellular behavior and enhance myogenic differentiation through the spatiotemporal release of growth factors. Growth factors tested for their efficacy on myotube formation, contraction, and stability

are VEGF [216], HGF [137], insulin growth factor-1 (IGF-1) [217, 218], neural growth factor (NGF) [73, 216] , fibroblastic growth factor (FGF) [219], and transforming growth factor-beta (TGF-ß1). These growth factors are precisely orchestrated in vivo. HGF, for instance, promotes muscle regeneration at early stages, but inhibits late-stage differentiation during muscle repair [137]. Further exploring growth factor delivery, dual delivery of HGF & VEGF [162] and FGF-2 & HGF have also been associated with improved myofiber generation. Hence, future work in biomaterials could involve engineering the key functional property of spatiotemporal (dual) drug release.

The PEG hydrogel platform described in this study has demonstrated functionality in other tissues, being used for 1) testing the effects of angiogenesis on bone reparation and stem cell survival in vivo and 2) engineering a biomaterial to sustain cell survival and engraftment in tissue engineered constructs [220, 221]. The next step for this SKMTE project would include development of an in vivo skeletal muscle ischemia model to further test its efficacy. It is already evident that biomaterials play a crucial role in muscle regeneration therapies, and material scientists are now working together with clinicians and stem cell biologists in interdisciplinary teams to translate existing biomaterial and cell based therapies into the clinic [8]. The use of methodologies developed here would enable translation to human-derived cells for use in regenerative therapies, or further studies on human disease states.

Tissue Engineering Beyond Skeletal Muscle

From a clinical perspective, patients suffering from muscular dystrophy, also experience respiratory and cardiac function decline. There exists an interesting link

between cardiac and skeletal muscle health. Baum et al found that strength training is an important part of cardiac rehabilitation [222, 223]. While Heineke et al found that the ablation of the myostatin gene in cardiomyocytes prevented skeletal muscle atrophy in a pressure overload model of heart failure. Other muscle factors such as insulin-like growth factor are also suggested to be important for cardiac-mediated effects on skeletal muscle growth [222]. Although differing in morphology and alignment, cardiomyocytes and skeletal myofibers share a similar cellular architecture, notably through their common use of the protein dystrophin, that links transmembrane protein to the extracellular matrix [223]. Both cell types are found to be susceptible to contraction-induced disruption in the absence of dystrophin [224, 225] . In muscular dystrophy, the dysfunction of diaphragm, abdominal, and intercostal muscles necessary for respiration occurs early and results in decreased respiratory function [226, 227]. Hypoventilation and hypoxia increase pulmonary artery pressure, raising the workload of the right ventricle, and exacerbating cardiomyocte defects [223]. The identification and further experimentation of specific genes will shed further light on the interplay between muscle and heart function in the future, leading to new pathways to exploit for diagnostics and therapeutics.

Skeletal muscle insulin resistance is a characteristic pathology of type 2 diabetes [228]. A potential therapy could involve the restoration of insulin acceptance in skeletal muscle tissue through the in vitro development of muscle constructs with encapsulated engineered cells. In summary, the engineering of skeletal muscle constructs today could impact the fields of type 2 diabetes, respiratory and cardiac dysfunctions.

The development of vascularization techniques and neuronal activation are physiologically relevant to most tissues in the human body and the procedures developed

here to optimize hydrogel formulations for cellular behavior may enable the development of better tissue-engineered products.

Soft Robotics for Biological Machines

There have been few notable muscle powered soft robots [10, 229]. Integration of cardiomyocyte muscle actuators into devices has led to basic muscle-powered devices such as grippers and pumps as well as more sophisticated muscle-powered soft robots that walk and swim [213]. These studies have primarily used neonatal rat cardiomyocytes that are already differentiated into contractile muscle cells. Future work should involve translating these techniques using skeletal muscle cells that are more amenable to stimulated, not spontaneous, contraction. For this purpose, optical methods of excitation are particularly interesting, as a non-invasive, and controlled stimulation [145, 169, 230]. The transition will require understanding the role of substrate stiffness and the mechanical environment, engineering the spatial organization of biochemical and physical cues to guide muscle alignment, and developing bioreactors for mechanical and electrical conditioning. Neuromuscular constructs formed by co-culturing or patterning skeletal muscle progenitor cells with neural cells are attractive components of biological machines as soft-actuators that can be specifically controlled [231]. Looking forward, current and future challenges include identifying the best source of muscle precursor cells to expand and differentiate into myotubes, replacing cardio myocytes with skeletal muscle tissue as the bio-actuator of choice for soft robots, and vascularization and innervation strategies to enable control and nourishment of larger muscle tissue constructs [115].

Innovative Uses for Muscle Tissue

Engineered muscle tissues can also be used for the large scale production of tissues to be used as a disease model for in vitro drug screenings of muscle-specific disease states [154]. Understanding endogenous regeneration cascades and their alteration in clinically relevant scenarios is essential to engineering biomaterials for therapies involving cells. In addition, artificially engineered muscle is becoming increasingly researched as a possible meat alternative [232].

APPENDIX A

DUAL DELIVERY OF HEPATOCYTE AND VASCULAR ENDOTHELIAL GROWTH FACTORS VIA A PROTEASE-DEGRADABLE HYDROGEL IMPROVES CARDIAC FUNCTION IN RATS*

Abstract

Acute myocardial infarction (MI) caused by ischemia and reperfusion (IR) is the most common cause of cardiac dysfunction due to local cell death and a temporally regulated inflammatory response. Current therapeutics are limited by delivery vehicles that do not address spatial and temporal aspects of healing. The aim of this study was to engineer biotherapeutic delivery materials to harness endogenous cell repair to enhance myocardial repair and function. We have previously engineered poly(ethylene glycol) (PEG)-based hydrogels to present cell adhesive motifs and deliver VEGF to promote vascularization in vivo. In the current study, bioactive hydrogels with a protease-degradable crosslinker were loaded with hepatocyte and vascular endothelial growth factors (HGF and VEGF, respectively) and delivered to the infarcted myocardium of rats. Release of both growth factors was accelerated in the presence of collagenase due to hydrogel degradation. When delivered to the border zones following ischemia-reperfusion injury, there was no acute effect on cardiac function as measured by echocardiography. Over time there was a significant increase in angiogenesis, stem cell

---

* Adapted from: Salimath AS, Phelps EA, Boopathy AV, Che P, Brown M, García AJ, et al. (2012) *Dual Delivery of Hepatocyte and Vascular Endothelial Growth Factors via a Protease-Degradable Hydrogel Improves Cardiac Function in Rats.* PLoS ONE 7(11): e50980. doi:10.1371/journal.pone.0050980

recruitment, and a decrease in fibrosis in the dual growth factor delivery group that was significant compared with single growth factor therapy. This led to an improvement in chronic function as measured by both invasive hemodynamics and echocardiography. These data demonstrate that dual growth factor release of HGF and VEGF from a bioactive hydrogel has the capacity to significantly improve cardiac remodeling and function following IR injury.

Introduction

Cardiovascular disease is the leading cause of death in the United States, with estimates indicating 1 death every 39 seconds. Coronary heart disease, specifically myocardial infarctions (MI), accounts for 1 of every 6 deaths in the Unites States with over 1 million new, recurrent, and silent MI annually [233]. Following an occlusive coronary event, patients are treated with percutaneous coronary intervention to clear the affected vessel and restore blood flow [234]. While lifesaving, the ischemia and subsequent reperfusion (IR) induces massive regional necrosis and apoptosis, with billions of myocytes being lost over the first few days [235-237]. These lost cells are not replaced and a non-contractile scar is laid down, which will eventually lead to heart failure. Currently, the only definitive cure for heart failure is cardiac transplantation, and the number of donor hearts needed vastly outweighs availability. Thus, new therapies to treat this progressive disease and improve cardiac function are greatly needed.

Because the loss of tissue is highly localized, and the endogenous response is not sufficient for repair, recent efforts have focused on replacement of the lost cells using a

variety of treatment options[238]. In recent years, many clinical studies have been initiated to deliver localized therapy in the form of various cell types for reconstitution of the myocardium. However, there is much debate on the optimal cell type, whether or not stem cells can differentiate into functional myocardium and the long-term effects of these non-myocytes [239, 240]. In addition to exogenous cell delivery, paracrine effects arising from delivery of angiogenic factors and other biochemical agents suggest that the myocardium retains the ability to remodel and heal [241]. Understandably, there has been tremendous focus on both growth factor- and gene therapy-based therapeutics. Whereas a source of great promise, direct growth factor delivery to the myocardium will most likely be inefficient as several studies have noted that many of these proteins are carried away in the highly vascularized cardiac tissue thereby limiting the effective tissue dose [218, 242, 243]. Gene therapy, while providing an excellent analytical tool, has not met with enthusiasm clinically, mostly due to the inability to quantify delivery and nonspecific targeting in vivo.

The need for spatiotemporal control to treat cardiac dysfunction is clear because ischemia/reperfusion (IR) injury is progressive with a distinct temporal and spatial response demanding distinct, controlled intervention [236]. Each of these processes is controlled by distinct mechanisms, and data suggest that therapeutics which may help at one phase may have no impact, or negative effects, at later time points. For example, small systemic doses of vascular endothelial growth factor (VEGF) improve regional blood flow following infarction; however, this did not lead to an improvement in cardiac function [244, 245]. However, large systemic doses of VEGF induce unfavorable side effects including hemangiomas, diabetic retinopathy, atherosclerosis, and rheumatoid

arthritis [246]. Thus, there is a compelling need for temporal and spatial control of therapeutic delivery as one therapeutic intervention is unlikely to be optimal for all phases of post-MI healing.

In this study, a bioactive, protease-degradable polyethylene glycol (PEG)-based hydrogel was used to deliver hepatocyte growth factor (HGF) and VEGF following acute myocardial infarction. The ability of the growth factor-laden hydrogels to improve angiogenesis, fibrosis, and progenitor cell infiltration was examined at chronic time points and functional parameters determined using clinical echocardiography and invasive hemodynamics.

Materials and Methods

Generation of PEG-hydrogel

Protease-degradable PEG-based hydrogels were prepared as previously described [12]. PEG-maleimide (PEG-MAL) 4-arm macromers (20 kDa, >95% maleimide functionalization; Laysan Bio) were pre-functionalized with GRGDSPC (RGD) adhesion peptide and growth factors (1% v/v) HGF and/or VEGF in 2.0 mM triethanolamine (TEA) solution. PEG polymer density used was 4% w/v and RGD density was 2.0 mM. The precursor molecules were cross-linked into a hydrogel by addition of a cysteine-flanked protease-degradable peptide sequence GCRDVPMSMRGGDRCG (VPM) [76, 247] (Fig. 1A). The final concentration of growth factors delivered was 1 µg VEGF (Gibco) and 1 µg HGF (US Biologicals) per 100 µl hydrogel.

In vitro Release Study

HGF and VEGF were tagged with Alexa Fluor 488, Carboxylic Acid, Succinimidyl Ester, mixed isomers (Life Technologies (Carlsbad, CA, USA) respectively), proteins were incubated at 0.1 mg/mL at a 1:50 protein to dye molar ratio in sodium bicarbonate buffer for 2 hours at 37°C, and purified into PBS by four passes through a desalting spin column (Zeba Spin Desalting Column, Pierce, 7K MWCO). Labeled protein was snap frozen in liquid N2 and stored at −80°C. Protein samples were confirmed to be labeled with respective Alexa Fluor tag, free from excess dye, by SDS-PAGE imaged on a BioRad system under Trans UV light.

To track the release of HGF and VEGF from PEG-MAL hydrogels, Alexa Fluor-tagged growth factors were pre-incubated with 4-arm PEG-MAL macromer for 1 hour and incorporated into PEG-MAL hydrogels by crosslinking remaining unreacted MAL groups with VPM protease degradable peptide. Gels were incubated in PBS alone or with 0.1 mg/mL or 0.01 mg/mL collagenase Type 1 (Worthington Biochemical) for 4 days at 37°C. Individual hydrogel volumes were 50 µL and 5 uL of tagged growth factor was added such that final concentration in the gel was equal to 0.02 mg/mL. Samples of incubation media were taken every few hours for day 1 and then every 24 hours and read using a standard fluorescence plate reader (Perkin Elmer). Percent released was calculated as fraction of the dye released/maximum loaded as compared to a standard dilution for each tagged growth factor.

Animal Studies

A randomized and blinded study was conducted using adult Sprague-Dawley rats (Charles River) weighing 250 g. Rats were randomly assigned to treatment groups (n = 7–10) using a random generator and the surgeon was only given letter codes to identify groups. While one group was subjected to sham surgery, the other eight groups received ischemia/reperfusion (IR) surgery (30 min. coronary artery ligation followed by reperfusion), with or without the injection of 100 µl (containing 1 µg) of the following: free VEGF, free HGF, free VEGF+HGF, PEG only, PEG/VEGF, PEG/HGF, or PEG/VEGF+HGF. Injections were made into the perimeter of cyanotic ischemic zone (3 locations) through a 30-gauge needle immediately after reperfusion. The animals were allowed to recover and functional assessments were made at later time points. The animals were sacrificed 21 days following surgery and the hearts were fixed in 4% paraformaldehyde, dehydrated, embedded in paraffin, and sectioned for immunohistochemical analysis. This investigation conformed with the Guide for the Care and Use of Laboratory Animals published by the US National Institutes of Health (NIH Publication No. 85-23, revised 1996) and all animal studies were approved by Emory University Institutional Animal Care and Use Committee (Animal Welfare Assurance #A3180-01).

Echocardiography

Anesthetized rats were subjected to echocardiography at 7 and 21 days following IR surgery. Short axis values of left ventricular end systolic (ES) and end diastolic (ED) dimension were obtained using Acuson Sequoia 512 echocardiography workstation with 14 MHz transducer. An average of 3 consecutive cardiac cycles was used for each measurement and was performed three times in an investigator-blinded manner.

Fractional shortening was calculated as (end-diastolic diameter – end-systolic diameter)/end-diastolic diameter and expressed as a percentage.

Invasive Hemodynamics

Following echocardiography at 21 days, animals were subjected to invasive hemodynamic measurements using a Millar MPVS Pressure-Volume system and Power Lab software package. Following intubation, a 2-French catheter was inserted into the right jugular vein and advanced to the right ventricle for pressure measurements. After the catheter was removed from the right ventricle, a polyethylene catheter was inserted into the right jugular vein for the subsequent saline volume challenge. The pressure-volume catheter was then inserted into the right carotid artery and advanced to the left ventricle. After stabilization, baseline left ventricular pressure-volume loops were recorded. To change preload, the inferior vena cava was transiently compressed (<30 seconds) through an incision in the upper abdomen. Pressure-volume measurements were recorded for at least 10 cardiac cycles and data averaged to get mean values for each animal. Data extracted include +dP/dT, -dP/dT, left-ventricular end systolic and diastolic pressure and volume.

Immunohistochemistry

Paraffin-embedded tissue was sectioned in to 5 mm sections and adhered to a glass slide. Following rehydration, tissue sections were probed with FITC-labeled isolectin B4 (Molecular Probes) and imaged using fluorescence microscopy. Additionally, tissue sections were probed against c-kit using a commercially available antibody (Santa Cruz H-300) and a fluorescently labeled secondary antibody (Molecular Probes). To quantify

immunohistochemistry, 5 non-serial sections from each animal were analyzed by a blinded investigator and expressed as either vessels/mm2 (for isolectin) or cells/mm2 (for c-kit).

Collagen deposition was determined by picrosirius red (Sigma) staining as previously described [19]. Briefly, 5 µm tissue sections were stained with Sirius Red and imaged at 2.5× using a light microscope. Overlapping images were taken and then stitched together using Adobe Photoshop to generate an image of the entire heart. Total collagen area (red staining) was normalized to total left ventricular area in 3 separate sections per animal using ImageJ.

Migration assay of CPCs into hydrogel

Cardiac progenitor cells (CPCs) were isolated from adult rat hearts as described using anti-c-kit coated magnetic beads prior to clonal expansion [248]. The CPCs were characterized for expression of c-kit and only clones with >90% expression of c-kit and >80% expression of the cardiac transcription factors nkx2-5 and gata-4 were used in this study. CPCs were trypsinized and incubated with 5-chloromethylfluorescein diacetate (CMFDA; Molecular Probes) for 30 minutes at 37°C. Four percent PEG hydrogels of 50 µL size containing 10 ng of VEGF, HGF or VEGF+HGF were generated as described above. The gels were laid flat into 8 well Labtek chamber slides with glass bottom (Nunc) for ease of imaging. The hydrogels were swollen in 100 µL PBS with Penicillin/Streptomycin for one hour at which point they completely covered the bottom of the well. CMFDA labeled CPCs (50,000) were seeded on top of the flat hydrogel surface. After 48 hours, the extent of CPC migration into the hydrogel was visualized on

a Nikon-C1 laser scanning confocal microscope with a 20× air objective. Five z-stack projections through a 90–450 μm thick section of the swollen hydrogel were rendered. The thickness of the imaged section was determined by the minimal thickness required to observe maximum cellular migration to reduce image capture and processing time. The maximum distance migrated by the cells into the hydrogel was calculated using ImageJ.

Statistics

All statistical analyses were performed using Graphpad Prism 5 software as described in the figure legends. P values of less than 0.05 were considered significant.

Results

Growth factor release from hydrogels is controlled by enzyme-mediated degradation

Bioactive hydrogels were synthesized as depicted in Figure 244A. To determine release of VEGF (Figure 24B) and HGF (Figure 24C) in vitro, fluorescently-labeled growth factors were chemically incorporated into PEG-MAL hydrogels. Modification of growth factors by PEG-MAL was verified by molecular weight increases of the protein band on SDS-PAGE. Hydrogels subjected to higher collagenase treatment were observed to degrade within the first 48 hours after treatment while hydrogels in PBS remained intact. Samples incubated with increasing levels of collagenase released loaded growth factor rapidly coinciding with gel degradation. PBS treated samples released protein much more slowly. These results show the rate of release of growth factors is dependent upon protease-mediated degradation of the hydrogel due to the protease-degradable crosslinking peptides.

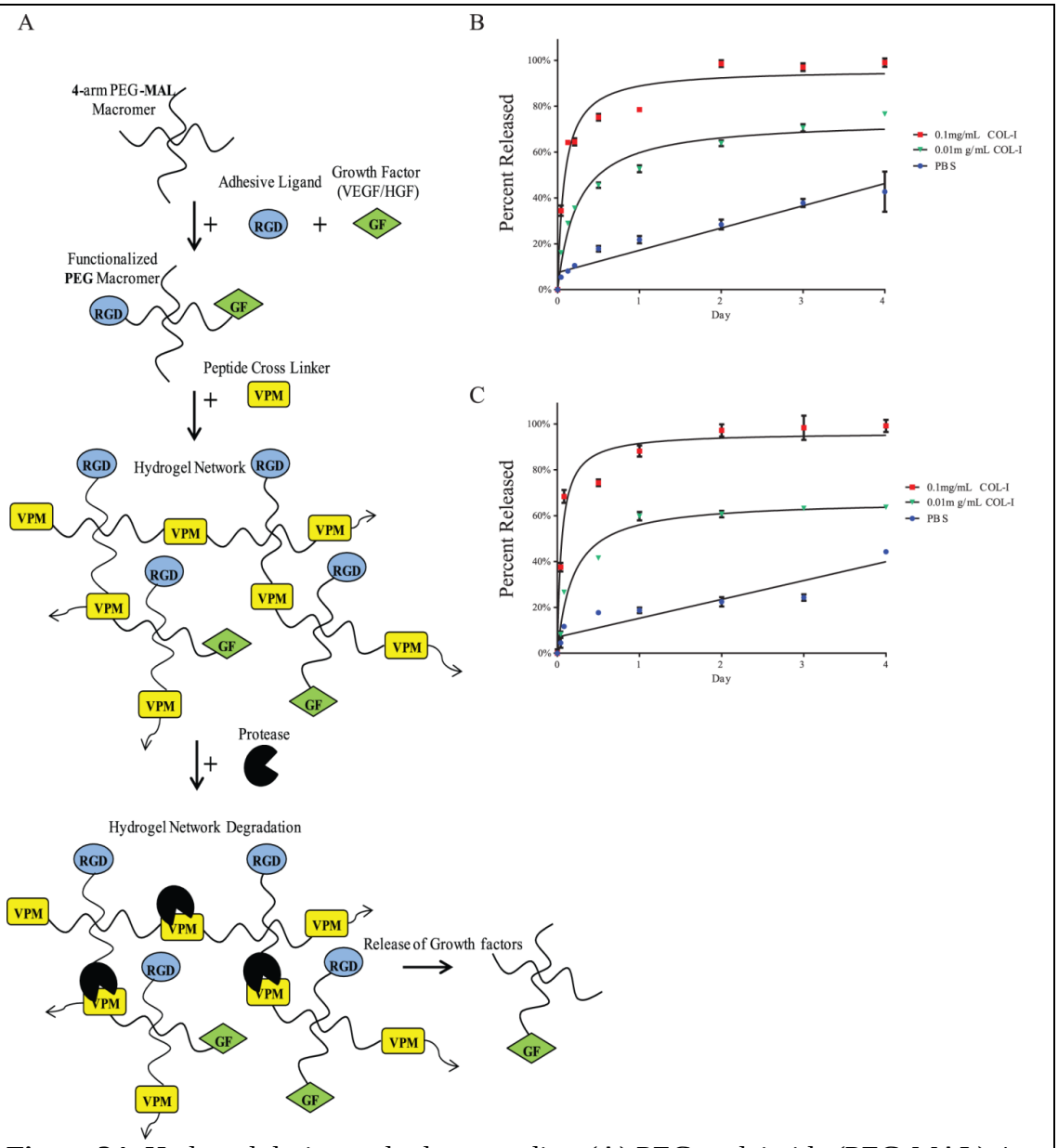

Figure 24: Hydrogel design and release studies. (A) PEG-maleimide (PEG-MAL) 4-arm macromers were pre-functionalized with RGD adhesion peptide and growth factors HGF and/or VEGF. The precursor molecules were cross-linked into a hydrogel by addition of cysteine-flanked protease-degradable peptide sequence GCRDVPMSMRGGDRCG (VPM). (B) Fluorescently tagged VEGF and (C) HGF released from PEG-MAL hydrogel treated with either PBS or 2 doses of collagenase Type 1 as measured by fluorescent plate reader sampling of incubation media. One hundred percent of loaded VEGF and HGF were released by day four after collagenase treatment while lower doses of collagenase and PBS released up to 65% and 40%, respectively. Data are mean ± SEM from 6 samples per condition. Hyperbolic and linear curve fits indicate different release profiles behaviors for collagenase vs. PBS treatment.

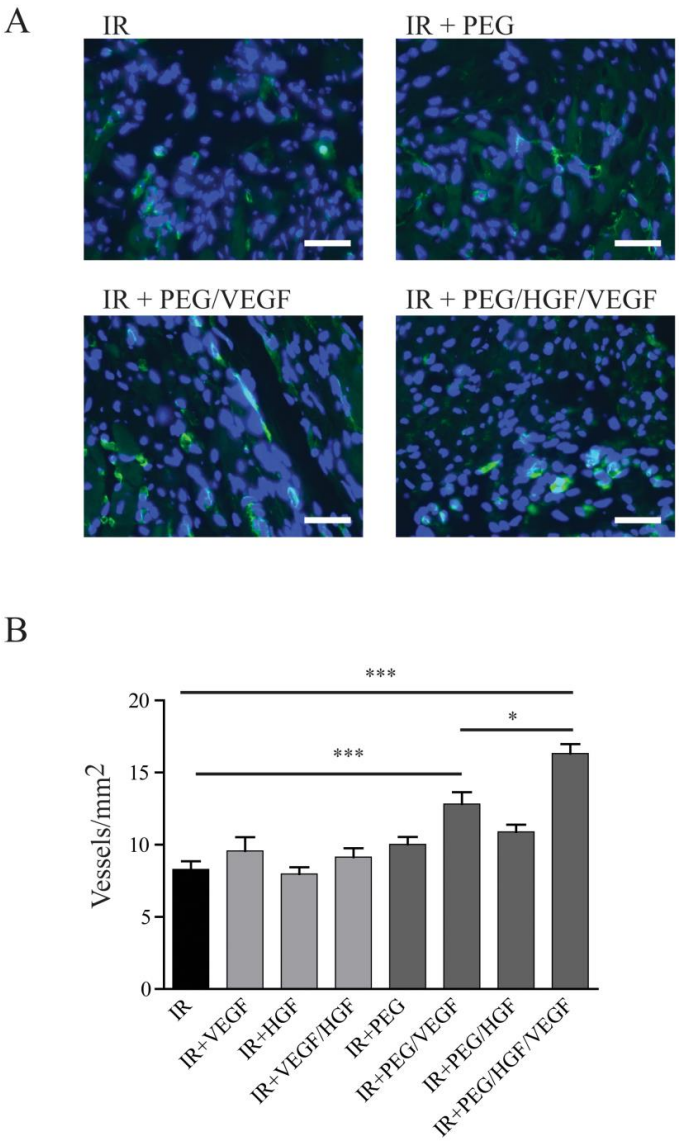

Figure 25: Angiogenesis following ischemia-reperfusion in treated rats. At 21 days following infarction, vessels were quantified by staining with isolectin-b4 conjugated to FITC. (A) Representative images (green = isolectin; blue = DAPI; scale bar = 30 μm) of rats subjected to IR, IR + PEG, IR+PEG/VEGF, or IR + PEG/HGF/VEGF. (B) Grouped data (mean ± SEM; n≥7 per group) demonstrating a significant increase in vessels/mm2 in the PEG/VEGF rats compared with IR alone, and in the PEG/HGF/VEGF rats compared with either PEG/VEGF or IR alone (***$p<0.001$; *$p<0.05$; ANOVA followed by Student-Newman-Keuls post-test). PEG = polyethyleneglycol, VEGF = vascular endothelial growth factor, HGF = hepatocyte growth factor, IR = ischemia reperfusion.

Angiogenesis is improved with the dual delivery of growth factors released from PEG hydrogels

Rats were subjected to ischemia-reperfusion (IR) surgery and free growth factors or growth factors embedded in protease-degradable hydrogels were injected in to the borderzones. To determine levels of angiogenesis, sections were probed with a FITC-labeled isolectin conjugate and vessels were counted 21 days following infarction. In untreated animals, 8.3±0.5 vessels/mm2 were counted in the infarcted area (Figure 25A top left). Infarcts treated with free VEGF, PEG hydrogel alone, or HGF-loaded PEG hydrogels (PEG/HGF) had equivalent levels of angiogenesis as the untreated control. Treatment of animals with VEGF-loaded PEG hydrogels (PEG/VEGF) significantly increased vessel density in the infarct area (12.8±0.8 vessels/mm2; $p<0.01$ vs. IR alone; Figure 25A bottom left). Interestingly, PEG hydrogels loaded with VEGF and HGF (PEG/VEGF+HGF) further increased vessel density over PEG/VEGF (16.3±0.6 vessels/mm2; $p<0.05$ vs. PEG/VEGF, $p<0.001$ vs. IR alone; Figure 25A bottom right). These grouped data (Figure 25B) demonstrate that PEG/VEGF is able to induce significant angiogenesis following MI, and that the presence of HGF along with VEGF induces a synergistic response.

Fibrosis is reduced with the dual delivery of growth factors released from PEG hydrogels

To determine levels of fibrosis following MI, tissue sections were stained with picrosirius red 21 days following IR and fibrotic area was normalized to total LV area. Animals receiving no treatment had a fibrotic area of 41.5±3.3% of total LV area (Figure 26A left). There was no significant decrease in groups treated with free growth factors or empty hydrogel. Only PEG/VEGF+HGF-treated animals demonstrated a significant

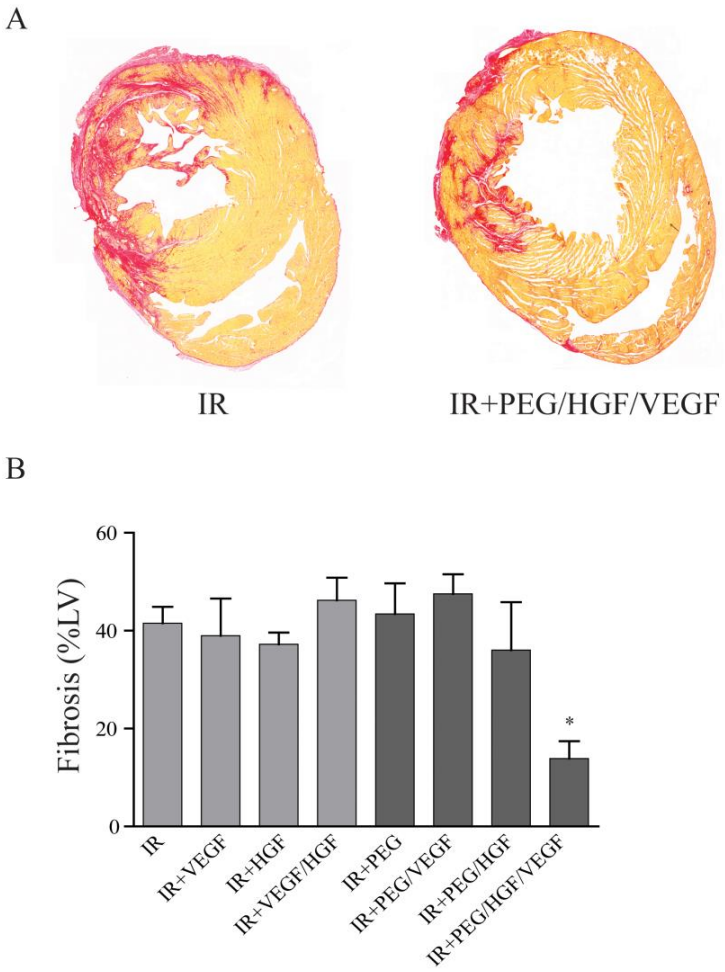

Figure 26: Fibrosis following ischemia-reperfusion in treated rats. At 21 days following infarction, fibrosis was measured by staining for collagen using picrosirius red (red stain, images taken at 20× magnification). (A) Shows 2 representative stitched heart sections used for quantification (IR alone and IR + PEG/VEGF/HGF. (B) Grouped data (mean ± SEM; n≥7 per group) demonstrating a significant decrease in fibrotic area in PEG/HGF/VEGF rats compared with IR alone (*p<0.05; ANOVA followed by Student-Newman-Keuls post-test). PEG = polyethyleneglycol, VEGF = vascular endothelial growth factor, HGF = hepatocyte growth factor, IR = ischemia reperfusion, LV = left ventricle.

decrease in fibrosis compared with IR alone (13.9±3.5%; p<0.05; Figure 26A right). The grouped data in Figure 26B clearly demonstrates that only controlled release of both growth factors from the PEG hydrogel inhibited collagen deposition following IR.

Progenitor cell isolation and migration is increased with the dual delivery of growth factors released from PEG hydrogels

To determine the effect of growth factor treatment on progenitor cell migration, in vitro migration assays were performed in addition to in vivo staining of progenitor cells. As shown in the representative images and grouped data in Figure 27A, c-kit+ cardiac progenitor cells demonstrated significant increases in migration in response to both HGF and VEGF in vitro. Examination of migration in to the hydrogel showed a significant increase in VEGF-loaded hydrogels, but not HGF-loaded hydrogels ($p<0.001$ VEGF vs. PEG alone; $p<0.05$ vs. HGF). There was a further increase in migration in to hydrogels loaded with both growth factors ($p<0.0001$ vs. VEGF, HGF, and PEG alone). Additionally, a similar trend was seen in migration in a 2-dimensional transwell system (data not shown). To determine levels of progenitor cells *in* vivo, sections were stained with an anti-c-kit antibody and positive cells were counted in relation to total cells. While all other treatments were similar to IR alone, there was a significant increase ($p<0.001$) in c-kit+ cells in animals treated with PEG/VEGF+HGF (IR = 3.1 c-kit+/1000 nuclei, PEG/VEGF+HGF = 10.6 c-kit+/1000 nuclei; Figure 27B&C)

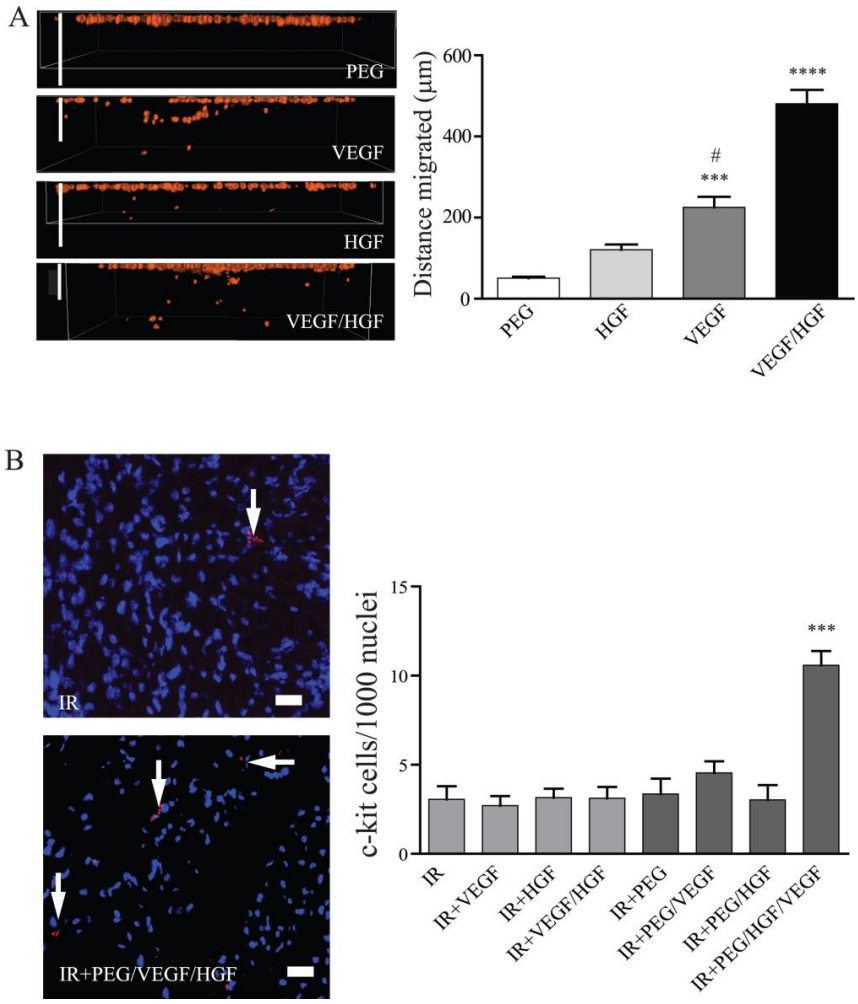

Figure 27: Progenitor cell recruitment. (A) Isolated, fluorescently-tagged cardiac progenitor cells (CPCs) were seeded on top of hydrogels containing nothing, VEGF, HGF, or HGF/VEGF and allowed to migrate for 48 hours. Gels were turned sideways and imaged using confocal microscopy and distance migrated was determined using ImageJ (scale bar = 100 μm). Data are mean ± SEM from 5 separate experiments and demonstrate a non-significant increase in migration in to HGF-loaded gels, but a significant increase in migration in to VEGF-loaded gels (***$p<0.001$ compared to PEG alone, #$p<0.05$ compared to HGF). There was a further increase in migration between the single treatment groups and HGF/VEGF (****$p<0.0001$ vs. all groups; ANOVA followed by Student-Newman-Keuls post-test). (B) Representative images of c-kit staining (red) in the infarct zone of rats with IR alone or treated with PEG/HGF/VEGF (blue = DAPI; scale bar = 30 μm). Grouped data (mean ± SEM; $n\geq7$ per group) demonstrating a significant increase in c-kit+ cells in PEG/HGF/VEGF treated rats compared with IR alone (***$p<0.001$; ANOVA followed by Student-Newman-Keuls post-test). PEG = polyethyleneglycol, VEGF = vascular endothelial growth factor, HGF = hepatocyte growth factor, IR = ischemia reperfusion, RFU = relative fluorescent units**.**

Echocardiographic function assessment shows improvement with growth factor delivery

To determine the effects of the various treatments on cardiac function, echocardiography was performed at 7 and 21 days following infarction. Data were obtained from short-axis images, quantified, and presented in Figure 28A&B, respectively. At day 7, there was a significant decrease in function in IR animals ($p<0.001$). Of all the treatment groups, only empty PEG hydrogels significantly improved function 7 days following IR ($p<0.05$ vs. IR alone). In contrast, 21 days following IR, empty PEG hydrogels were no different from IR alone. Interestingly, only PEG/VEGF+HGF-treated animals demonstrated a significant improvement in function ($p<0.05$ vs. IR alone). These data show that long-term improvements in function were only evident following combined growth factor delivery from PEG hydrogels.

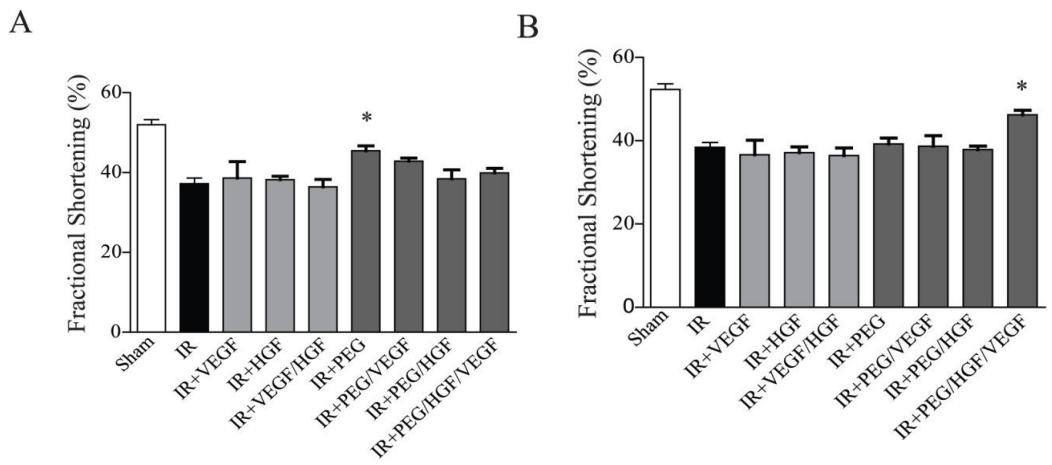

Figure 28: Echocardiographic measurement of function. Grouped data (mean ± SEM; n≥7 per group) from (A) 7 days post-injury or (B) 21 days post-injury. At 7 days there was a significant increase in function only in the empty PEG hydrogel treated rats. At 21 days, only the PEG/HGF/VEGF rats demonstrated a significant increase in function compared with untreated rats (*$p<0.05$; ANOVA followed by Student-Newman-Keuls post-test). PEG = polyethyleneglycol, VEGF = vascular endothelial growth factor, HGF = hepatocyte growth factor, IR = ischemia reperfusion.

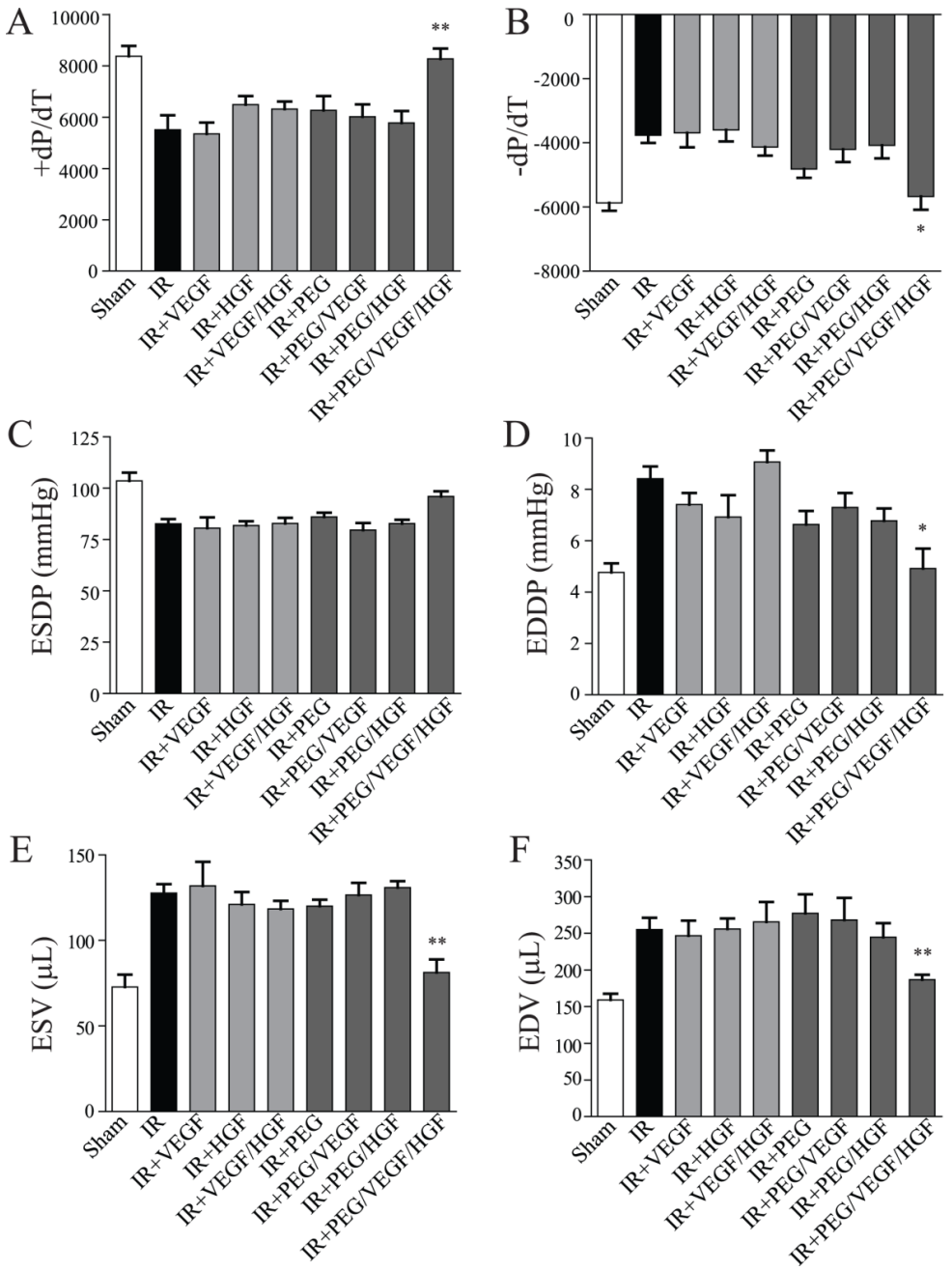

Figure 29: Invasive hemodynamic measurement of function. Grouped data (mean ± SEM; n≥7 per group) taken 21 days following injury by cardiac catheterization. (A-F) Various measures of function demonstrate a significant improvement in all but 1 measurement (C, end-systolic developed pressure) in PEG/HGF/VEGF treated rats compared to IR alone (*p<0.05; **p<0.01; ANOVA followed by Student-Newman-Keuls post-test). PEG = polyethyleneglycol, VEGF = vascular endothelial growth factor, HGF = hepatocyte growth factor, IR = ischemia reperfusion, ESDP = end-systolic developed pressure, EDDP = end-diastolic developed pressure, ESV = end-systolic volume, EDV = end-diastolic volume, ±dP/dT = change in pressure over time.

Invasive Hemodynamics confirms improved cardiac function from dual delivery of growth factors

To confirm echocardiographic assessments, invasive hemodynamics was performed to determine actual cardiac pressures and volumes 21 days following IR and summarized in Figure 29. Infarction induced a significant impairment in both positive and negative pressure changes over time (dP/dT; $p<0.01$ vs. sham). Of all the treatments, only PEG/VEGF+HGF-treated animals had significantly improved pressure changes ($p<0.01$ for +dP/dT, $p<0.05$ for –dP/dT vs. IR alone). In addition to pressure changes, significant improvements in left-ventricular end diastolic pressure ($p<0.01$) and both end systolic ($p<0.05$) and end diastolic volumes ($p<0.01$) were seen in PEG/VEGF+HGF-treated animals. Whereas there was a 20% improvement in left-ventricular end systolic pressure, it was not considered significantly different. Taken together, these data confirm echocardiographic measurements of cardiac function, demonstrating a significant improvement in cardiac function in animals receiving both growth factors delivered from a protease-degradable PEG hydrogel.

Discussion

Ischemia-reperfusion injury (IR) results in excessive local cell death, and in many patients eventually leads to heart failure as the lost tissue is not replaced. While current treatments such as ß-receptor antagonists and angiotensin receptor blockers are effective in improving contractility, there are few therapies that attempt to address the underlying mechanistic problems [234, 249]. While growth factor therapy holds great promise, the retention in the highly vascular myocardium is low and prevents sustained activation

needed for adequate cellular responses [218]. Biomaterial-based approaches for sustained therapeutic delivery hold great promise as many have shown little toxicity in animal studies, and they can be tailored in many cases to address tissue needs.

In this report, we delivered a protease-degradable, bioactive PEG hydrogel loaded with VEGF and HGF to the infarct zone following IR for localized therapy. This material was chosen due to the low fouling properties of PEG, as well as excellent biocompatibility [80]. A recent publication with this novel material containing both RGD sequences to enhance cell adhesion, as well a dithiol protease-cleavable peptide cross-linker GCRDVPMSMRGGDRCG, demonstrate excellent cell compatibility as well as the ability to form *in situ* gels on tissue [12]. Timing of gel formation can be tuned by modifying the concentration of the buffering agent triethanolamine (TEA) in the reaction solution and thus proteins can be freshly added immediately prior to injection. The injected material is a liquid, yet gels rapidly in tissue. We examined VEGF and HGF release *in vitro* and show the hydrogel system is capable of controlled release due to protease-mediated degradation.

Preliminary studies demonstrated excellent *in situ* gel formation in the myocardium, similar to other hydrogels used for post-infarct drug delivery. In vitro release studies demonstrated a slow release profile in PBS that was accelerated by increasing levels of collagenase treatment. Given the amount of MMPs released following IR, especially collagenase [250], this on-demand release system is ideal for the post-infarcted heart, triggering release of growth factors when active remodeling is occurring. Interestingly, when function was measured at 7 days, only the empty hydrogel demonstrated a

significant increase in function. While it is possible that the bioactive sequences aided in some manner, they are within the hydrogel and likely not diffusing away to enhance cellular function. Previous studies demonstrate that hydrogels themselves can acutely improve function due to mechanical support of the left ventricular (LV) wall [173, 174]. The bioactive PEG hydrogel has an elastic modulus of 0.5–1.0 kPa [12], within the range of most soft tissues and well below stiff substrates such as collagen that impede cardiac function [251-253]. While there was no effect of embedded growth factors at this early time point, it was not surprising as neither HGF nor VEGF plays a major role in cardiomyocyte survival, the major contributor of early regulation of cardiac function [238]. It is also possible that the growth factors were not released fast enough to diffuse to the injured cardiac tissue, although our in vitro results would suggest otherwise. In contrast to the day 7 data, at day 21 there was a significant improvement in cardiac function only in the group that received the bioactive hydrogel embedded with VEGF and HGF. In keeping with the acute studies, there was no effect of free growth factors, or single growth factor hydrogel treatments. This was determined both via 2D echocardiography and invasive hemodynamic measurements. Dual growth factor delivery from the bioactive hydrogel resulted in a significant decrease in end-systolic and diastolic volume, as well as improved contractile performance as evidenced by improvements in end-systolic and diastolic pressures.

To determine potential mechanisms for these enhancements, several areas were examined. Due to the documented effect of VEGF on angiogenesis [254], vessel number was assessed in the infarcted tissue. Consistent with previous findings, sustained VEGF delivery induced a significant increase in vessel number with no effect for free VEGF.

Despite this increase in vessel number, this effect did not translate to increases in function. These data are supported by prior studies noting that angiogenesis alone may not be sufficient for long-term functional recovery [245, 255]. We saw no evidence of increased angiogenesis from HGF-loaded hydrogels, despite recent studies demonstrating the ability of HGF to induce angiogenesis following injury [256-259]. Interestingly, the majority of these reports are using HGF gene therapy or various HGF-overexpressing cells [260, 261], suggesting perhaps long-term release of HGF is required for improved angiogenesis. However, long-term HGF production may have negative side-effects, and recent efforts have focused on using HGF gene expression that can be turned off via suicide gene system, indicating the need for temporal control of HGF release [262]. While our HGF release was not sustained enough to induce angiogenesis on its own, co-delivery of HGF with VEGF had a synergistic effect, significantly increasing angiogenesis over single hydrogel-growth factor delivery alone. This strategy of dual growth factor delivery has been used recently to co-deliver insulin-like growth factor-1 (IGF-1) with HGF to improve angiogenesis [217]. Additionally, both VEGF and IGF were identified as being potential mediators of the paracrine effects of stem cell therapy, specifically for improving angiogenesis [263-265]. Recent studies demonstrate that hydrogel-mediated co-delivery of VEGF and platelet-derived growth factor (PDGF) for angiogenesis is synergistic as compared with single growth factor therapy[266, 267]. Finally, both VEGF and HGF have been delivered synergistically using poly(lactic-co-glycolic) acid (PLGA) microspheres [268]. The authors made microspheres up to 100 μm in diameter and implanted them in the leg muscle of mice subjected to hindlimb ischemia. This interesting study found that dual factor-loaded microparticles themselves

enhanced angiogenesis, but the main finding was that dual-delivery of HGF and VEGF enhanced endothelial progenitor cell-induced function and recovery compared to cells alone. While this is interesting in that it may be a future avenue to use our PEG hydrogel to deliver cells, previous reports from our laboratory demonstrate that PLGA microspheres are not optimal for post-infarction delivery due to uncontrolled release and potential to induce inflammation from acidic degradation products [269]. Taken together, our data clearly show that dual growth factor release from a bioactive hydrogel is superior to single factor release for improving angiogenesis, but that other combinations may also be effective and remains an area for potential future study.

Similar to angiogenesis, we also examined collagen content via picrosirius red staining and found the dual growth factor delivery to be significantly improved over single factor hydrogel-mediated or soluble growth factor delivery. The effect of VEGF on fibrosis is not clear, with many studies linking the ability of VEGF to reduce fibrosis on its ability to increase angiogenesis [270, 271]. While angiogenesis and fibrosis are clearly tied, there is potential for altered signaling in myocytes independent of angiogenesis. An early study demonstrated increased Akt-mediated signaling in animals treated with chronic HGF following infarction [272]. While Akt is well known for its role in cell survival, many studies link activation of Akt to decreases in collagen production and assembly, especially in fibroblasts [273]. While we cannot separate the specific cell signaling effects from the benefits of increased angiogenesis, it is worth noting that hydrogel-mediated VEGF delivery did not result in a decrease in fibrosis, indicating angiogenesis by itself may not be sufficient. Likewise, another explanation is that VEGF did not induce enough angiogenesis to improve fibrosis. We also examined progenitor

cell infiltration by immunohistochemistry and found increased cell numbers only in the dual growth factor hydrogel group. Both VEGF [274] and HGF [275] are implicated in migration of c-kit+cardiac progenitor cells (CPCs). Our in vitro data confirms that CPCs show increased migration in response to the synergistic combination of VEGF and HGF over single growth factor alone. Studies demonstrate that CPCs respond to gradients in growth factor concentrations in vivo, and the use of a biodegradable hydrogel may facilitate this. Additionally, the hydrogel used in this study also contains RGD ligands, which may facilitate CPC retention or binding [276]. It is also possible that increased angiogenesis allowed for better access for circulating and bone marrow-derived progenitors expressing c-kit. We do not know the source of c-kit+ cells in this study and could be an interesting area for future investigation. Finally, VEGF and HGF may also improve the survival and growth of migrated progenitor cells. While we did not see co-staining of c-kit with any vessels in our samples, it may be that c-kit expression was lost as the cells matured. Earlier studies demonstrated that bone-marrow-derived c-kit+ clusters had improved cardiac differentiation potential in vitro [277]. While we examined the slides for evidence of clusters in vivo, we were unable to detect any within the infarcted tissue. As the source of these cells was not determined in our studies, the role of cell clustering in the healing response seen is unknown, but remains an interesting area for future studies.

Our data clearly demonstrates the ability of a bioactive, degradable hydrogel to deliver growth factors in vivo. There are very few reports of PEG hydrogels used to improve post-MI remodeling and angiogenesis [278, 279]. The use of a hydrogel containing adhesive sequences, as well as degradable linkages is promising, as it allows for potential

control over spatial and temporal aspects of healing and regeneration [12]. PEG hydrogels are promising in that they can be modified chemically, they have excellent biocompatibility, and do not bind proteins on their own. Thus, most parameters of drug delivery can be easily controlled. The processes following MI that contribute to the disease, inflammation, cell death, fibrosis, hypertrophy, all follow distinct time courses with varying locations [238]. Thus, it is unlikely that one factor will be optimal for all these events and multiple signals are needed. Our data demonstrate that dual growth factor delivery, sustained with bioactive PEG hydrogels is significantly better than free growth factors, or single-growth factor delivery attempts. While this seems rather intuitive, very few reports exist of dual growth factor delivery with biomaterials for MI. Thus the potential for creating even more complex delivery systems with control over growth factor release, cell migration, and scaffold degradation is quite promising

Conclusion

In this study, we demonstrated the first in vivo use of a recently described bioactive, protease-degradable PEG hydrogel capable of delivering multiple growth factors. The hydrogel was delivered via intramyocardial injection following infarction, and loaded either with VEGF, HGF, or both factors. Only the hydrogels loaded with both factors demonstrated functional improvements, with animals showing increased cardiac function by invasive hemodynamics and echocardiography. Our data demonstrated that dual growth factor release, specifically controlled release of both HGF and VEGF was far superior to single-factor delivery at inducing angiogenesis, inhibiting fibrosis, and

stimulating migration of progenitor cells. These results may have clinical implications in the prevention of post-MI cardiac dysfunction and demonstrate the utility of synergistic, biomaterial-based growth factor delivery.

APPENDIX B

SUPPLEMENTAL DATA

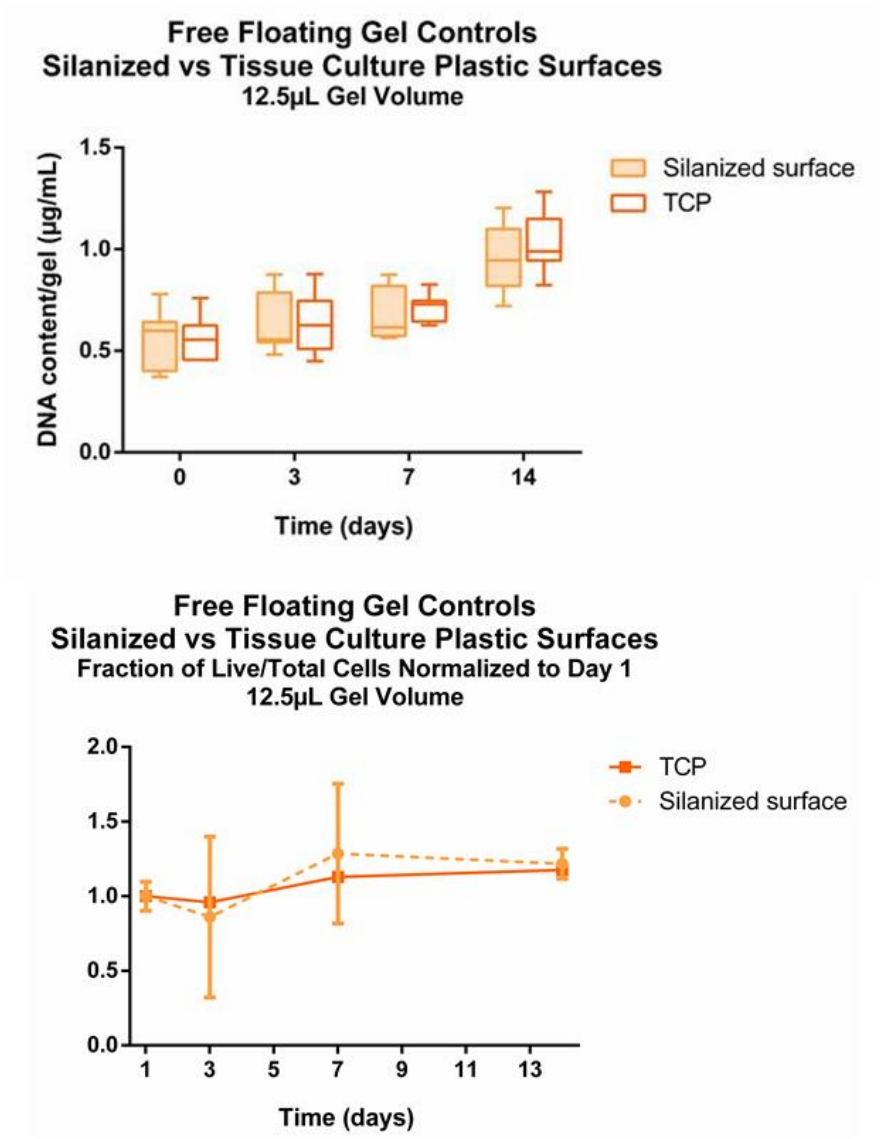

Figure 30: DNA content comparison shows no significant differences between free-floating hydrogels cast on parafilm and cultured in TCP ('TCP') or cast and cultured on silanized PDMS surfaces for use as geometric controls: free-floating, bulk hydrogels.

1. <u>Free floating vs silanized surfaces comparison</u>

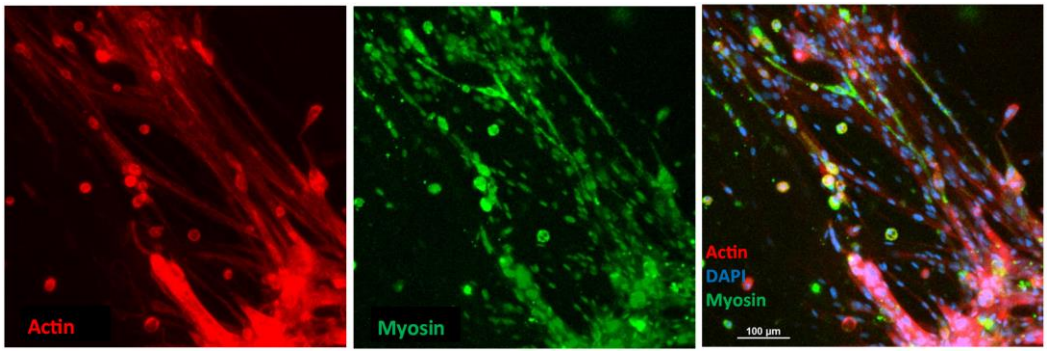

Figure 31: Local correlation of actin (Ph 555) staining with sarcomeric myosin (MF20, Alexa Fluor 488) to show that the differentiating cell alignment can be measured using the less diffuse actin staining for better agreement with existing image processing capabilities to determine alignment index measurements.

Local correlation of actin (Ph 555) staining with sarcomeric myosin (MF20, Alexa Fluor 488)

2. Diffusion distances for agonists of contraction

For the external agonists: Acetylcholine (ACh) and Caffeine, diffusion time through a construct is inversely proportional to distance and directly related to a diffusion constant. Using Einstein's approximation equation $t \approx \frac{x^2}{2D}$, where the diffusion time (t) is a function of the distance of diffusion (x) and the diffusion coefficient (D). Diffusion time increases with the square of diffusion distance. As shown in Table 6, diffusion times for molecules of this size are in the nanosecond range, allowing us to assume that millisecond scale changes in readings are related to cellular structure contraction, and not molecular diffusion.

Table 8: Diffusion times for agonists: ACh and Caffeine

Agonist	Diffusion Coefficient (cm^2/s) in H_20 at 25°C	Min. Diffusion Distance (mm)	Max. Diffusion Distance (mm)	Time range (ns)
ACh	4.06×10^{-6}	2.0	5.0	81.1 – 507.2
Caffeine	5.39×10^{-6}	2.0	5.0	107.8 – 673.7

APPENDIX C

AMENDMENTS & CLARIFICATIONS

Clarification of influence of toroid shape on cellular alignment: hypotheses and discussion

We would like to clarify the manner in which alignment occurs, by correlating two key metrics: the change over time of the volume of the toroidal hydrogel and the alignment of cellular structures within the toroidal hydrogel. We agree this data and discussion portion was missing from the document.

1. Quantification in the reduction in outer diameter over time

We observed that the factors affecting alignment within the hydrogel are a combination of interdependent factors. While passive cellular alignment may occur as a consequence of the construct deformation, notable construct deformation itself occurred due to cellular forces acting within the hydrogel in the first place. Quantification of one of the factors affecting alignment: change in hydrogel diameter over time, is shown in Figure 32. Hydrogels without cells cast around toroids do not significantly change after swelled volume (day 1) over 14 days. Hydrogels containing cells contract significantly from their volume at day 1 to day 14. The cell density in both hydrogel volumes is the same, yet, different rates of contraction are observed. This leads us to consider other factors that affect rate of contraction such as the development of differing stress patterns due to geometrical variation and differences in cellular contribution.

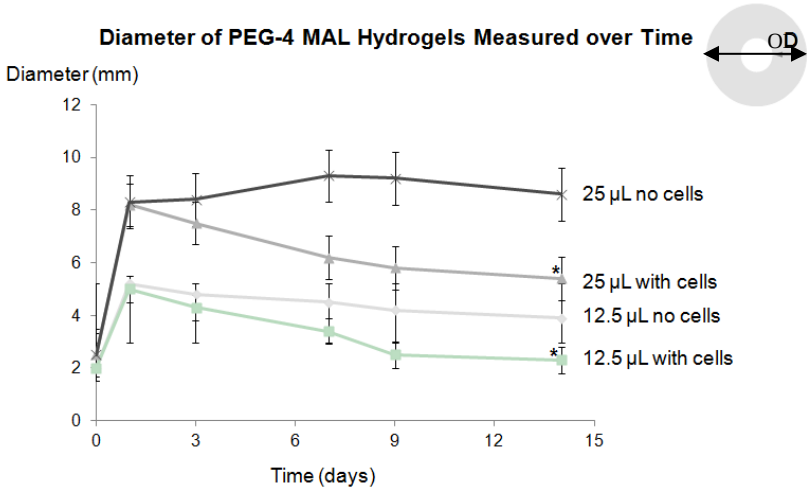

Figure 32: Change of spire -toroid outer diameter 'D', over time when cast around 1.0 mm spires and cultured for 14 days, with and without cells. OD was measured in cardinal directions and averaged for each spire-toroid. All gels swell overnight between casting (day 0) and day 1. After day 1, for a given volume, the presence of cells significantly decreases the diameter as cells spread and grow, contracting the hydrogel. (* indicates significance $p < 0.05$ between gels with or without cells, of a given volume, at day 14, $n = 5$).

We agree that our "constructs are constrained such that essentially all of the shape change over time occurs by reduction of the outer diameter of the toroid." This was visually observed.

2. Estimation of diameter-change effect on embedded fiber orientation and comparison with observed development of alignment

Overlaying the development of AI over time, Figure 21, with Figure 1 above, can provide an understanding of how the two are related. Figure 21 shows steep increases in alignment between days 1 and 3 and between 3 and 7. Alignment continues to increase at a slower rate between days 7 and 14. In Figure 1, we observe toroidal hydrogels with cells begin to contract between days 1 and 3 and then continue to contract at a high rate from days 3, 7, through to 9. Beyond day 9, the toroid diameter decreases much less

rapidly. These data suggest that the development of alignment occurs between days 1 through 7, during the phase of highest toroid contraction.

3. Demonstration of stress development in Hydrogels

We have shown that contraction is mediated by cells within the hydrogel, and expect this contraction to be a result of cell-mediated traction forces [280, 281] . The extent of the traction forces developed that cause the macro-scale construct deformation may be related to differential stress patterns within toroidal hydrogels. These differences in stress patterns occur as a result of the geometry, but are in interplay with the cellular forces themselves. We believed it to be beyond the scope of this thesis to dissociate these interactive factors (cellular, physical, mechanical), their causes, spatio-temporal occurrence and determine their precise interdependence for the assessment of alignment development.

The use of Figure 23 is to demonstrate that there exist differences in stress patterns that cause deformation, and present one possible effect that may explain the development of alignment. The model assumes that the toroid structure has consistent density. Similarly, a toroid with homogenous cell density, where each cell exerts the same contraction force would produce the same relative stress patterns in a toroid configuration. We do not agree that "it is not the stress…[that] influences alignment, but the deformation of the construct in response to that stress", as these factors are interdependent and stress development may be occurring in parallel with alignment development.

We do agree that the change in hydrogel contraction causes "fibers (even inactive, non-biological fibers) that were randomly embedded in the initial configuration to become circumferentially aligned...as a natural consequence of uniform tension developed by those initially randomly oriented cells interacting with the geometrical constraints on deformation." As the myotubes develop within the hydrogel, we expect they would produce biological ECM fibers of their own, further contributing to the simultaneous stress and alignment development.

Though the cells will contribute to their alignment, we agree that it is "qualitatively different for the cells to change the geometry of their environment and pull themselves into alignment than for the cells to rearrange themselves within a fixed construct." In this toroid cell-hydrogel system, we observed that the cells contribute to the changing environment of their construct, resulting in a construct with stable geometry by day 7, within which they continue to align. We understand the construct to be 'fixed' around the central spire, but constantly changing as remodeled by the developing cells contained within it.

4. Surface Area/Volume ratio measurements

Committee members raised valid concerns regarding the accurate measurement of the hydrogel and construct dimensions for Surface Area/Volume (SA/V) ratios and understanding their consequent importance in alignment of the cells within the hydrogels.

To further clarify the note on cell density: there are no differences in cell density between hydrogel configurations and the differing volumes over time arise as a function of geometry during swelling and inter-dependent cell-mediated contraction and alignment of the myoblasts and myotubes. Past work with the hydrogel system has shown that swelling can be constrained (cast between tow cover-slips, in troughs) and is dependent upon the geometry in which the hydrogels are cast.

SA/V ratio is believed to be important to quantify our visual observations. We agree that it is not the best singular metric to determine a pre-requisite for alignment. Further, this claim would warrant deeper investigation into specific ratios. Hence, we would like to clarify the purpose of the SA/V ratio as a suggestion for the geometrical constraints that may enable alignment support. Though optimal for the scenarios studied here, developing other constructs would have to take into consideration scale of the hydrogels, cell density, swelling constraints, and other practical measures of construct generation. It cannot be concluded that "a 1 liter construct with a surface-volume ratio of 1.4" would generate a construct with optimized cell alignment.

5. Dimensions used for AI analysis

We agree that the dimensions used for AI measurements are missing in the document. Referencing Figure 15, page 75: full images were taken at 20 x magnifications where the field of view is approximately (600x600) μm^2, 360000 μm^2. These images were cropped to about 60 μm^2, resulting in 6-8 images of 60000 – 45000 μm^2 per original image for

analysis. The images needed to be cropped in this manner to avoid empty 'black-space' skewing the FFT and ensure more consistent image analysis with the code being used.

Contractility Experiments

Acknowledgement of lack of comparability to Yamamoto (2011)

We acknowledge that the time to peak tension of 5-10 seconds, for total contraction duration of 20-30 seconds cannot be practically compared with the work by Yamamoto et al for the primary reason of the utilization of different modes to produce contraction: namely, electrical pulse stimulation compared to the diffusion of small molecules seen in this work. We compared our work with Yamamoto's due to the limited work in small molecule diffusion for millimeter-scale muscle constructs developed from mouse stem cells.

REFERENCES

1. Tanner, C.L., J.R. Cruz, and R.D. Braun, *Structural Verification and Modeling of a Tension Cone Inflatable Aerodynamic Decelerator*. 2010, Georgia Inst. of Tech.
2. Powers, S.K. and E.T. Howley, *Skeletal Muscle Structure and Function*, in *Excercise Physiology: Theory and Application to Fitness and Performance* 2009, McGraw-Hill Companies.
3. Stone, M.H., M. Stone, and W.A. Sands, *Neuromuscular Physiology* in *Principles and Practice of Resistance Training*. 2007. p. 384.
4. Grassi, F., S. Fucile, and F. Eusebi, *Ca2+ signalling pathways activated by acetylcholine in mouse C2C12 myotubes.* Pflogers Archiv European Journal of Physiology, 1994. **428**(3-4): p. 340-345.
5. Kamm, R., et al., *Emergent Behaviors of Integrated Cellular Systems (EBICS)*. 2010, National Science Foundation: Science and Technology Center
6. Salimath, A.S. and A.J. Garcia, *Biofunctional hydrogels for skeletal muscle constructs.* J Tissue Eng Regen Med, 2014.
7. Trotter, J.A. and P.P. Purslow, *Functional morphology of the endomysium in series fibered muscles.* J Morphol, 1992. **212**(2): p. 109-22.
8. Qazi, T.H., et al., *Biomaterials based strategies for skeletal muscle tissue engineering: Existing technologies and future trends.* Biomaterials, 2015. **53**: p. 502-521.
9. Roger Kamm, R.N., Jimmy Hsia, *Cells into Systems*, in *Mechanical Engineering*. 2010.
10. Kevin Kit Parker, J.O.D., Janna C Nawroth, *A tissue-engineered jellyfish with biomimetic propulsion.* Nature Biotechnology, 2012. **30**(8): p. 792.
11. Neill J Turner, S.B., *Regeneration of skeletal muscle.* Cell and Tissue Research, 2011. **347**(3): p. 759-774.
12. Phelps, E.A., et al., *Maleimide Cross-Linked Bioactive PEG Hydrogel Exhibits Improved Reaction Kinetics and Cross-Linking for Cell Encapsulation and In Situ Delivery.* Advanced Materials, 2012. **24**(1): p. 64-70.
13. Cezar, C.A. and D.J. Mooney, *Biomaterial-based delivery for skeletal muscle repair.* Adv Drug Deliv Rev, 2014.
14. Ruegg, J.C., *Muscle Contraction: Molecular and Cellular Physiology*, in *Comprehensive Human Physiology*. 1996, Springer-Verlag: Berlin, Heidelberg.
15. Berne, R.M. and M.N. Levy, *Contractile Mechanism of Muscle Cells*, in *Physiology*, B.M. Koeppen, Editor. 1998, Mosby: St.Louis, MI. p. 269-277.
16. Huxley, A.F. and R. Niedergerke, *Structural changes in muscle during contraction; interference microscopy of living muscle fibres.* Nature, 1954. **173**(4412): p. 971-3.
17. Huxley, H. and J. Hanson, *Changes in the Cross-Striations of Muscle during Contraction and Stretch and their Structural Interpretation.* Nature, 1954. **173**(4412): p. 973-976.
18. Rida, P.C., N. Le Minh, and Y.J. Jiang, *A Notch feeling of somite segmentation and beyond.* Dev Biol, 2004. **265**(1): p. 2-22.

19. Sheffield-Moore, M. and R.J. Urban, *An overview of the endocrinology of skeletal muscle.* Trends Endocrinol Metab, 2004. **15**(3): p. 110-5.
20. Guttridge, D.C., *Signaling pathways weigh in on decisions to make or break skeletal muscle.* Curr. Opin. Clin. Nutr. Metab. Care, 2004. **7**: p. 7.
21. Schulz, R.A. and K.E. Yutzey, *Calcineurin signaling and NFAT activation in cardiovascular and skeletal muscle development.* Dev Biol, 2004. **266**(1): p. 1-16.
22. Martin, P.T., *Role of transcription factors in skeletal muscle and the potential for pharmacological manipulation.* Curr Opin Pharmacol, 2003. **3**(3): p. 300-8.
23. Solloway, M.J. and R.P. Harvey, *Molecular pathways in myocardial development: a stem cell perspective.* Cardiovasc Res, 2003. **58**(2): p. 264-77.
24. Baylies, M.K. and A.M. Michelson, *Invertebrate myogenesis: looking back to the future of muscle development.* Curr Opin Genet Dev, 2001. **11**(4): p. 431-9.
25. Relaix, F., et al., *A Pax3/Pax7-dependent population of skeletal muscle progenitor cells.* Nature, 2005. **435**(7044): p. 948-53.
26. Charge, S.B. and M.A. Rudnicki, *Cellular and Molecular Regulation of Muscle Regeneration*, P. Rev, Editor. 2004, Physiol Rev: Ottawa.
27. Cooper, R.N., et al., *In vivo satellite cell activation via Myf5 and MyoD in regenerating mouse skeletal muscle.* J Cell Sci, 1999. **112 (Pt 17)**: p. 2895-901.
28. Cornelison, D.D. and B.J. Wold, *Single-cell analysis of regulatory gene expression in quiescent and activated mouse skeletal muscle satellite cells.* Dev Biol, 1997. **191**(2): p. 270-83.
29. Fuchtbauer, E.M. and H. Westphal, *MyoD and myogenin are coexpressed in regenerating skeletal muscle of the mouse.* Dev Dyn, 1992. **193**(1): p. 34-9.
30. Grounds, M., et al., *Identification of skeletal muscle precursor cells in vivo by use of MyoD1 and myogenin probes.* Cell Tissue Res, 1992. **267**: p. 5.
31. Zhou, Z. and A. Bornemann, *MRF4 protein expression in regenerating rat muscle.* J Muscle Res Cell Motil, 2001. **22**(4): p. 311-6.
32. Kislinger, T., et al., *Proteome dynamics during C2C12 myoblast differentiation.* Mol Cell Proteomics, 2005. **4**(7): p. 887-901.
33. Decary, S., et al., *Replicative potential and telomere length in human skeletal muscle: implications for satellite cell-mediated gene therapy.* Hum Gene Ther, 1997. **8**(12): p. 1429-38.
34. Silverthorn, D.U., et al., *Muscles*, in *Human Physiology*, H. Dinsey, Editor. 2001, Prentice-Hall: NJ. p. 352-356.
35. Ornatsky, O.I. and J.C. McDermott, *MEF2 protein expression, DNA binding specificity and complex composition, and transcriptional activity in muscle and non-muscle cells.* J Biol Chem, 1996. **271**(40): p. 24927-33.
36. Di Lisi, R., et al., *Combinatorial cis-acting elements control tissue-specific activation of the cardiac troponin I gene in vitro and in vivo.* J Biol Chem, 1998. **273**(39): p. 25371-80.
37. Yang, C.C., et al., *Interaction of myocyte enhancer factor 2 (MEF2) with a mitogen-activated protein kinase, ERK5/BMK1.* Nucleic Acids Res, 1998. **26**(20): p. 4771-7.
38. Youn, H.D., C.M. Grozinger, and J.O. Liu, *Calcium regulates transcriptional repression of myocyte enhancer factor 2 by histone deacetylase 4.* J Biol Chem, 2000. **275**(29): p. 22563-7.

39. Youn, H.D. and J.O. Liu, *Cabin1 represses MEF2-dependent Nur77 expression and T cell apoptosis by controlling association of histone deacetylases and acetylases with MEF2.* Immunity, 2000. **13**(1): p. 85-94.
40. Gillies, A.R. and R.L. Lieber, *Structure and function of the skeletal muscle extracellular matrix.* Muscle Nerve, 2011. **44**(3): p. 318-31.
41. Purslow, P.P. and J.A. Trotter, *The morphology and mechanical properties of endomysium in series-fibred muscles: variations with muscle length.* J Muscle Res Cell Motil, 1994. **15**(3): p. 299-308.
42. Gawlik, K.I. and M. Durbeej, *Skeletal muscle laminin and MDC1A: pathogenesis and treatment strategies.* Skelet Muscle, 2011. **1**(1): p. 9.
43. Andrade, F.H., et al., *Effect of hydrogen peroxide and dithiothreitol on contractile function of single skeletal muscle fibres from the mouse.* J Physiol, 1998. **509 (Pt 2)**: p. 565-75.
44. Knudson, D.V., *Mechanics of the Muscoskeletal system*, in *Fundamentals of Biomechanics*. 2007, Springer: Chico, CA. p. 84-88.
45. *Global burden of musculoskeletal disease revealed in new WHO report.* Bull World Health Organ, 2003. **81**(11): p. 853-4.
46. *Burden of Musculoskeletal Disease Overview. The Burden of Musculoskeletal Diseases in the United States: Prevalence, Societal and Economic Cost*, in *United States Bone and Joint Initiative*. 2011, American Academy of Orthopaedic Surgeons: Rosemont, IL. p. pp 1-20.
47. Juhas, M. and N. Bursac, *Engineering skeletal muscle repair.* Current Opinion in Biotechnology, 2013. **24**(5): p. 880-886.
48. Turner, N.J. and S.F. Badylak, *Regeneration of skeletal muscle.* Cell Tissue Res, 2012. **347**(3): p. 759-74.
49. Sandri, M., *Signaling in muscle atrophy and hypertrophy.* Physiology (Bethesda), 2008. **23**: p. 160-70.
50. Chinnery PF, G.L., Schafer AI, eds, *Muscle Diseases*, in *Cecil Medicine*. 2011, Saunders Elsevier: Philadelphia, Pa.
51. Uhrig, B.A., et al., *Models of Composite Bone and Soft Tissue Limb Trauma*, in *Biomaterials and Regenerative Medicine* 2014.
52. Grogan, B.F. and J.R. Hsu, *Volumetric Muscle Loss.* Journal of American Academy of Orthopaedic Surgeons, 2011. **19**: p. S35-S37.
53. Mase, V.J., Jr., et al., *Clinical application of an acellular biologic scaffold for surgical repair of a large, traumatic quadriceps femoris muscle defect.* Orthopedics, 2010. **33**(7): p. 511.
54. Huard, J., Y. Li, and F.H. Fu, *Muscle injuries and repair: current trends in research.* J Bone Joint Surg Am, 2002. **84-A**(5): p. 822-32.
55. Styf, J., *The effects of functional knee bracing on muscle function and performance.* Sports Med, 1999. **28**(2): p. 77-81.
56. Atala, A., F.K. Kasper, and A.G. Mikos, *Engineering Complex Tissues.* Tissue Eng, 2012.
57. Giannoudis, P.V., et al., *Long-term quality of life in trauma patients following the full spectrum of tibial injury (fasciotomy, closed fracture, grade IIIB/IIIC open fracture and amputation).* Injury, 2009. **40**(2): p. 213-9.

58. Castillo, R.C., et al., *Prevalence of chronic pain seven years following limb threatening lower extremity trauma.* Pain, 2006. **124**(3): p. 321-9.
59. Matsuoka, T., et al., *Long-term physical outcome of patients who suffered crush syndrome after the 1995 Hanshin-Awaji earthquake: prognostic indicators in retrospect.* J Trauma, 2002. **52**(1): p. 33-9.
60. Mimata, Y., et al., *Limb function after excision of a deltoid muscle sarcoma.* J Shoulder Elbow Surg, 2013. **22**(12): p. e1-5.
61. Borrelli, J., Jr., *Management of soft tissue injuries associated with tibial plateau fractures.* J Knee Surg, 2014. **27**(1): p. 5-9.
62. Crow, B.D., et al., *Evaluation of a novel biomaterial for intrasubstance muscle laceration repair.* J Orthop Res, 2007. **25**(3): p. 396-403.
63. Papadakis, M., et al., *Growth hormone replacement in healthy older men improves body composition but not functional ability.* Ann Intern Med, 1996. **124**: p. 8.
64. Miller, K.J., et al., *Hepatocyte growth factor affects satellite cell activation and differentiation in regenerating skeletal muscle.* Am J Physiol Cell Physiol, 2000. **278**(1): p. C174-81.
65. Barnard, W., et al., *Leukemia inhibitory factor (LIF) infusion stimulates skeletal muscle regeneration after injury: injured muscle expresses lif mRNA.* J Neurol Sci, 1994. **123**(1-2): p. 108-13.
66. Lee, C., et al., *Biological intervention based on cell and gene therapy to improve muscle healing after laceration.* J Musculoskeletal Res, 2000. **4**: p. 13.
67. Menetrey, J., et al., *Suturing versus immobilization of a muscle laceration. A morphological and functional study in a mouse model.* Am J Sports Med, 1999. **27**(2): p. 222-9.
68. Zein, N.N., *Interferons in the management of viral hepatitis.* Cytokines Cell Mol Ther, 1998. **4**(4): p. 229-41.
69. Kloen, P., et al., *Suramin inhibits growth and transforming growth factor-beta 1 (TGF-beta 1) binding in osteosarcoma cell lines.* Eur J Cancer, 1994. **30A**(5): p. 678-82.
70. Crisco, J.J., et al., *A muscle contusion injury model. Biomechanics, physiology, and histology.* Am J Sports Med, 1994. **22**(5): p. 702-10.
71. Garrett, W.E., Jr., et al., *Recovery of skeletal muscle after laceration and repair.* J Hand Surg Am, 1984. **9**(5): p. 683-92.
72. Jarvinen, M. and T. Sorvari, *Healing of a crush injury in rat striated muscle. 1. Description and testing of a new method of inducing a standard injury to the calf muscles.* Acta Pathol Microbiol Scand A, 1975. **83**(2): p. 259-65.
73. Kasemkijwattana, C., et al., *Development of approaches to improve the healing following muscle contusion.* Cell Transplant, 1998. **7**(6): p. 585-98.
74. Hurme, T., et al., *Healing of skeletal muscle injury: an ultrastructural and immunohistochemical study.* Med Sci Sports Exerc, 1991. **23**(7): p. 801-10.
75. Raeber, G.P., M.P. Lutolf, and J.A. Hubbell, *Molecularly engineered PEG hydrogels: a novel model system for proteolytically mediated cell migration.* Biophys J, 2005. **89**(2): p. 1374-88.

76. Patterson, J. and J.A. Hubbell, *Enhanced proteolytic degradation of molecularly engineered PEG hydrogels in response to MMP-1 and MMP-2.* Biomaterials, 2010. **31**(30): p. 7836-7845.
77. Raab, M., J.W. Shin, and D.E. Discher, *Matrix elasticity in vitro controls muscle stem cell fate in vivo.* Stem Cell Res Ther, 2010. **1**(5): p. 38.
78. Engler, A.J., et al., *Myotubes differentiate optimally on substrates with tissue-like stiffness: pathological implications for soft or stiff microenvironments.* Journal of Cell Biology, 2004. **166**(6): p. 877-87.
79. Lutolf MP, R.G., Zisch AH, Tirelli N, Hubbell JA, *Cell-responsive synthetic hydrogels.* Advanced Materials, 2003. **15**: p. 888-92.
80. Phelps, E.A., et al., *Bioartificial matrices for therapeutic vascularization.* Proc Natl Acad Sci U S A, 2010. **107**(8): p. 3323-8.
81. Miller, J.B., et al., *Cellular and molecular diversity in skeletal muscle development: news from in vitro and in vivo.* Bioessays, 1993. **15**(3): p. 191-6.
82. Bajaj, P., et al., *Patterning the differentiation of C2C12 skeletal myoblasts.* Integr Biol (Camb), 2011. **3**(9): p. 897-909.
83. Buck, C.A. and A.F. Horwitz, *Cell surface receptors for extracellular matrix molecules.* Annu Rev Cell Biol, 1987. **3**: p. 179-205.
84. Huijing, P.A., *Muscle as a collagen fiber reinforced composite: a review of force transmission in muscle and whole limb.* Journal of Biomechanics, 1999. **32**(4): p. 329-345.
85. Purslow, P.P., *The structure and functional significance of variations in the connective tissue within muscle.* Comparative Biochemistry and Physiology a-Molecular and Integrative Physiology, 2002. **133**(4): p. 947-966.
86. Wolf, M.T., et al., *Naturally derived and synthetic scaffolds for skeletal muscle reconstruction.* Adv Drug Deliv Rev, 2014.
87. Page, R.L., et al., *Restoration of skeletal muscle defects with adult human cells delivered on fibrin microthreads.* Tissue Eng Part A, 2011. **17**(21-22): p. 2629-40.
88. Janmey, P.A., J.P. Winer, and J.W. Weisel, *Fibrin gels and their clinical and bioengineering applications.* Journal of the Royal Society Interface, 2009. **6**(30): p. 1-10.
89. Hill, E., T. Boontheekul, and D.J. Mooney, *Designing scaffolds to enhance transplanted myoblast survival and migration.* Tissue Eng, 2006. **12**(5): p. 1295-304.
90. Takahashi, H., et al., *The use of anisotropic cell sheets to control orientation during the self-organization of 3D muscle tissue.* Biomaterials, 2013. **34**: p. 7372-7380.
91. Tomblyn, S., et al., *Keratin hydrogel carrier system for simultaneous delivery of exogenous growth factors and muscle progenitor cells.* J Biomed Mater Res B Appl Biomater, 2015.
92. Fujita, H., K. Shimizu, and E. Nagamori, *Novel method for fabrication of skeletal muscle construct from the C2C12 myoblast cell line using serum-free medium AIM-V.* Biotechnology and Bioengineering, 2009. **103**(5): p. 1034-1041.
93. Kroehne, V., et al., *Use of a novel collagen matrix with oriented pore structure for muscle cell differentiation in cell culture and in grafts.* J Cell Mol Med, 2008. **12**(5a): p. 1640-1648.

94. Choi, J., et al., *The influence of electrospun aligned poly(epsilon-caprolactone)/collagen nanofiber meshes on the formation of self-aligned skeletal muscle myotubes.* Biomaterials, 2008. **29**(19): p. 2899-906.
95. Hoque, M.E., et al., *Processing of polycaprolactone and polycaprolactone-based copolymers into 3D scaffolds, and their cellular responses.* Tissue Eng Part A, 2009. **15**(10): p. 3013-24.
96. Saxena, A., et al., *Skeletal muscle tissue engineering using isolated myoblasts on synthetic biodegradable polymers: preliminary studies.* Tissue Eng, 1999. **5**(6): p. 525-532.
97. Saxena, A., G. Willital, and J. Vacanti, *Vascularized three-dimensional skeletal muscle tissue-engineering.* Biomed Mater Eng, 2001. **11**(4): p. 275-81.
98. Mulder, M., R. Hitchcock, and P. Tresco, *Skeletal myogenesis on elastomeric substrates: implications for tissue engineering.* J Biomater Sci Polym Ed., 1998. **9**(7): p. 731-48.
99. Riboldi, S., et al., *Electrospun degradable polyesterurethane membranes: potential scaffolds for skeletal muscle tissue engineering.* Biomaterials, 2005. **26**(22): p. 4606-15.
100. Peyton, S.R., et al., *The emergence of ECM mechanics and cytoskeletal tension as important regulators of cell function.* Cell Biochem Biophys, 2007. **47**: p. 300-320.
101. Place, E.S., et al., *Synthetic polymer scaffolds for tissue engineering.* Chemical Society Reviews, 2009. **38**(4): p. 1139-1151.
102. Gilbert, P.M., et al., *Substrate Elasticity Regulates Skeletal Muscle Stem Cell Self-Renewal in Culture.* Science, 2010. **329**(5995): p. 1078-1081.
103. Fuoco, C., et al., *3D hydrogel environment rejuvenates aged pericytes for skeletal muscle tissue engineering.* Front Physiol, 2014. **5**: p. 203.
104. Fuoco, C., et al., *Injectable polyethylene glycol-fibrinogen hydrogel adjuvant improves survival and differentiation of transplanted mesoangioblasts in acute and chronic skeletal-muscle degeneration.* Skelet Muscle, 2012. **2**(1): p. 24.
105. Costa, K.D., E.J. Lee, and J.W. Holmes, *Creating alignment and anisotropy in engineered heart tissue: role of boundary conditions in a model three-dimensional culture system.* Tissue Eng, 2003. **9**(4): p. 567-77.
106. Colton, C.K., *Implantable biohybrid artificial organs.* Cell Transplant, 1995. **4**(4): p. 415-36.
107. Ilievski, F., et al., *Soft robotics for chemists.* Angew Chem Int Ed Engl, 2011. **50**(8): p. 1890-5.
108. Ueoka, Y., J. Gong, and Y. Osada, *Chemomechanical Polymer Gel with Fish-like Motion.* Journal of Intelligent Material Systems and Structures, 1997. **8**(5): p. 465-471.
109. Hamlen, R.P., C.E. Kent, and S.N. Shafer, *Electrolytically Activated Contractile Polymer.* Nature, 1965. **206**(4989): p. 1149-1150.
110. Shiga, T. and T. Kurauchi, *Deformation of polyelectrolyte gels under the influence of electric field.* Journal of Applied Polymer Science, 1990. **39**(1112): p. 2305-2320.

111. Robert Shepherd, F.I., Wonjae Choi, Stephen A Morin, Adam Stokes, Aaron Mazzeo, Xin Chen, Michael Wang, George Whitesides, *Multigait soft robot.* PNAS, 2011. **108**(51): p. 20400-20403.
112. Ribuan, M.N., K. Suzumori, and S. Wakimoto, *New Pneumatic Rubber Leg Mechanism for Omnidirectional Locomotion.* International Journal of Automation Technology, 2014. **8**(2): p. 8.
113. Breger, J.C., et al., *Self-folding thermo-magnetically responsive soft microgrippers.* ACS Appl Mater Interfaces, 2015. **7**(5): p. 3398-405.
114. Suzumori, K., *Elastic materials producing compliant robots.* Robotics and Autonomous Systems, 1996. **18**(1-2): p. 135-140.
115. Duffy, R.M. and A.W. Feinberg, *Engineered skeletal muscle tissue for soft robotics: fabrication strategies, current applications, and future challenges.* Wiley Interdiscip Rev Nanomed Nanobiotechnol, 2014. **6**(2): p. 178-95.
116. Ham, R., et al., *Compliant actuator designs.* IEEE Robotics & Automation Magazine, 2009. **16**(3): p. 81-94.
117. Pette, D. and G. Vrbova, *Neural control of phenotypic expression in mammalian muscle fibers.* Muscle Nerve, 1985. **8**(8): p. 676-89.
118. Hu, W., et al., *Hydrogel microrobots actuated by optically generated vapour bubbles.* Lab Chip, 2012. **12**(19): p. 3821-6.
119. Mahmut Selman Sakar, D.N., Harry Asada, Chris Chen, Ron Weiss, Roger Kamm, *Formation and optogenetic control of engineered 3D skeletal muscle bioactuators.* Lab on a Chip, 2012.
120. Fujita, H., K. Shimizu, and E. Nagamori, *Novel Method for Measuring Active Tension Generation by C2C12 Myotube Using UV-Crosslinked Collagen Film.* Biotechnology and Bioengineering, 2010.
121. Dennis, R.G. and P.E. Kosnik, 2nd, *Excitability and isometric contractile properties of mammalian skeletal muscle constructs engineered in vitro.* In Vitro Cell Dev Biol Anim, 2000. **36**(5): p. 327-35.
122. Lam, M.T., et al., *Microfeature guided skeletal muscle tissue engineering for highly organized 3-dimensional free-standing constructs.* Biomaterials, 2009. **30**(6): p. 1150-5.
123. Juhas, M., et al., *Biomimetic engineered muscle with capacity for vascular integration and functional maturation in vivo.* Proc Natl Acad Sci U S A, 2014. **111**(15): p. 5508-13.
124. Bian, W., et al., *Mesoscopic hydrogel molding to control the 3D geometry of bioartificial muscle tissues.* Nat Protoc, 2009. **4**(10): p. 1522-34.
125. Bian, W. and N. Bursac, *Engineered skeletal muscle tissue networks with controllable architecture.* Biomaterials, 2009. **30**(7): p. 1401-12.
126. Hinds, S., et al., *The role of extracellular matrix composition in structure and function of bioengineered skeletal muscle.* Biomaterials, 2011. **32**(14): p. 3575-83.
127. Bian, W., et al., *Local tissue geometry determines contractile force generation of engineered muscle networks.* Tissue Eng Part A, 2012. **18**(9-10): p. 957-67.
128. Yamamoto, Y., et al., *Functional evaluation of artificial skeletal muscle tissue constructs fabricated by a magnetic force-based tissue engineering technique.* Tissue Eng Part A, 2011. **17**(1-2): p. 107-14.

129. Yamamoto, Y., et al., *Preparation of artificial skeletal muscle tissues by a magnetic force-based tissue engineering technique.* J Biosci Bioeng, 2009. **108**(6): p. 538-43.
130. David Yaffe, O.S., *Serial Passaging and differentiation of myogenic cells isolated frm dystrophic mouse muscle.* Nature, 1977. **270**(22/29).
131. Lawson, M.A. and P.P. Purslow, *Differentiation of myoblasts in serum-free media: effects of modified media are cell line-specific.* Cells Tissues Organs, 2000. **167**(2-3): p. 130-7.
132. Dennis, R.G., et al., *Excitability and contractility of skeletal muscle engineered from primary cultures and cell lines.* Am J Physiol Cell Physiol, 2001. **280**(2): p. C288-95.
133. García, A.J., M.D. Vega, and D. Boettiger, *Modulation of cell proliferation and differentiation through substrate-dependent changes in fibronectin conformation.* Molecular Biology of the Cell, 1999. **10**(3): p. 785-798.
134. Rowley, J.A. and D.J. Mooney, *Alginate type and RGD density control myoblast phenotype.* Journal of Biomedical Materials Research, 2002. **60**(2): p. 217-223.
135. Peng-Yuan Wang, H.T., Wei-Bor Tsai, *The Roles of RGD and Grooved Topography in the Adhesion, Morphology, and Differentiation of C2C12 Skeletal Myoblasts.* Biotechnology and Bioengineering, 2012. **109**(8).
136. Zhao, Y., et al., *Fabrication of skeletal muscle constructs by topographic activation of cell alignment.* Biotechnol Bioeng, 2009. **102**(2): p. 624-31.
137. Weist, M.R., et al., *TGF-beta1 enhances contractility in engineered skeletal muscle.* J Tissue Eng Regen Med, 2013. **7**(7): p. 562-71.
138. Pedrotty, D.M., et al., *Engineering skeletal myoblasts: roles of three-dimensional culture and electrical stimulation.* Am J Physiol Heart Circ Physiol, 2005. **288**(4): p. H1620-6.
139. Marquette, M.L., D. Byerly, and M. Sognier, *A novel in vitro three-dimensional skeletal muscle model.* In Vitro Cell Dev Biol Anim, 2007. **43**(7): p. 255-63.
140. Haraguchi, Y., et al., *Fabrication of functional three-dimensional tissues by stacking cell sheets in vitro.* Nat Protoc, 2012. **7**(5): p. 850-8.
141. Takahashi, H., et al., *The use of anisotropic cell sheets to control orientation during the self-organization of 3D muscle tissue.* Biomaterials, 2013. **34**(30): p. 7372-80.
142. Shimizu, T., et al., *Cell sheet engineering for myocardial tissue reconstruction.* Biomaterials, 2003. **24**(13): p. 2309-16.
143. Shimizu, K., H. Fujita, and E. Nagamori, *Evaluation systems of generated forces of skeletal muscle cell-based bio-actuators.* J Biosci Bioeng, 2013. **115**(2): p. 115-21.
144. Fujita, H., et al., *Evaluation of Serum-Free Differentiation Conditions for C2C12 Myoblast Cells Assessed as to Active Tension Generation Capability.* Biotechnology and Bioengineering, 2010. **107**(5).
145. Sakar, M.S., et al., *Formation and optogenetic control of engineered 3D skeletal muscle bioactuators.* Lab Chip, 2012. **12**(23): p. 4976-85.
146. Vandenburgh, H., et al., *Drug-screening platform based on the contractility of tissue-engineered muscle.* Muscle Nerve, 2008. **37**(4): p. 438-47.

147. Barton, E.R., G. Lynch, and T.S. Khurana, *Measuring isometric force of isolated mouse muscles in vitro*. 2008, Wellstone Muscular Dystrophy Center: Washington, DC. p. 14.
148. Head, S.I., B. Greenaway, and S. Chan, *Incubating isolated mouse EDL muscles with creatine improves force production and twitch kinetics in fatigue due to reduction in ionic strength.* PLoS One, 2011. **6**(8): p. e22742.
149. Kabumoto, K., et al., *Voluntary movement controlled by the surface EMG signal for tissue-engineered skeletal muscle on a gripping tool.* Tissue Eng Part A, 2013. **19**(15-16): p. 1695-703.
150. Wendel, J.S., et al., *Functional consequences of a tissue-engineered myocardial patch for cardiac repair in a rat infarct model.* Tissue Eng Part A, 2014. **20**(7-8): p. 1325-35.
151. Ferenczi, M.A., et al., *Fluorescence Lifetime Imaging Reveals that the Environment of the ATP Binding Site of Myosin in Muscle Senses Force.* Biophys J, 2010. **99**: p. 2163-69.
152. Feinberg, A.W., et al., *Muscular thin films for building actuators and powering devices.* Science, 2007. **317**(5843): p. 1366-70.
153. Sun, Y., et al., *Optimizing the structure and contractility of engineered skeletal muscle thin films.* Acta Biomater, 2013. **9**(8): p. 7885-94.
154. Cvetkovic, C., et al., *Three-dimensionally printed biological machines powered by skeletal muscle.* Proc Natl Acad Sci U S A, 2014. **111**(28): p. 10125-30.
155. Nichols, R., J. Malamud, and R. Godt, *Relationship between short-range stiffness and yielding in type-identified, chemically skinned muscle fibers from the cat triceps surae muscles.* J. Neurophysiology, 1996. **76**: p. 2280-2289.
156. Lamb, G.D. and G.S. Posterino, *Effects of oxidation and reduction on contractile function in skeletal muscle fibres of the rat.* J Physiol, 2003. **546**(Pt 1): p. 149-63.
157. Oba, T., et al., *A novel phasic contraction induced by dithiothreitol in frog skeletal muscle.* Gen Pharmacol, 1996. **27**(8): p. 1361-6.
158. Zhao, R., C.S. Chen, and D.H. Reich, *Force-driven evolution of mesoscale structure in engineered 3D microtissues and the modulation of tissue stiffening.* Biomaterials, 2014.
159. Bond, L.M., et al., *Small-molecule inhibitors of myosin proteins.* Future Med Chem, 2013. **5**(1): p. 41-52.
160. Wenningmann, I. and J.P. Dilger, *The kinetics of inhibition of nicotinic acetylcholine receptors by (+)-tubocurarine and pancuronium.* Mol Pharmacol, 2001. **60**(4): p. 790-6.
161. Phelps, E.A., et al., *Vasculogenic bio-synthetic hydrogel for enhancement of pancreatic islet engraftment and function in type 1 diabetes.* Biomaterials, 2013.
162. Salimath, A.S., et al., *Dual delivery of hepatocyte and vascular endothelial growth factors via a protease-degradable hydrogel improves cardiac function in rats.* PLoS One, 2012. **7**(11): p. e50980.
163. Gersbach, C.A., et al., *Runx2/Cbfa1 stimulates transdifferentiation of primary skeletal myoblasts into a mineralizing osteoblastic phenotype.* Exp.Cell Res, 2004. **300**(2): p. 406-417.

164. Lamont, C. and D.J. Miller, *Calcium sensitizing action of carnosine and other endogenous imidazoles in chemically skinned striated muscle.* J Physiol, 1992. **454**: p. 421-34.
165. Purslow, P.P., *The structure and functional significance of variations in the connective tissue within muscle.* Comparative Biochemistry and Physiology Part A: Molecular & Integrative Physiology, 2002. **133**(4): p. 947-966.
166. Charrasse, S., et al., *N-cadherin-dependent cell-cell contact regulates Rho GTPases and beta-catenin localization in mouse C2C12 myoblasts.* J Cell Biol, 2002. **158**(5): p. 953-65.
167. Jordan S. Miller, S.N.B., Christopher S. Chen, *Rapid casting of patterned vascular networks for perfusable engineered three-dimensional tissues.* Nature Materials, 2012.
168. Madden, L., et al., *Bioengineered human myobundles mimic clinical responses of skeletal muscle to drugs.* Elife, 2014. **4**: p. e04885.
169. Neal, D., et al., *Mechanical Characterization and Shape Optimization of Fascicle-Like 3D Skeletal Muscle Tissues Contracted with Electrical and Optical Stimuli.* Tissue Eng Part A, 2015. **21**(11-12): p. 1848-1858.
170. Neal, D., et al., *Formation of elongated fascicle-inspired 3D tissues consisting of high-density, aligned cells using sacrificial outer molding.* Lab on a Chip, 2014. **14**(11): p. 1907-1916.
171. van der Schaft, D.W., et al., *Engineering skeletal muscle tissues from murine myoblast progenitor cells and application of electrical stimulation.* J Vis Exp, 2013(73): p. e4267.
172. Hume, S.L., et al., *Alignment of multi-layered muscle cells within three-dimensional hydrogel macrochannels.* Acta Biomaterialia, 2012. **8**(6): p. 2193-2202.
173. Ifkovits, J.L., et al., *Injectable hydrogel properties influence infarct expansion and extent of postinfarction left ventricular remodeling in an ovine model.* Proc Natl Acad Sci U S A, 2010. **107**(25): p. 11507-12.
174. Wall, S.T., et al., *Biomimetic matrices for myocardial stabilization and stem cell transplantation.* J Biomed Mater Res A, 2010. **95**(4): p. 1055-66.
175. Kannan, R.Y., et al., *The roles of tissue engineering and vascularisation in the development of micro-vascular networks: a review.* Biomaterials, 2005. **26**(14): p. 1857-75.
176. Bian, W. and N. Bursac, *Tissue engineering of functional skeletal muscle: challenges and recent advances.* IEEE Eng Med Biol Mag, 2008. **27**(5): p. 109-13.
177. Agarwal, A., et al., *Micropatterning Alginate Substrates for In Vitro Cardiovascular Muscle on a Chip.* Advanced Functional Materials, 2013. **23**(30): p. 3738-3746.
178. Li, J.Y., et al., *Preparation of micron/submicron hybrid patterns via a two-stage UV-imprint technique and their dimensional effects on cell adhesion and alignment.* Biofabrication, 2013. **5**(3).
179. Wang, P.Y., H.T. Yu, and W.B. Tsai, *Modulation of alignment and differentiation of skeletal myoblasts by submicron ridges/grooves surface structure.* Biotechnol Bioeng, 2010. **106**(2): p. 285-94.

180. Yang, H.S., et al., *Nanopatterned muscle cell patches for enhanced myogenesis and dystrophin expression in a mouse model of muscular dystrophy.* Biomaterials, 2014. **35**(5): p. 1478-86.
181. Kroehne, V., et al., *Use of a novel collagen matrix with oriented pore structure for muscle cell differentiation in cell culture and in grafts.* J Cell Mol Med, 2008. **12**(5A): p. 1640-8.
182. Jana, S., A. Cooper, and M. Zhang, *Chitosan scaffolds with unidirectional microtubular pores for large skeletal myotube generation.* Adv Healthc Mater, 2013. **2**(4): p. 557-61.
183. Legant, W.R., et al., *Microfabricated tissue gauges to measure and manipulate forces from 3D microtissues.* Proc Natl Acad Sci U S A, 2009. **106**(25): p. 10097-102.
184. Ahadian, S., et al., *Hybrid hydrogels containing vertically aligned carbon nanotubes with anisotropic electrical conductivity for muscle myofiber fabrication.* Sci Rep, 2014. **4**: p. 4271.
185. VanDusen, K.W., et al., *Engineered skeletal muscle units for repair of volumetric muscle loss in the tibialis anterior muscle of a rat.* Tissue Eng Part A, 2014. **20**(21-22): p. 2920-30.
186. Rangarajan, S., L. Madden, and N. Bursac, *Use of Flow, Electrical, and Mechanical Stimulation to Promote Engineering of Striated Muscles.* BMES, 2013.
187. Jun, I., S. Jeong, and H. Shin, *The stimulation of myoblast differentiation by electrically conductive sub-micron fibers.* Biomaterials, 2009. **30**(11): p. 2038-47.
188. Gilmore, K.J., et al., *Skeletal muscle cell proliferation and differentiation on polypyrrole substrates doped with extracellular matrix components.* Biomaterials, 2009. **30**(29): p. 5292-304.
189. Ahmed, W.W., et al., *Myoblast morphology and organization on biochemically micro-patterned hydrogel coatings under cyclic mechanical strain.* Biomaterials, 2010. **31**(2): p. 250-258.
190. Bayati, V., et al., *The evaluation of cyclic uniaxial strain on myogenic differentiation of adipose-derived stem cells.* Tissue Cell, 2011. **43**(6): p. 359-66.
191. Nagamine, K., et al., *Spatiotemporally controlled contraction of micropatterned skeletal muscle cells on a hydrogel sheet.* Lab Chip, 2011. **11**(3): p. 513-7.
192. Ahadian, S., et al., *A contactless electrical stimulator: application to fabricate functional skeletal muscle tissue.* Biomed Microdevices, 2013. **15**(1): p. 109-15.
193. Uzel, S.G., A. Pavesi, and R.D. Kamm, *Microfabrication and microfluidics for muscle tissue models.* Prog Biophys Mol Biol, 2014.
194. Choi, Y.S., et al., *Mechanical derivation of functional myotubes from adipose-derived stem cells.* Biomaterials, 2012. **33**(8): p. 2482-91.
195. Munoz-Pinto, D.J., et al., *Relative impact of form-induced stress vs. uniaxial alignment on multipotent stem cell myogenesis.* Acta Biomater, 2012. **8**(11): p. 3974-81.
196. Tanaka, T., et al., *Alignment of Skeletal Muscle Cells Cultured in Collagen Gel by Mechanical and Electrical Stimulation.* International Journal of Tissue Engineering, 2014. **2014**: p. 1-5.

197. Powell, C.A., et al., *Mechanical stimulation improves tissue-engineered human skeletal muscle.* Am J Physiol Cell Physiol, 2002. **283**(5): p. C1557-65.
198. Sandow, A., *Excitation-contraction coupling in muscular response.* Yale J Biol Med, 1952. **25**(3): p. 176-201.
199. Ng, C.P., B. Hinz, and M.A. Swartz, *Interstitial fluid flow induces myofibroblast differentiation and collagen alignment in vitro.* J Cell Sci, 2005. **118**(Pt 20): p. 4731-9.
200. Stein, A.M., et al., *An algorithm for extracting the network geometry of three-dimensional collagen gels.* J Microsc, 2008. **232**(3): p. 463-75.
201. Chrzanowska-Wodnicka, M. and K. Burridge, *Rho-stimulated contractility drives the formation of stress fibers and focal adhesions.* Journal of Cell Biology, 1996. **133**(6): p. 1403-15.
202. Ostrovidov, S., et al., *Three-dimensional co-culture of C2C12/PC12 cells improves skeletal muscle tissue formation and function.* J Tissue Eng Regen Med, 2014.
203. Ilaria E. Palama, S.D.A., Addolorata M.L. Coluccia, Giuseppe Gigli, *Micropatterned Polyelectrolyte Nanofilms Promote Alignment and Myogenic Differentiation of C2C12 Cells in Standard Growth Media.* Biotechnology and Bioengineering, 2012.
204. Ostrovidov, S., et al., *Myotube formation on gelatin nanofibers e Multi-walled carbon nanotubes hybrid scaffolds.* Biomaterials, 2014.
205. Nishiyama, T., I. Kii, and A. Kudo, *Inactivation of Rho/ROCK signaling is crucial for the nuclear accumulation of FKHR and myoblast fusion.* J Biol Chem, 2004. **279**(45): p. 47311-9.
206. Castellani, L., et al., *Fine regulation of RhoA and Rock is required for skeletal muscle differentiation.* J Biol Chem, 2006. **281**(22): p. 15249-57.
207. Maekawa, M., *Signaling from Rho to the Actin Cytoskeleton Through Protein Kinases ROCK and LIM-kinase.* Science, 1999. **285**(5429): p. 895-898.
208. Sutcliffe, W.J., *Stress analysis of toroidal shells of elliptical cross-section.* International Journal of Mechanical Sciences, 1971. **13**(11): p. 951-958.
209. Veličković, V., *Stress and Strain States in the Material of the Stressed Toroidal Container for Liquefied Petroleum Gas*. 2007, Military Technical Institute: Belgrade, Serbia.
210. Latour, L.L., et al., *Time-dependent diffusion of water in a biological model system.* Proceedings of the National Academy of Sciences, 1994. **91**(4): p. 1229-1233.
211. Klinge, L., et al., *From T-tubule to sarcolemma: damage-induced dysferlin translocation in early myogenesis.* FASEB J, 2007. **21**(8): p. 1768-76.
212. Flucher, B.E., et al., *Biogenesis of transverse tubules in skeletal muscle in vitro.* Dev Biol, 1991. **145**(1): p. 77-90.
213. Chan, V., H.H. Asada, and R. Bashir, *Utilization and control of bioactuators across multiple length scales.* Lab Chip, 2014. **14**(4): p. 653-70.
214. van der Schaft, D.W., et al., *Mechanoregulation of vascularization in aligned tissue-engineered muscle: a role for vascular endothelial growth factor.* Tissue Eng Part A, 2011. **17**(21-22): p. 2857-65.

215. Criswell, T.L., et al., *The role of endothelial cells in myofiber differentiation and the vascularization and innervation of bioengineered muscle tissue in vivo.* Biomaterials, 2013. **34**(1): p. 140-9.
216. Shvartsman, D., et al., *Sustained delivery of VEGF maintains innervation and promotes reperfusion in ischemic skeletal muscles via NGF/GDNF signaling.* Mol Ther, 2014. **22**(7): p. 1243-53.
217. Ruvinov, E., J. Leor, and S. Cohen, *The promotion of myocardial repair by the sequential delivery of IGF-1 and HGF from an injectable alginate biomaterial in a model of acute myocardial infarction.* Biomaterials, 2011. **32**(2): p. 565-78.
218. Davis, M.E., et al., *Local myocardial insulin-like growth factor 1 (IGF-1) delivery with biotinylated peptide nanofibers improves cell therapy for myocardial infarction.* Proc Natl Acad Sci U S A, 2006. **103**(21): p. 8155-60.
219. Hill, E., T. Boontheekul, and D.J. Mooney, *Regulating activation of transplanted cells controls tissue regeneration.* Proc Natl Acad Sci U S A, 2006. **103**(8): p. 2494-9.
220. Shekaran, A., et al., *Bone regeneration using an alpha 2 beta 1 integrin-specific hydrogel as a BMP-2 delivery vehicle.* Biomaterials, 2014. **35**(21): p. 5453-61.
221. Lee, T.T., et al., *Light-triggered in vivo activation of adhesive peptides regulates cell adhesion, inflammation and vascularization of biomaterials.* Nat Mater, 2015. **14**(3): p. 352-60.
222. Baum, K., et al., *Comparison of skeletal muscle strength between cardiac patients and age-matched healthy controls.* Int J Med Sci, 2009. **6**(4): p. 7.
223. McNally, E.M. and J.A. Goldstein, *Interplay between heart and skeletal muscle disease in heart failure: the 2011 George E. Brown Memorial Lecture.* Circ Res, 2012. **110**(5): p. 749-54.
224. Petrof, B.J., et al., *Dystrophin protects the sarcolemma from stresses developed during muscle contraction.* Proc Natl Acad Sci U S A, 1993. **90**(8): p. 3710-4.
225. Danialou, G., et al., *Dystrophin-deficient cardiomyocytes are abnormally vulnerable to mechanical stress-induced contractile failure and injury.* FASEB J, 2001. **15**(9): p. 1655-7.
226. D'Angelo, M.G., et al., *Respiratory pattern in an adult population of dystrophic patients.* J Neurol Sci, 2011. **306**(1-2): p. 54-61.
227. Ugalde, V., et al., *Respiratory abdominal muscle recruitment and chest wall motion in myotonic muscular dystrophy.* J Appl Physiol (1985), 2001. **91**(1): p. 395-407.
228. DeFronzo, R.A. and D. Tripathy, *Skeletal muscle insulin resistance is the primary defect in type 2 diabetes.* Diabetes Care, 2009. **32 Suppl 2**: p. S157-63.
229. Ionov, L., *Biomimetic Hydrogel-Based Actuating Systems.* Advanced Functional Materials, 2013. **23**(36): p. 4555-4570.
230. Bryson, J.B., et al., *Optical control of muscle function by transplantation of stem cell-derived motor neurons in mice.* Science, 2014. **344**(6179): p. 94-7.
231. Morimoto, Y., et al., *Three-dimensional neuron-muscle constructs with neuromuscular junctions.* Biomaterials, 2013. **34**(37): p. 9413-9.
232. Langelaan, M.L.P., et al., *Meet the new meat: tissue engineered skeletal muscle.* Trends in Food Science & Technology, 2010. **21**(2): p. 59-66.

233. Roger, V.L., et al., *Heart disease and stroke statistics--2012 update: a report from the American Heart Association.* Circulation, 2012. **125**(1): p. e2-e220.
234. Almeda, F.Q., R.J. Snell, and J.E. Parrillo, *The Contemporary Management of Acute Myocardial Infarction.* Critical Care Clinics, 2001. **17**(2): p. 411-434.
235. Anversa, P., *Myocyte Death in the Pathological Heart.* Circulation Research, 2000. **86**(2): p. 121-124.
236. Anversa, P., et al., *Cellular mechanisms of cardiac failure in the infarcted heart.* Cardiologia, 1995. **40**(12): p. 909-20.
237. Kajstura, J., et al., *Apoptotic and necrotic myocyte cell deaths are independent contributing variables of infarct size in rats.* Lab Invest, 1996. **74**(1): p. 86-107.
238. Anversa, P., A. Leri, and J. Kajstura, *Cardiac regeneration.* J Am Coll Cardiol, 2006. **47**(9): p. 1769-76.
239. Assmus, B., et al., *Transcoronary transplantation of progenitor cells after myocardial infarction.* N Engl J Med, 2006. **355**(12): p. 1222-32.
240. Kang, H.-J., et al., *Effects of intracoronary infusion of peripheral blood stem-cells mobilised with granulocyte-colony stimulating factor on left ventricular systolic function and restenosis after coronary stenting in myocardial infarction: the MAGIC cell randomised clinical trial.* The Lancet, 2004. **363**(9411): p. 751-756.
241. Sy, J.C. and M.E. Davis, *Delivering regenerative cues to the heart: cardiac drug delivery by microspheres and peptide nanofibers.* J Cardiovasc Transl Res, 2010. **3**(5): p. 461-8.
242. Engel, F.B., et al., *FGF1/p38 MAP kinase inhibitor therapy induces cardiomyocyte mitosis, reduces scarring, and rescues function after myocardial infarction.* Proc Natl Acad Sci U S A, 2006. **103**(42): p. 15546-51.
243. Hsieh, P.C., et al., *Controlled delivery of PDGF-BB for myocardial protection using injectable self-assembling peptide nanofibers.* J Clin Invest, 2006. **116**(1): p. 237-48.
244. Ozawa, C.R., et al., *Microenvironmental VEGF concentration, not total dose, determines a threshold between normal and aberrant angiogenesis.* J Clin Invest, 2004. **113**(4): p. 516-27.
245. Schwarz, E.R., et al., *Evaluation of the effects of intramyocardial injection of DNA expressing vascular endothelial growth factor (VEGF) in a myocardial infarction model in the rat—angiogenesis and angioma formation.* Journal of the American College of Cardiology, 2000. **35**(5): p. 1323-1330.
246. Epstein, S.E., et al., *Angiogenesis Therapy : Amidst the Hype, the Neglected Potential for Serious Side Effects.* Circulation, 2001. **104**(1): p. 115-119.
247. Patterson, J. and J.A. Hubbell, *SPARC-derived protease substrates to enhance the plasmin sensitivity of molecularly engineered PEG hydrogels.* Biomaterials, 2011. **32**(5): p. 1301-10.
248. French, K.M., et al., *A naturally derived cardiac extracellular matrix enhances cardiac progenitor cell behavior in vitro.* Acta Biomater, 2012. **8**(12): p. 4357-64.
249. Guerra, S., et al., *Myocyte Death in the Failing Human Heart Is Gender Dependent.* Circulation Research, 1999. **85**(9): p. 856-866.
250. Christian Danielsen, C., *Increased Amounts of Collagenase and Gelatinase in Porcine Myocardium Following Ischemia and Reperfusion.* Journal of Molecular and Cellular Cardiology, 1998. **30**(7): p. 1431-1442.

251. Jacot, J.G., et al., *A simple microindentation technique for mapping the microscale compliance of soft hydrated materials and tissues.* J Biomed Mater Res A, 2006. **79**(3): p. 485-94.
252. Jacot, J.G., et al., *Cardiac myocyte force development during differentiation and maturation.* Ann N Y Acad Sci, 2010. **1188**: p. 121-7.
253. Jacot, J.G., A.D. McCulloch, and J.H. Omens, *Substrate stiffness affects the functional maturation of neonatal rat ventricular myocytes.* Biophys J, 2008. **95**(7): p. 3479-87.
254. Nakagawa, K., et al., *Angiogenesis and Its Regulation: Roles of Vascular Endothelial Cell Growth Factor.* Seminars in Thrombosis and Hemostasis, 2000. **Volume 26**(Number 01): p. 061-066.
255. Kloner, R.A., et al., *Intramyocardial injection of DNA encoding vascular endothelial growth factor in a myocardial infarction model.* J Thromb Thrombolysis, 2000. **10**(3): p. 285-9.
256. Cho, K.R., et al., *Therapeutic angiogenesis using naked DNA expressing two isoforms of the hepatocyte growth factor in a porcine acute myocardial infarction model.* Eur J Cardiothorac Surg, 2008. **34**(4): p. 857-63.
257. Morishita, R., et al., *Therapeutic Angiogenesis using Hepatocyte Growth Factor (HGF).* Current Gene Therapy, 2004. **4**(2): p. 199-206.
258. Ruvinov, E., J. Leor, and S. Cohen, *The effects of controlled HGF delivery from an affinity-binding alginate biomaterial on angiogenesis and blood perfusion in a hindlimb ischemia model.* Biomaterials, 2010. **31**(16): p. 4573-82.
259. Yamaguchi, T., et al., *Therapeutic angiogenesis induced by injecting hepatocyte growth factor in ischemic canine hearts.* Surg Today, 2005. **35**(10): p. 855-60.
260. Siltanen, A., et al., *hHGF overexpression in myoblast sheets enhances their angiogenic potential in rat chronic heart failure.* PLoS One, 2011. **6**(4): p. e19161.
261. Zhu, X.Y., et al., *Transplantation of adipose-derived stem cells overexpressing hHGF into cardiac tissue.* Biochem Biophys Res Commun, 2009. **379**(4): p. 1084-90.
262. Miyagawa, S., et al., *Angiogenic gene cell therapy using suicide gene system regulates the effect of angiogenesis in infarcted rat heart.* Transplantation, 2006. **81**(6): p. 902-7.
263. Angoulvant, D., et al., *Mesenchymal stem cell conditioned media attenuates in vitro and ex vivo myocardial reperfusion injury.* J Heart Lung Transplant, 2011. **30**(1): p. 95-102.
264. Fatma, S., et al., *Factors Released from Embryonic Stem Cells Stimulate c-kit-FLK-1(+ve) Progenitor Cells and Enhance Neovascularization.* Antioxid Redox Signal, 2010. **13**(12): p. 1857-65.
265. Perez-Ilzarbe, M., et al., *Characterization of the paracrine effects of human skeletal myoblasts transplanted in infarcted myocardium.* Eur J Heart Fail, 2008. **10**(11): p. 1065-72.
266. Chen, R.R., et al., *Spatio-temporal VEGF and PDGF delivery patterns blood vessel formation and maturation.* Pharm Res, 2007. **24**(2): p. 258-64.

267. Sun, Q., et al., *Sustained release of multiple growth factors from injectable polymeric system as a novel therapeutic approach towards angiogenesis.* Pharm Res, 2010. **27**(2): p. 264-71.
268. Saif, J., et al., *Combination of injectable multiple growth factor-releasing scaffolds and cell therapy as an advanced modality to enhance tissue neovascularization.* Arterioscler Thromb Vasc Biol, 2010. **30**(10): p. 1897-904.
269. Sy, J.C., et al., *Sustained release of a p38 inhibitor from non-inflammatory microspheres inhibits cardiac dysfunction.* Nat Mater, 2008. **7**(11): p. 863-8.
270. Samuel, S.M., et al., *Coadministration of adenoviral vascular endothelial growth factor and angiopoietin-1 enhances vascularization and reduces ventricular remodeling in the infarcted myocardium of type 1 diabetic rats.* Diabetes, 2010. **59**(1): p. 51-60.
271. Zentilin, L., et al., *Cardiomyocyte VEGFR-1 activation by VEGF-B induces compensatory hypertrophy and preserves cardiac function after myocardial infarction.* FASEB J, 2010. **24**(5): p. 1467-78.
272. Wang, Y., et al., *Hepatocyte growth factor prevents ventricular remodeling and dysfunction in mice via Akt pathway and angiogenesis.* J Mol Cell Cardiol, 2004. **37**(5): p. 1041-52.
273. Vilahur, G., et al., *Molecular and cellular mechanisms involved in cardiac remodeling after acute myocardial infarction.* J Mol Cell Cardiol, 2011. **50**(3): p. 522-33.
274. Tang, J., et al., *Vascular endothelial growth factor promotes cardiac stem cell migration via the PI3K/Akt pathway.* Exp Cell Res, 2009. **315**(20): p. 3521-31.
275. Linke, A., et al., *Stem cells in the dog heart are self-renewing, clonogenic, and multipotent and regenerate infarcted myocardium, improving cardiac function.* Proc Natl Acad Sci U S A, 2005. **102**(25): p. 8966-71.
276. Chimenti, I., et al., *Human cardiosphere-seeded gelatin and collagen scaffolds as cardiogenic engineered bioconstructs.* Biomaterials, 2011. **32**(35): p. 9271-81.
277. Xaymardan, M., et al., *c-Kit function is necessary for in vitro myogenic differentiation of bone marrow hematopoietic cells.* Stem Cells, 2009. **27**(8): p. 1911-20.
278. Kadner, K., et al., *The beneficial effects of deferred delivery on the efficiency of hydrogel therapy post myocardial infarction.* Biomaterials, 2012. **33**(7): p. 2060-6.
279. Rane, A.A., et al., *Increased infarct wall thickness by a bio-inert material is insufficient to prevent negative left ventricular remodeling after myocardial infarction.* PLoS One, 2011. **6**(6): p. e21571.
280. Choquet, D., D.P. Felsenfeld, and M.P. Sheetz, *Extracellular matrix rigidity causes strengthening of integrin-cytoskeleton linkages.* Cell, 1997. **88**(1): p. 39-48.
281. Galbraith, C.G., K.M. Yamada, and M.P. Sheetz, *The relationship between force and focal complex development.* Journal of Cell Biology, 2002. **159**(4): p. 695-705.